Synthesis and Thermoelectric Properties of Cu-Sb-S Compounds

Kan Chen

Submitted in partial fulfilment of the requirements of the Degree of Doctor of Philosophy

School of Engineering and Materials Science,
Queen Mary, University of London
London, United Kingdom
August 2016

Declaration

I hereby declare that the present work is prepared solely by me during the course of my doctoral studies at the Queen Mary, University of London. It has not been submitted anywhere for any award. Work of other people is fully acknowledged according to standard referencing.

This thesis fully complies with the regulations set by the University of London and the Queen Mary, University of London.

Kan Chen

August 2016

Abstract

The Cu-Sb-S compounds ($Cu_{12}Sb_4S_{13}$, $CuSbS_2$, Cu_3SbS_3 and Cu_3SbS_4) have the advantages of earth-abundance, low-toxicity and low-cost, compared with conventional thermoelectric materials. This work provides a comprehensive study on the synthesis methods, crystal structures and thermoelectric properties of Cu-Sb-S compounds. All of the samples were prepared by mechanical alloying combined with SPS, which had high density, high purity and very fine microstructure. The lone-pair electrons of Sb and the [CuS3] plane play important roles in realizing very low lattice thermal conductivity of these compounds. Except for $Cu_{12}Sb_4S_{13}$, which is known as a good thermoelectric material, the other three compounds showed very poor thermoelectric performance due to their high electrical resistivities. A phase transition at 398 K was found in Cu_3SbS_3, which makes it unsuitable for applications and attempts to optimize electrical properties of $CuSbS_2$ failed. Different p-type dopants were studied to improve the electrical properties of Cu_3SbS_4. Both Ge-doping and Sn-doping on Sb sites increased the carrier concentration of Cu_3SbS_4 significantly. The electrical transport properties were analyzed using SPB model, and a large effective mass of 3.0 m_e was found for all of the samples. A maximum zT value of 0.69 was obtained at 623 K in 5 mol. % Sn-doped sample which was about 6 times higher than that of undoped sample. The solid-solutions of $Cu_3SbS_{4(1-y)}Se_{4y}$ were studied to further improve the thermoelectric properties. The lattice thermal conductivity was reduced in solid-solution due to the local mass contrast and alloying scattering, but there was no further improvement in zT value due to the decrease in Seebeck coefficient. Another solid solution of $Cu_3Sb_{1-x}Bi_xS_4$ was studied, but Bi had very low solubility and a second phase was formed instead of forming the solid solution. Future work should

focus on reducing the lattice thermal conductivity of Cu_3SbS_4 without impacting its electrical properties.

Acknowledgement

I would like to express my sincere gratitude to my supervisor, Prof. Michael John Reece for his support, patience, motivation and guidance throughout my PhD study at Queen Mary, University of London. I would also like to thank my secondary supervisor Dr. Haixue Yan for his help in my study.

I would specially like to thank Dr. Baoli Du, Dr. Huanpo Ning and Dr. Ruizhi Zhang for stimulating discussions, ideas and helping with the experiments and papers. I would like to thank Dr. Isaac Abrahams and Dr. Rory Wilson for their help with XRD structural analysis, Deepanshu Srivastava and Prof. Robert Freer for their help with Seebeck and resistivity measurements. Claire Burgess, Becky Kilmurray and Dr Martyn McLachlan at Imperial College, London for their help in Hall measurements, Dr Haitao Ye at Aston University, Birmingham for his help in XPS measurements and Dr Cedric Weber and Dr Bonini Nicola at King's College, London for helping with theoretical study and calculations.

I would like to thank everyone in the Ceramic group for their help and friendship.

I would like to thank Chinese Scholarship Council for the support and funding for my PhD.

Finally, I would like to thank my family and friends for all their support and in particular my mother and father for their endless love, support and encouragement.

Table of Contents

Abstract i

Acknowledgement iii

Table of Contents iv

List of Figures viii

List of Tables xviii

Chapter 1 Introduction 1

Chapter 2 Review of Thermoelectrics 4

2.1 Thermoelectric Effects and Applications 4

2.2 The Conversion Efficiency and the Figure of Merit 7

2.3 Strategies to Improve the Figure of Merit 9

2.4 Traditional Thermoelectric Materials 13

2.4.1 Introduction 13

2.4.2 Bismuth Telluride 13

2.4.3 Lead Telluride 15

2.4.4 Silicon Germanium Alloy 17

2.4.5 Conclusions 17

2.5 Thermoelectric Sulfides 18

2.5.1 Introduction 18

2.5.2 Copper Sulfide 18

2.5.3 Lead Sulfide 20

2.5.4 Bismuth Sulfide (Bi_2S_3) 22

2.5.5 Tin Sulfide (SnS) 23

2.5.6 Titanium Sulfide 24

2.5.7 Tetrahedrite 26

2.5.8 Conclusions 35

2.6 Cu-Sb-S Ternary Compounds 36

2.6.1 Introduction 36

2.6.2 $CuSbS_2$ (Chalcostibite) 37

2.6.3 Cu_3SbS_3 (Skinnerite) 41

2.6.4 Cu_3SbS_4 (Famatinite) 45

2.6.5 Conclusions 52

Chapter 3 Experimental Details 53

3.1 Sample Preparations 53

3.1.1 Mechanical Alloying 53

3.1.2 Melt Processing 54

3.1.3 Spark Plasma Sintering (SPS) 55

3.2 Characterizations 56

3.2.1 Density Measurements 56

3.2.2 X-Ray Diffraction and X-Ray Photoelectron Spectroscopy 56

3.2.3 Scanning Electron Microscopy 57

3.2.4 Electrical Characterizations 58

3.2.5 Thermal Characterizations 60

Chapter 4 Initial Investigation of Cu-Sb-S Compounds 62

4.1 Introduction 62

4.2 Experimental Details 63

4.3 Results and Discussions 63

4.3.1 Comparative Study of Synthesis Methods 63

4.3.2 Comparative Study of Undoped Cu-Sb-S Compounds 69

4.3.3 Attempts to Optimize Electrical Properties of $CuSbS_2$ 80

4.4 Conclusions 82

Chapter 5 Thermoelectric Properties of Ge-doped Cu_3SbS_4 84

5.1 Introduction 84

5.2 Experimental Details 85

5.3 Results and Discussions 85

5.4 Conclusions 100

Chapter 6 Thermoelectric Properties of Sn-doped Cu_3SbS_4 102

6.1 Introduction 102

6.2 Experimental Details 103

6.3 Results and Discussions 103

6.4 Conclusions 125

Chapter 7 Thermoelectric Properties of $Cu_3SbS_{4(1-y)}Se_{4y}$ Solid Solution 127

7.1 Introduction 127

7.2 Experimental Details 128

7.3 Results and Discussions 128

7.4 Conclusions 137

Chapter 8 Conclusions and Future Work 138

8.1 Conclusions 138

8.2 Future Work 141

8.2.1 $CuSbS_2$ 141

8.2.2 Cu_3SbS_4 142

8.2.3 Other Sulfides 142

List of Publications 143

References 144

Appendix 162

List of Figures

Figure 2.1: The schematics of (a) Seebeck effect and (b) thermoelectric power generator.

Figure 2.2: The schematics of (a) Peltier effect and (b) thermoelectric cooler.

Figure 2.3: The schematic of thermoelectric device.

Figure 2.4: The thermodynamic efficiency of thermoelectric materials as a function of *zT* assuming a cold side temperature of 298 K [19].

Figure 2.5: The schematic dependence of α, σ, $\alpha^2\sigma$, and k on carrier concentration [21].

Figure 2.6: The schematic of different wavelength phonons scattering (adapted from reference [29]).

Figure 2.7: Thermoelectric performance of typical material for different temperature ranges (adapted from reference [5, 30, 31, 32, 34, 35]).

Figure 2.8: The crystal structure of Bi_2Te_3 [20].

Figure 2.9: (a) The TEM of nano-inclusion in LAST [32]; (b) schematic of a Tl-related level increasing the density of states in pure PbTe [33]; (c) schematic of valence bands convergence in $PbTe_{0.85}Se_{0.15}$ [27]; (d) all-length-scale hierarchy in PbTe [5].

Figure 2.10: The Cu-S phase diagram [37].

Figure 2.11: (a) Crystal structure of cubic phase of $Cu_{2-x}S$. The blue spheres represent sulfur atoms and the liquid-like copper ions (orange) travel freely within the sulfide

sublattice; (b) temperature dependence of thermal conductivity in $Cu_{2-x}S$ [12].

Figure 2.12: (a) Binary phase diagram of PbS-Bi_2S_3(Sb_2S_3); (b) high-resolution TEM images of PbS with 1.0 mol. % Sb_2S_3 and doped with 1.0 mol. % $PbCl_2$ [41].

Figure 2.13: (a) Temperature dependence of lattice thermal conductivity for Bi_2S_3 with $CuBr_2$ doping; (b) high magnification TEM image showing the Cu-nanoparticles [45].

Figure 2.14: (a) Crystal structure of SnS; (b) the fractured surface of SnS [47].

Figure 2.15: (a) Crystal structure of TiS_2 [50]; (b) TEM images and simulated crystal structure of $(BiS)_{1.2}(TiS_2)_2$ [49].

Figure 2.16: Crystal structure of $Cu_{12}Sb_4S_{13}$ (left). The three-coordinate Cu atoms and the three-coordinate Sb atoms with lone-pair electrons (right) [54].

Figure 2.17: Side view of the trigonal bipyramid in $Cu_{12}Sb_4S_{13}$ with Cu in the off-centered position [55].

Figure 2.18: Electronic band structure and density of states (DOS) of $Cu_{12}Sb_4S_{13}$ [15].

Figure 2.19: (a) XRD patterns of $Cu_{10}Tr_2Sb_4S_{13}$ samples; (b) The temperature dependence of resistivity, Seebeck coefficient and thermal conductivity of $Cu_{10}Tr_2Sb_4S_{13}$ samples [56].

Figure 2.20: Maximum *zT* values reported for tetrahedrite materials [64].

Figure 2.21: The temperature dependence of (a) electrical conductivity, (b) Seebeck coefficient, (c) thermal conductivity and (d) *zT* value of $Cu_{10}TM_2Sb_4S_{13}$ samples [17].

Figure 2.22: (a) The *zT* value, (b) thermal conductivity and power factor, (c) electrical conductivity and Seebeck coefficient as a function of Mn concentration in Cu_{12-}

$_xMn_xSb_4S_{13}$ samples at 575 K [17].

Figure 2.23: The temperature dependence of (a) resistivity, (b) Seebeck coefficient, (c) thermal conductivity, and (d) *zT* value of natural mineral based tetrahedrites [57].

Figure 2.24: The state-of-the-art thermoelectric sulfides (adapted from reference [12, 17, 41, 45, 47, 52]).

Figure 2.25: Phase relations in the Cu-Sb-S system at 500 ℃. Compositions are plotted in atom percent. One-phase field appears as points or are stippled, two-phase fields are shaded by tie lines and three-phase fields are open [66].

Figure 2.26: (a) Structure of $CuSbS_2$ showing CuS4 tetrahedron (blue), SbS5 square pyramid (grey) and S atoms (yellow); (b) SbS5 square pyramid with lone-pair electrons (red) [67].

Figure 2.27: Orbital-projected density of states for $CuSbS_2$ [67].

Figure 2.28: (a)The temperature dependence of resistivity [75]; (b)The temperature dependence of theoretical Seebeck coefficient at different hole concentrations for $CuSbS_2$ [76].

Figure 2.29: The temperature dependence of (a) lattice parameters and (b) thermal conductivity and heat capacity for Cu_3SbSe_3 [86].

Figure 2.30: The temperature dependence of (a) heat capacity, (b) thermal conductivity, (c) resistivity, (d) Seebeck coefficient, (e) power factor and (f) *zT* value for Cu_3SbSe_3[84].

Figure 2.31: The crystal structures of Cu_3SbS_3 at different temperature: (a) below 263

K, (b) between 263 K and 395 K, and (c) above 395 K [77].

Figure 2.32: (a) The crystal structure and (b) band structure of Cu_3SbS_4 [93].

Figure 2.33: The temperature dependence of (a) electrical conductivity, (b) Seebeck coefficient, (c) thermal conductivity, and (d) zT value for $Cu_3Sb_{1-x}Sn_xSe_4$ [94].

Figure 2.34: The temperature dependence of zT values for Cu_3SbSe_4 from different reports (adapted from reference [94-101]).

Figure 2.35: The backscattered electron image of Cu_3SbS_4 bulk sample [103].

Figure 2.36: The temperature dependence of (a) electrical conductivity, (b) Seebeck coefficient, (c) power factor, and (d) carrier concentration for $Cu_3Sb_{1-x}Ge_xS_4$ [103].

Figure 3.1: (a) QM-3SP4 planetary ball-milling machine; (b) Saffron scientific glove box.

Figure 3.2: (a) Quartz ampoule sealed in vacuum; (b) Box furnace (Carbolite HTF 1800).

Figure 3.3: (a) Spark plasma sintering furnace (FCT, Germany); (b) working schematic [104].

Figure 3.4: Schematic of electrical resistivity and Seebeck coefficient measurements.

Figure 3.5: Principles of Hall measurements.

Figure 3.6: Schematic of thermal diffusivity measurements.

Figure 4.1: XRD patterns of Cu_3SbS_4 samples prepared by (a) melt processing and (b) mechanical alloying method.

Figure 4.2: SEM images of Cu_3SbS_4 samples prepared by (a) melting + SPS and (b)

MA+SPS.

Figure 4.3: SEM images of Cu_3SbS_4 powder after ball milling.

Figure 4.4: XRD peak for particle and grain size calculations.

Figure 4.5: Back scattered image and EDX mapping of Cu_3SbS_4 sample prepared by MA+SPS.

Figure 4.6: The temperature dependence of thermal conductivities for Cu_3SbS_4 samples prepared by melting + SPS and MA + SPS. Note there is a 10 % uncertainty in all data points.

Figure 4.7: XRD patterns of (a) $Cu_{12}Sb_4S_{13}$, (b) Cu_3SbS_3, (c) $CuSbS_2$, and (d) Cu_3SbS_4 samples before and after SPS.

Figure 4.8: The fracture surface SEM images of (a) $Cu_{12}Sb_4S_{13}$, (b) Cu_3SbS_3, (c) $CuSbS_2$, and (d) Cu_3SbS_4 bulk samples.

Figure 4.9: The temperature dependence of (a) electrical resistivities, (b) Seebeck coefficients and (c) power factors for $Cu_{12}Sb_4S_{13}$, Cu_3SbS_3, $CuSbS_2$, and Cu_3SbS_4 samples. Note there is a 5 % uncertainty in all data points.

Figure 4.10: The temperature dependence of (a) thermal conductivities and (b) lattice thermal conductivities for $Cu_{12}Sb_4S_{13}$, Cu_3SbS_3, $CuSbS_2$, and Cu_3SbS_4 samples. Note there is a 10% uncertainty in all data points.

Figure 4.11: The temperature dependence of lattice thermal conductivity for $Cu_{12}Sb_4S_{13}$, Cu_3SbS_3, $CuSbS_2$ and Cu_3SbS_4 samples, individually. Note there is a 10% uncertainty in all data points.

Figure 4.12: The average bond angles of S-Sb-S for Cu_3SbS_4 [90], $Cu_{12}Sb_4S_{13}$ [112], $CuSbS_2$ [113], and Cu_3SbS_3 [114], individually.

Figure 4.13: The temperature dependence of *zT* value for $Cu_{12}Sb_4S_{13}$, $CuSbS_2$, Cu_3SbS_4 and Cu_3SbS_3 samples. Note there is a 20 % uncertainty in all data points.

Figure 4.14: The XRD results of $CuSbS_2$ with (a) Sn-doping, (b) In- doping and (c) Co-doping.

Figure 4.15: The XRD results of $Cu_{1-x}SbS_2$ (x = 0 ~ 0.05) samples.

Figure 5.1: XRD patterns of $Cu_3Sb_{1-x}Ge_xS_4$ (x = 0 ~ 0.15) samples and the enlarged figure shows the peak shift.

Figure 5.2: SEM images of fracture surface for $Cu_3Sb_{1-x}Ge_xS_4$ (x = 0.0125) sample.

Figure 5.3: SEM images of fracture surface for $Cu_3Sb_{1-x}Ge_xS_4$ (x = 0.025, 0.05, 0.1 and 0.15) samples.

Figure 5.4: EDX analysis for Ge-doped Cu_3SbS_4 with the second phase.

Figure 5.5: The theoretical and experimental carrier concentration as a function of nominal Ge content in $Cu_3Sb_{1-x}Ge_xS_4$ system.

Figure 5.6 The temperature dependence of (a) electrical resistivity, (b) Seebeck coefficient and (c) power factor for $Cu_3Sb_{1-x}Ge_xS_4$ (x = 0 ~ 0.15) samples. Note there is a 5 % uncertainty in all data points.

Figure 5.7 The carrier concentration (n) dependence of Seebeck coefficient (α) at 300 K and the Pisarenko line with $m^* = 3.0\ m_e$.

Figure 5.8 The calculated band structure of Cu_3SbS_4 (left) and corresponding density-

of-state (DOS) (right). (The results are courtesy of C. Weber and N. Bonini, King's College, London.)

Figure 5.9 The density-of-state of undoped Cu_3SbS_4 and Ge-doped Cu_3SbS_4. The DOS of undoped Cu_3SbS_4 has been shifted to account for the extra hole introduced by Ge-doping. (The results are courtesy of C. Weber and N. Bonini, King's College, London.)

Figure 5.10 The theoretical and experimental power factor (PF) as a function of carrier concentration (n) at 600 K. (The results are courtesy of C. Weber and N. Bonini, King's College, London.)

Figure 5.11 The temperature dependence of total thermal conductivity for $Cu_3Sb_{1-x}Ge_xS_4$ (x = 0 ~ 0.15) samples. Note there is a 10% uncertainty in all data points.

Figure 5.12 (a) The calculated Lorenz number and (b) the temperature dependence of lattice thermal conductivity for $Cu_3Sb_{1-x}Ge_xS_4$ (x = 0 ~ 0.15) samples. Note there is a 10 % uncertainty in all data points.

Figure 5.13 The temperature dependence of the *zT* value for $Cu_3Sb_{1-x}Ge_xS_4$ (x = 0 ~ 0.15) samples. Note there is a 20 % uncertainty in all data points.

Figure 6.1: (a) XRD patterns of $Cu_3Sb_{1-x}Sn_xS_4$ (x = 0 ~ 0.5) samples and (b) the enlarged figure shows the peak shift.

Figure 6.2: SEM images of fracture surface for $Cu_3Sb_{1-x}Sn_xS_4$ (x = 0, 0.1, 0.3 and 0.5) samples.

Figure 6.3: X-ray photoelectron spectra (XPS) survey spectrum of $Cu_3Sb_{1-x}Sn_xS_4$ (x = 0, 0.1, 0.3 and 0.5) samples.

Figure 6.4: X-ray photoelectron spectra (XPS) spectrum of Cu2p core level, Sb3d core level and S2p core level for Cu_3SbS_4 sample.

Figure 6.5: X-ray photoelectron spectra (XPS) spectrum of Sb3d core level for Cu_3SbS_4 and $CuSbS_2$ samples.

Figure 6.6: X-ray photoelectron spectra (XPS) spectrum of (a) Cu2p, (b) Sb3d, (c) Sn3d and (d) S2p for $Cu_3Sb_{1-x}Sn_xS_4$ (x = 0, 0.1, 0.3 and 0.5) samples.

Figure 6.7 The temperature dependence of (a) electrical resistivity, (b) Seebeck coefficient and (c) power factor for $Cu_3Sb_{1-x}Sn_xS_4$ (x = 0 ~ 0.5) samples. Note there is a 5 % uncertainty in all data points.

Figure 6.8 The temperature dependence of (a) thermal conductivity, (b) lattice thermal conductivity and (c) calculated Lorenz number for $Cu_3Sb_{1-x}Ge_xS_4$ (x = 0 ~ 0.5) samples. Note there is a 10 % uncertainty in all data points.

Figure 6.9 The temperature dependence of the *zT* value for $Cu_3Sb_{1-x}Sn_xS_4$ (x = 0 ~ 0.5). Note there is a 20 % uncertainty in all data points.

Figure 6.10: XRD patterns of $Cu_3Sb_{1-x}Sn_xS_4$ (x = 0 ~ 0.15) samples.

Figure 6.11: SEM images for $Cu_3Sb_{1-x}Sn_xS_4$ (x = 0, 0.01, 0.05 and 0.15) samples.

Figure 6.12: EDX mapping for $Cu_3Sb_{1-x}Sn_xS_4$ (x = 0.15) sample.

Figure 6.13: The theoretical and experimental carrier concentration as a function of nominal Sn content.

Figure 6.14 The temperature dependence of (a) electrical resistivity, (b) Seebeck coefficient and (c) power factor for $Cu_3Sb_{1-x}Sn_xS_4$ (x = 0 ~ 0.15) samples. Note there is

a 5 % uncertainty in all data points.

Figure 6.15 The carrier concentration (n) dependence of Seebeck coefficient (α) at 300 K and the Pisarenko line with m* = 3.0 m_e.

Figure 6.16 The temperature dependence of (a) thermal conductivity, (b) lattice thermal conductivity and (c) calculated Lorenz number for $Cu_3Sb_{1-x}Sn_xS_4$ (x = 0 ~ 0.15) samples. Note there is a 10 % uncertainty in all data points.

Figure 6.17 The temperature dependence of the *zT* value for $Cu_3Sb_{1-x}Sn_xS_4$ (x = 0 ~ 0.15) samples. Note there is a 20 % uncertainty in all data points.

Figure 6.18 The power factor, *zT* value and thermal conductivity as a function of carrier concentration for $Cu_3Sb_{1-x}Sn_xS_4$ (x = 0 ~ 0.15) samples.

Figure 7.1: XRD patterns of $Cu_3SbS_{4(1-y)}Se_{4y}$ (y = 0 ~ 0.5) samples and the enlarged figure showing peak shift.

Figure 7.2: Calculated lattice parameters of $Cu_3SbS_{4(1-y)}Se_{4y}$ (y = 0 ~ 0.5) samples and the red dash line represents the Vegard's law.

Figure 7.3: SEM images of $Cu_3SbS_{4(1-y)}Se_{4y}$ (y = 0, 0.05, 0.1 and 0.2) samples.

Figure 7.4: (a) ~ (e) SEM images of $Cu_3SbS_{4(1-y)}Se_{4y}$ (y = 0.2) samples and (f) SEM image of Cu_3SbSe_4 from reference [99]

Figure 7.5: The temperature dependence of thermal conductivity for $Cu_3SbS_{4(1-y)}Se_{4y}$ (y = 0 ~ 0.5) samples. Note there is a 10 % uncertainty in all data points.

Figure 7.6: The temperature dependence of (a) electrical resistivity, (b) Seebeck coefficient, (c) power factor and (d) *zT* value for sample A, B, C and D. Note there is a

20 % uncertainty in *zT* values and a 5 % uncertainty in all other data points.

Figure 7.7: XRD patterns of $Cu_3Sb_{1-x}Bi_xS_4$ (x = 0 ~ 0.3) samples.

List of Tables

Table 4.1: The theoretical, measured and relative densities of $Cu_{12}Sb_4S_{13}$, Cu_3SbS_3, $CuSbS_2$ and Cu_3SbS_4 bulk samples.

Table 5.1 Room temperature Hall coefficient, carrier concentration, carrier mobility, Seebeck coefficient and electrical resistivity of $Cu_3Sb_{1-x}Ge_xS_4$ (x = 0 ~ 0.15) samples.

Table 6.1 Room temperature Hall coefficient, carrier concentration, carrier mobility, Seebeck coefficient and electrical resistivity of $Cu_3Sb_{1-x}Sn_xS_4$ (x = 0 ~ 0.2) samples.

Chapter 1 Introduction

Thermoelectric (TE) technology is attracting growing attention due to the global need for clean, safe and sustainable energy sources. As known, 78.3 % of the global energy consumption is from fossil fuels (petroleum, natural gas and coal), which are unsustainable and cause serious environmental issues [1]. Moreover, more than 50 % of the fossil fuels used in automobiles and coal-fired power plants is wasted in the form of heat. Solid-state devices based on thermoelectric materials can directly convert waste heat into useful electricity. In the other words, it can improve the efficiency of energy usage while reducing greenhouse-gas emissions. The working principle of a thermoelectric device is similar to the thermodynamic principles that govern the operation of conventional heat engines, except for the fact that the working fluid of thermoelectric power generators are electrons instead of steam or air [2]. The conversion efficiency is largely determined by figure of merit (zT) of the thermoelectric materials, which is defined as $zT = \alpha^2\sigma T/\kappa$, where α is Seebeck coefficient, σ is electrical conductivity, κ is thermal conductivity and T is absolute temperature. Ideally, a good thermoelectric material simultaneously possesses high electrical conductivity, large Seebeck coefficient and low thermal conductivity.

With the development of nano-structuring, new materials and fabrication technologies, there have been continuous reports of materials with high zT values, such as $Bi_xSb_{2-x}Te_3$

(zT~1.56 at 300 K) [3], filled Skutterudites (zT~1.45 at 850 K) [4], Na doped PbTe-SrTe (zT~2.2 at 915 K) [5], $AgSbTe_2$ (zT~1.59 at 673 K) [6], $AgPb_{18+x}SbTe_{20}$(LAST) (zT~1.7 at 700 K) [7], SiGe alloys (zT~1.3 at 1173 K) [8], $(AgSbTe_2)_{1-x}(GeTe)_x$(TAGS) (zT~1.5 at 700 K) [9] and SnSe single crystal (zT~2.6 at 923 K) [10]. However, some of the key component elements in these high-zT materials are very rare in the Earth's crust, such as Te (0.001 ppm by weight) and Se(0.05 ppm by weight) [11]. If thermoelectric devices are to reach mass markets in the future, cost and environmental conservation issues should be taken into consideration when choosing elements used for thermoelectric materials.

Sulfide compounds could be a potential alternative for telluride and selenide compounds, as sulfur is low cost, environment-friendly, non-toxic, and earth-abundant (at least 10 000 times more abundant than selenium in the earth's crust). However, the zT values of sulfides are so far less than their counterpart selenides and tellurides, due to their relatively high thermal conductivities. Generally, the compounds containing light elements (sulfur) have stronger and more covalent bonds than their analogues containing heavier elements (selenium and tellurium). Such strong bonds give stiffer elastic constants and higher speeds of sound, which lead to higher thermal conductivity in sulfides [12]. Also sulfide tends to have a larger band-gap and a lower carrier mobility than its counterpart of selenide and telluride, and it leads to a lower electrical conductivity in sulfide [13, 14]. In recent years, the copper antimony sulfosalt mineral tetrahedrite, was found to have intrinsically low thermal conductivity. The base composition of

tetrahedrite is $Cu_{12}Sb_4S_{13}$, and its low thermal conductivity most likely derives from its complex crystal structure and the lone-pair electrons of Sb [15]. The Sb atoms occupy a tetrahedral site but are bonded to only three sulfur atoms, leaving a void and lone-pair electrons in the structure. Skoug and Morelli [16] identified a correlation between minimal thermal conductivity and lone-pair electrons of Sb in nitrogen-group chalcogenide compounds. Electrostatic repulsion between the lone-pair electrons and neighboring atoms creates anharmonicity in the lattice, which leads to a low thermal conductivity. By optimizing the electrical properties of $Cu_{12}Sb_4S_{13}$, zT value above 1 has been achieved [17].

Due to the unique features of Sb and the high thermoelectric performance achieved in $Cu_{12}Sb_4S_{13}$, it is worth exploring other Cu-Sb-S compounds as potentially good thermoelectric materials. Four major phases are found to exist in the Cu−Sb−S system, namely, $Cu_{12}Sb_4S_{13}$ (Tetrahedrite), $CuSbS_2$ (Chalcostibite), Cu_3SbS_3 (Skinnerite), and Cu_3SbS_4 (Famatinite). Up to now, there has been no systemic research of the thermoelectric properties of Cu-Sb-S compounds. Thus, the synthesis methods, crystal structures, microstructures and thermoelectric properties of Cu-Sb-S all four compounds were investigated systematically, aiming to find out the effects of lone-pair electrons and the potential use of these compounds as thermoelectric materials.

Chapter 2 Review of Thermoelectrics

2.1 Thermoelectric Effects and Applications

The thermoelectric effects provide a way for the direct and reversible conversion between thermal energy and electricity, which can be used for power generation and electronic refrigeration. There are three related effects, including the Seebeck effect, Peltier effect, and Thomson effect.

The Seebeck effect was discovered by Thomas J. Seebeck in 1823, when he observed that a compass needle was deflected by a closed circuit composed of two different metals, with a temperature difference between two junctions. Figure 2.1 (a) shows a schematic circuit of two different conductors, A and B, with junctions at different temperature T and $T + \Delta T$. An electromotive force E_{AB} will be generated between A and B, which is given by

$$E_{AB} = \alpha_{AB} \times \Delta T \tag{2.1}$$

Here α_{AB} is the defined as the relative Seebeck coefficient between A and B, where $\alpha_{AB} = \alpha_A - \alpha_B$ and α_A and α_B are the respective absolute Seebeck coefficients of the conductors [18]. The model of thermoelectric power generator based on Seebeck effect is shown in Figure 2.1 (b). The thermoelectric power generators can be applied in waste heat recovery in many applications, such as automobiles, coal-fired power plants, wood stoves, outdoor boilers and so on. Unlike traditional heat engines, the solid-state devices

have no moving parts, require no maintenance, and have long life and high reliability. Also they are primarily used as power generators in remote and unmanned places, such as deep-space and deep-ocean. For instance, the Voyager space probes launched by NASA have been working for more than 34 years and have now left the solar system.

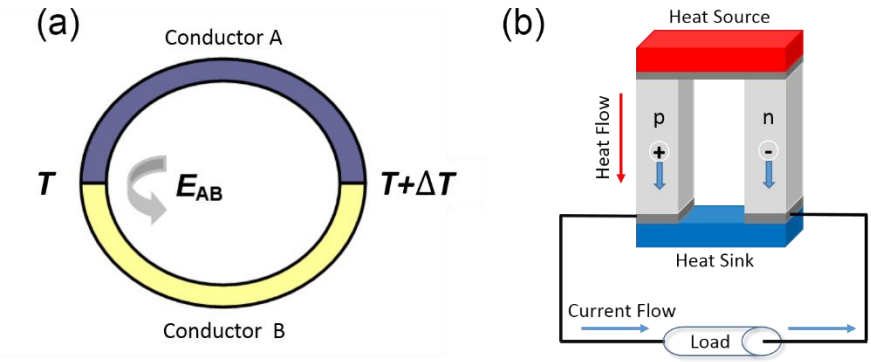

Figure 2.1: *The schematics of (a) Seebeck effect and (b) thermoelectric power generator.*

The Peltier effect is the reverse of the Seebeck effect, which was discovered by Jean Charles Athanase Peltier in 1834. The Peltier effect is described in Figure 2.2 (a). When an electric current *I* passes through a circuit composed of two different conductors A and B, heat is absorbed at one junction and liberated at the other one. The rate of heat exchange *Q* at the junctions is given by

$$Q = \pi_{AB} \times I \qquad (2.2)$$

Here π_{AB} is defined as the relative Peltier coefficient, where $\pi_{AB} = \pi_A - \pi_B$ and π_A and π_B are the respective absolute Peltier coefficients of the conductors [18]. Figure 2.2 (b) illustrates the operation of a thermoelectric cooler based on the Peltier effect. Compared

to a vapor-compression refrigerator, a thermoelectric cooler has the primary advantages of no moving parts, no liquid refrigerant, long life, compact size and flexible shape.

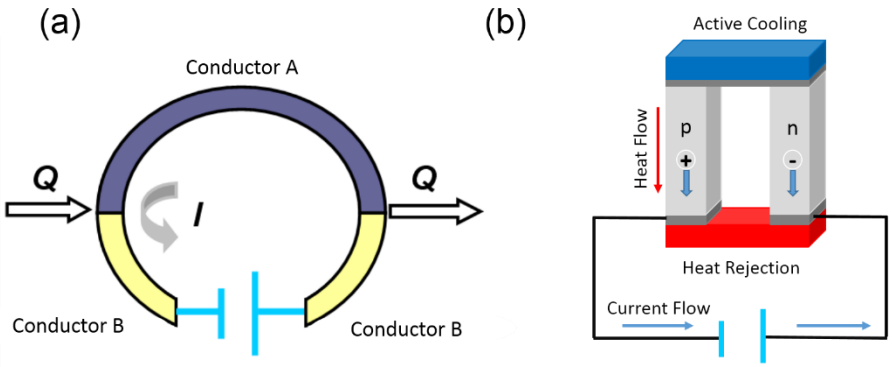

Figure 2.2: *The schematics of (a) Peltier effect and (b) thermoelectric cooler.*

In 1851, William Thomson (Lord Kelvin) predicted the Thomson effect by thermodynamic analysis and proved it subsequently experimentally. It describes the reversible heat exchange in a single homogeneous conductor when a temperature gradient and an electric current are applied at the same time. Later, Thomson established the thermodynamic relationships between the three effects, which are given by

$$\tau = T\frac{\mathrm{d}\alpha}{\mathrm{d}T} \tag{2.3}$$

and

$$\pi = \alpha T \tag{2.4}$$

where T is the absolute temperature, τ is the Thomson coefficient, α is the Seebeck coefficient, and π is the Peltier coefficient. The Thomson relations indicated that Thomson, Peltier, and Seebeck effects are different manifestations of one effect.

2.2 The Conversion Efficiency and the Figure of Merit

Thermoelectric devices consist of a series of thermoelectric unicouples (n and p legs) which are electrically connected, as illustrated in Figure 2.3. The number of unicouples in a device depends on the power output requirement. As the materials investigated in this work are related to thermoelectric power generators, the illustration of device and its efficiency is based on power generation.

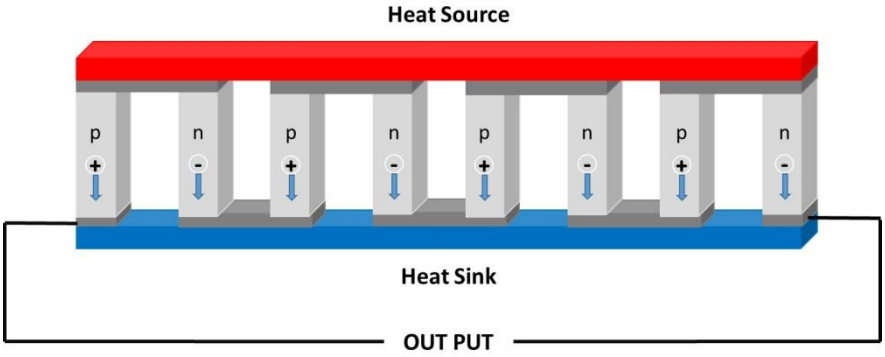

Figure 2.3: *The schematic of thermoelectric device.*

Deriving from Altenkirch's research in 1911, the maximum efficiency of a thermoelectric power generation device is written as

$$\eta = \frac{T_{hot} - T_{cold}}{T_{hot}} \frac{\sqrt{1+zT_{avg}} - 1}{\sqrt{1+zT_{avg}} + T_{cold}/T_{hot}} \qquad (2.5)$$

where T_{hot} is the temperatures of the hot side(heat source), T_{cold} is the temperature of cold side (heat sink) and zT_{avg} is the average figure of merit. The equation indicates that, with a certain temperature difference, the conversion efficiency is largely determined by the

materials' figure of merit. Figure 2.4 shows the relationship between *zT* value and conversion efficiency. Up to now, the thermoelectric devices based on commercial materials Bi_2Te_3 have an efficiency of 5 ~ 8 %, which is far behind conventional engines and photovoltaic power systems. Thus, one of the key points for thermoelectric applications is to improve the *zT* value.

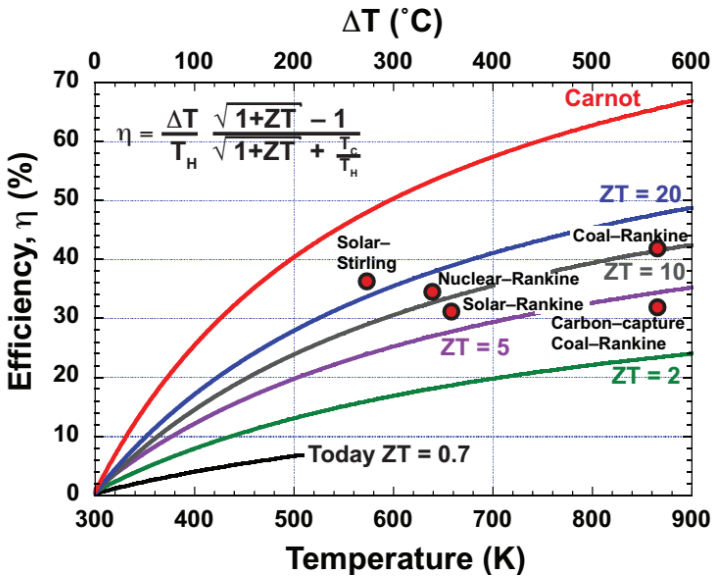

Figure 2.4: *The thermodynamic efficiency of thermoelectric materials as a function of zT assuming a cold side temperature of 298 K [19].*

The dimensionless figure of merit *zT* is the guidance to search good thermoelectric materials, which is defined as

$$zT=(\alpha^2\sigma T)/\kappa \qquad (2.6)$$

where α is Seebeck coefficient, σ is electrical conductivity, κ is thermal conductivity and T is absolute temperature. The quantity $\alpha^2\sigma$ is known as the power factor (*PF*). The

thermal conductivity κ has a contribution from electrons and lattice vibrations (phonons), which can be written as,

$$\kappa = \kappa_e + \kappa_L \tag{2.7}$$

Here, κ_e is the electronic thermal conductivity and κ_L is the lattice thermal conductivity. A low thermal conductivity is necessary to maintain a large temperature difference in devices. Thus, a good thermoelectric material should possess high Seebeck coefficient, large electrical conductivity and low thermal conductivity, simultaneously [20].

2.3 Strategies to Improve the Figure of Merit

Since a renewed interest in thermoelectric technology in the 1990s, a lot of effort has been made to improve the figure of merit, *zT*. Although there is no theoretical limit on *zT*, it is very difficult to make significant improvements. In order to show the relations among the electrical conductivity (σ), Seebeck coefficient (α) and thermal conductivity (κ), these parameters can be written as functions of carrier concentration (n),

$$\sigma = ne\mu \tag{2.8}$$

$$\alpha = \frac{8\pi^2 \kappa_B^{\,2}}{3eh^2} m^* T \left(\frac{\pi}{3n}\right)^{\frac{2}{3}} \tag{2.9}$$

$$\kappa_e = L\sigma T = Lne\mu T \tag{2.10}$$

Based on these equations, the schematic dependence of different parameters on carrier concentration can be seen in Figure 2.5 [21]. For a certain material, a higher carrier concentration gives higher electrical conductivity while leads to lower Seebeck coefficient. There is always a trade-off between the electrical conductivity and the

Seebeck coefficient. Thus, the power factor can be maximized at certain carrier concentration. For a good thermoelectric material, the typical values of carrier concentration, electrical conductivity and Seebeck coefficient are around 10^{20} cm^{-3}, 10^5 Sm^{-1} and 150~200 μVK^{-1}, respectively [22]. The electronic thermal conductivity is proportional to carrier concentration and the lattice thermal conductivity is the only parameter that is slightly decoupling from the other parameters. So there are two general strategies to increase *zT*: maximize power factor and minimize lattice thermal conductivity.

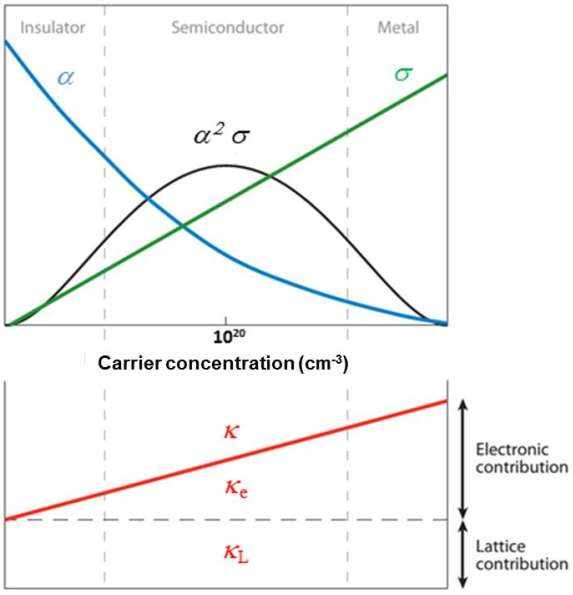

Figure 2.5: *The schematic dependence of α, σ, $\alpha^2\sigma$, and k on carrier concentration [21].*

Besides tuning carrier concentration, there are some special cases to improve the power factor $\alpha^2\sigma$, in which one quantity can be increased while the other remains constant or both quantities can be increased simultaneously. For instance, enhanced Seebeck

coefficient in Tl-doped PbTe and its alloys by introducing an impurity state in conduction band which causes distortions in the density of states near Fermi level [23, 24], improved carrier mobility through hoping conduction in In_2O_3-based mixed oxides [25], increased Seebeck coefficient through carrier energy filtering in Pt-Sb_2Te_3 nanocomposite [26], and simultaneous high Seebeck coefficient and high electrical conductivity through band convergence in Na doped $PbTe_{1-x}Se_x$ [27]. Although these strategies only work in very specific situations and are very difficult to be commonly applied in all different materials, they show the possibilities to further improvements in power factor and zT value.

In recent years, reducing lattice thermal conductivity κ_L has been the most effective way to improve zT value. As discussed above, lattice thermal conductivity is the only parameter decoupled from the electronic structure. Based on kinetic theory, the lattice thermal conductivity is given by,

$$\kappa_L = \frac{1}{3} C_V v l = \frac{1}{3} C_V v^2 \tau \quad (l = v\tau) \tag{2.11}$$

where C_V is the heat capacity, v is the phonon velocity, l is the phonon mean free path and τ is the phonon relaxation time. The phonon velocity is estimated by the low frequency speed of sound ($v_s \propto \sqrt{B/\rho}$), where B is the appropriate elastic modulus and ρ is the density of the material [28]. Generally, low lattice thermal conductivity can be achieved by finding new materials with high density and soft bonds (low v_s) or introducing extra phonon scattering into known materials (reducing τ). For a certain material, phonons have a distribution of different wavelengths and mean free paths, including short, medium and

long wavelength phonons. The phonons can be effectively scattered, if the size of scattering center is comparable to the mean free path. For instance, point defects, nano-inclusions and grain boundaries are effective to scatter short, medium and long wavelength phonons, respectively.

A recent report on Na-doped PbTe-SrTe solid solution shows a method of all-scale hierarchical architectures to reduce thermal conductivity. As shown in Figure 2.6, point defects, nano-inclusions and grain boundaries are combined together in a single bulk material to scatter different wavelength phonons. The lattice thermal conductivity was reduced by 55 % and zT value reached 2.2 at 900 K [5]. In term of developing materials with these featured microstructures, there are several effective techniques including ball milling (BM), melt spinning (MS), self-propagating high-temperature synthesis (SHS) and spark plasma sinter (SPS).

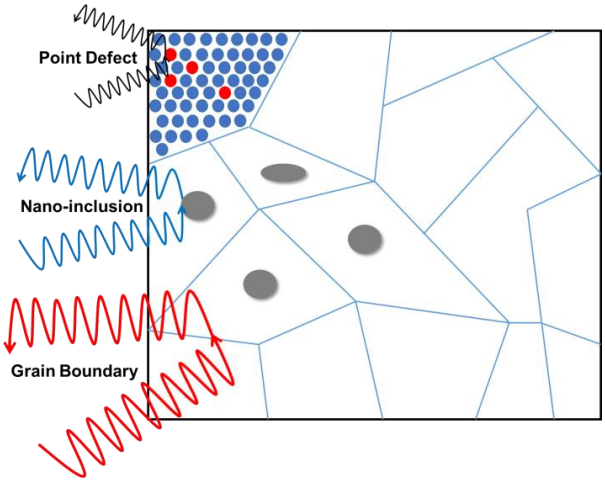

Figure 2.6: *The schematic of different wavelength phonons scattering (adapted from reference [29]).*

2.4 Traditional Thermoelectric Materials

2.4.1 Introduction

According to the working temperature, thermoelectric materials can be classified as low-temperature (<400 K), mid-temperature (400 K~900 K) and high-temperature (>900 K) ranges. The typical materials and their thermoelectric performances for each temperature range are shown in Figure 2.7, which will be reviewed below.

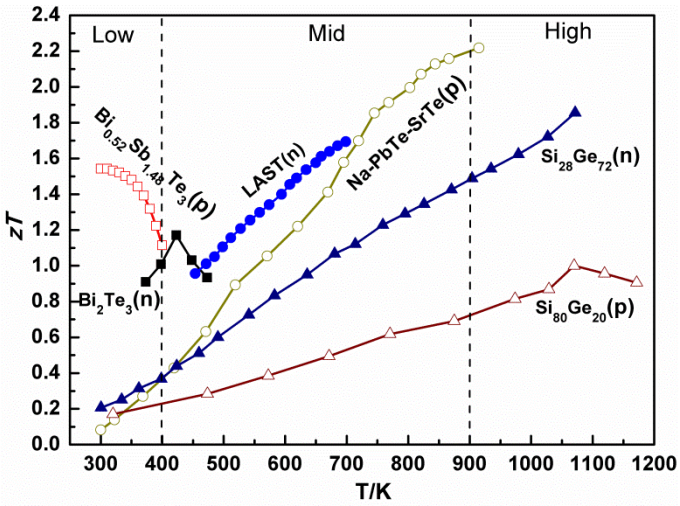

Figure 2.7: *Thermoelectric performance of typical material for different temperature ranges (adapted from reference [5, 30, 31, 32, 34, 35]).*

2.4.2 Bismuth Telluride

Bi_2Te_3-based alloys are the best thermoelectric materials in the low-temperature range and are the most widely used thermoelectric materials up to now. Bi_2Te_3 is a narrow gap semiconductor ($E_g \approx 0.15$ eV). It crystallizes with rhombohedral space group $R\bar{3}m$

with layered structure. As shown in Figure 2.8, the layers are connected by van der Waals forces along the c-axis and each layer is comprised of five atomic layers (Te1-Bi-Te2-Bi-Te1) [20]. Due to the layered structure, single crystal and zone melt prepared Bi_2Te_3 samples show anisotropic properties and very poor mechanical properties. Thus, recent research has focused more on polycrystalline materials and significant enhancements have been made in the thermoelectric properties of both n-type and p-type Bi_2Te_3 alloys. For instance, n-type Bi_2Te_3 prepared from flower-like nano-powders has achieved a zT value of 1.16 at 423 K and the average zT value is larger than 0.9 over a wide temperature range from 373 K to 498 K [30]; the p-type $Bi_{0.52}Sb_{1.48}Te_3$ alloy prepared by melt-spinning and SPS has a very high zT value of 1.56 at 300K, due to its unique microstructure and low thermal conductivity [31].

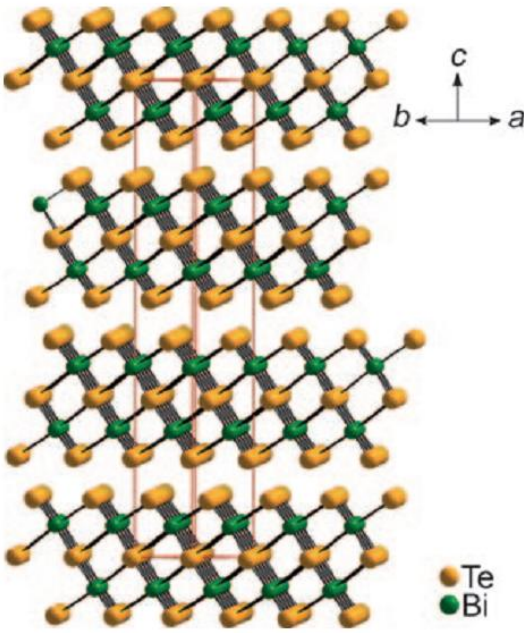

Figure 2.8: *The crystal structure of Bi_2Te_3 [20].*

2.4.3 Lead Telluride

PbTe and its alloys are well-known for their high thermoelectric performance in the mid-temperature range and play an important role in deep space exploration. PbTe has a simple cubic crystal structure with lattice parameter a = 6.462 Å. The high symmetry of cubic structure is favorable for high Seebeck coefficient and the constituent heavy elements contribute to a low thermal conductivity.

In the last decade, a wider research interest in the PbTe system has generated a lot of new and interesting results. $(PbTe)_m(Ag_{1-x}SbTe_2)_{1-m}$ alloy (n-type), also known as LAST, exhibits a zT value of 1.5 ~ 1.7 at 700 K [32]. Due to the nucleation and growth of a second phase, coherent nano-inclusions are formed in the PbTe matrix (See Figure 2.9(a)). The nano-inclusions are believed to scatter acoustic phonons while have minimal effect on charge carriers, which leads to high zT value. Heremans et al. reported a zT value of 1.5 at 773 K in Tl-doped PbTe (p-type) [33]. As seen in Figure 2.9(b), an additional resonant state was induced in the valence band near Fermi level by Tl, which gives a large rise in the Seebeck coefficient of PbTe. In 2011, the theory of electronic bands convergence was applied in Na-doped $PbTe_{1-x}Se_x$ alloys (p-type) to enhance the Seebeck coefficient [27]. Because of the large density-of-states effective mass resulting from high valley degeneracy of valence bands (Figure 2.9(c)), an outstanding zT value of 1.8 was achieved at 850 K. Recently, Biswas et al. reported a further enhanced zT value of 2.2 in Na-doped PbTe-SrTe system (p-type) [5]. By introducing multi-scale scattering sources

(atomic-scale point defects, nano-scale precipitates and meso-scale grain boundaries) in bulk material (See Figure 2.9(d)), the phonons are effectively scattered and the maximum reduction of lattice thermal conductivity was achieved in PbTe.

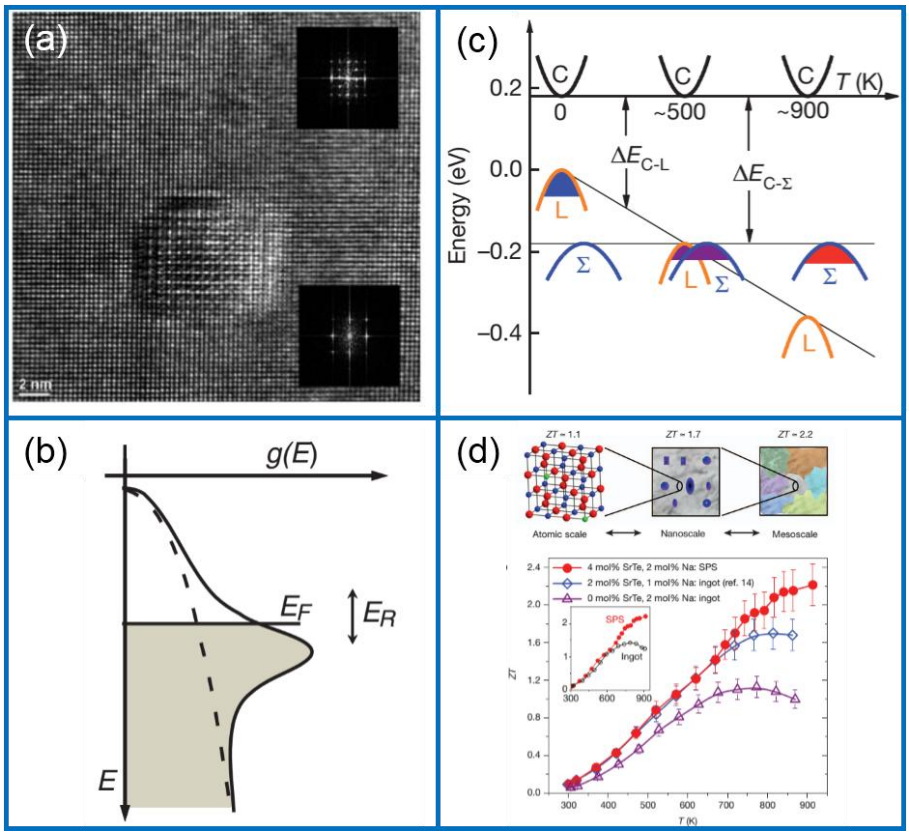

Figure 2.9: *(a) The TEM of nano-inclusion in LAST [32]; (b) schematic of a Tl-related level increasing the density of states in pure PbTe [33]; (c) schematic of valence bands convergence in* $PbTe_{0.85}Se_{0.15}$ *[27]; (d) all-length-scale hierarchy in PbTe [5].*

2.4.4 Silicon Germanium Alloy

The first thermoelectric material that was studied for high-temperature application is silicon germanium (SiGe) alloy. Since the 1970s, NASA has used SiGe alloys in radioisotope thermoelectric generators (RTGs), with a zT value of 0.5 (p-type) and 0.9 (n-type) [18]. Nowadays, with the development of nanostructuring techniques, the thermoelectric performance of both p-type and n-type SiGe alloys has been further improved. Nanostructured B-doped $Si_{80}Ge_{20}$ alloy (p-type) has achieved a zT of 1 at 1073-1173K [34], while nanostructured P-doped $Si_{72}Ge_{28}$ alloy (n-type) has achieved a zT value of 1.84 at 1073 K [35].

2.4.5 Conclusions

The development of nanostructuring techniques and band engineering theories has led to many impressive results in wide range of established thermoelectric materials. The high zT values give more confidence in developing thermoelectric devices with competitive efficiency. However, it is worthy to note that many of the state of the art thermoelectric materials contain very rare metals, such as Te which is only 0.001ppm in the Earth's crust. The high cost of thermoelectric devices is major barrier to their increased commercialization. Therefore, it is necessary to search for new thermoelectric materials containing low cost and abundant elements. Sulfides could be a potential replacement of tellurium-contained thermoelectric materials.

2.5 Thermoelectric Sulfides

2.5.1 Introduction

Sulfur is one of the most abundant elements in Earth's crust, and it is at least 100000 times more abundance than tellurium. The low price, high abundance and non-toxicity of sulfur have led to an increasing interest in their thermoelectric properties. In recent years, many sulfide systems have been explored as thermoelectric materials. The reported thermoelectric properties of sulfides are promising for medium-high temperature applications (400~1000 K). The state-of-the-art thermoelectric sulfides will be reviewed below.

2.5.2 Copper Sulfide

For many years, research on copper sulfide $Cu_{2-x}S$ has focused on its complex crystal structures and photovoltaic applications. In 2012, Liu et al. reported high thermoelectric performance in the super-ionic phase of p-type $Cu_{2-x}Se$ with a zT value of 1.5 at 1000K [36]. The special 'liquid-like' behavior of copper ions leads to an intrinsically low lattice thermal conductivity. As the analogue of $Cu_{2-x}Se$, $Cu_{2-x}S$ has the similar crystal structure and liquid-like behavior. The Cu_2S has three phases which can be seen from the Cu-S phase diagram (Figure 2.10). It has a α-Chalcocite phase (αCh) below 370 K, a β-Chalcocite phase (βCh) between 370 K and 700 K, and a cubic Digenite phase (Dg)

above 700K, respectively [37]. It also can be seen that the Dg phase is stable over an extensive composition range between $Cu_{2.02}S$ and $Cu_{1.732}S$ at high temperatures, which allows using Cu-deficiency to adjust the carrier concentration. The liquid-like state appears in cubic phase, which can be seen in Figure 2.11 (a). Sulfur atoms form a cubic sublattice and the copper ions can move freely as liquid within the frame, which will show strong phonon scattering and additional reduction in specific heat capacity [36]. The thermal conductivities of $Cu_{2-x}S$ samples were reported to be extremely low, below 0.6 $Wm^{-1}K^{-1}$ from 300 K to 1000 K (Figure 2.11 (b)). And a maximum zT value of 1.6 is obtained at 1000 K in p-type $Cu_{1.97}S$ sample [12]. The high mobility of Cu ions contributes to excellent thermoelectric performance, but it also causes severe degradation when the samples is exposed to currents and voltages [38]. This will be a critical problem for TE devices.

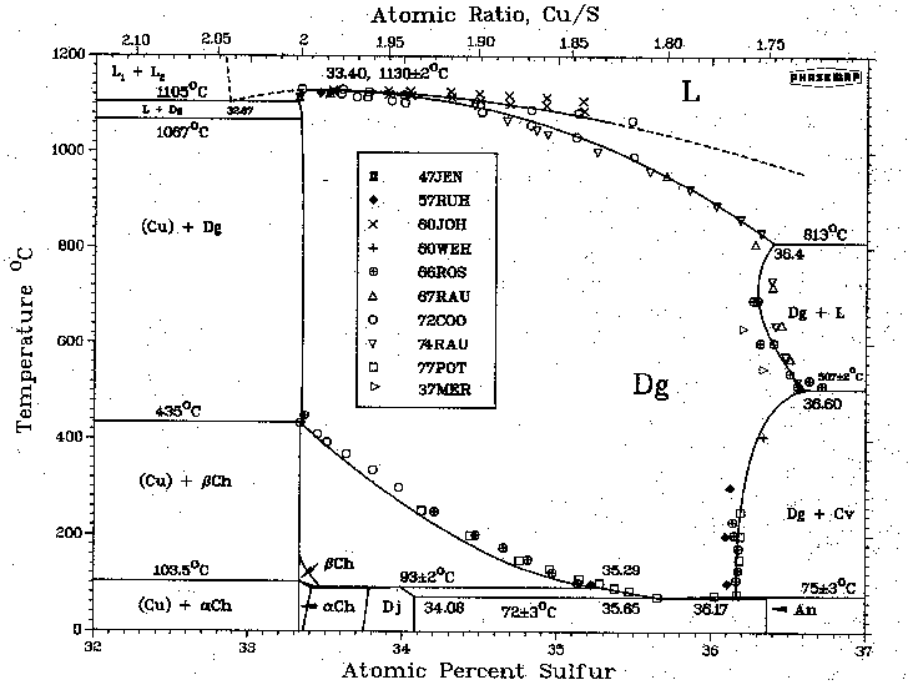

Figure 2.10: *The Cu-S phase diagram [37].*

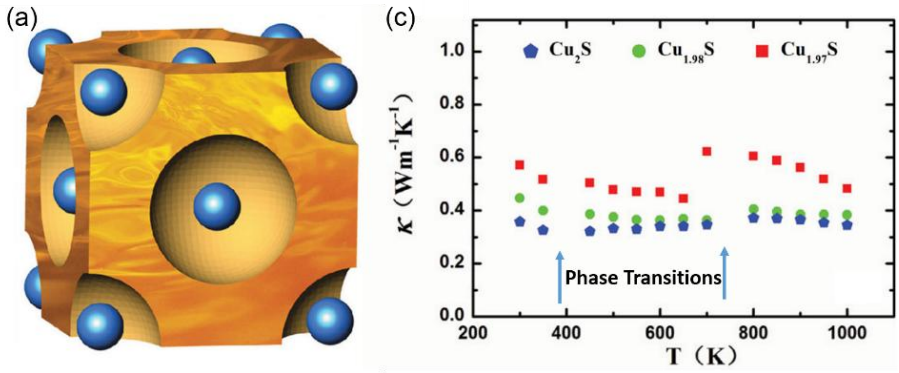

Figure 2.11: *(a) Crystal structure of cubic phase of Cu_{2-x} S. The blue spheres represent sulfur atoms and the liquid-like copper ions (orange) travel freely within the sulfide sublattice; (b) temperature dependence of thermal conductivity in $Cu_{2-x}S$ [12].*

2.5.3 Lead Sulfide

Lead sulfide actually is one of the earliest compounds to have its thermoelectric properties studied. The story begins at least as far back as 1822, when Seebeck proposed PbS as the n-type part of a thermoelectric series. Later, in 1940, Maslakovets reported thermoelectric generators based on PbS thermoelements with a conversion efficiency of 3 % [39]. However, with the discovery of good thermoelectric performance in Bi_2Te_3, there was no further research on PbS until recent years. PbS, also known as the mineral Galena, is isostructural to PbTe possessing the cubic structure with lattice parameters of 5.94 Å. Compared with PbTe, PbS has a larger band gap of 0.41 eV and a higher melting point of 1391 K, which is promising to be used in thermoelectric generator at higher temperature. Through carrier concentration optimizing, a maximum *zT* value of 0.7 at 850 K for n-type

PbS was reported by Wang [40]. And the *zT* value is predicted to keep increasing with temperature and reach 1 at 1000 K. Zhao et al. reported enhanced thermoelectric performance in PbS by second phase nanostructures [41]. From the phase diagram shown in Figure 2.12 (a), Bi_2S_3 and Sb_2S_3 are found to have very low solubility in the solid state, but complete solubility in the liquid state. In this case, phase separation and precipitation of the second phases can be achieved by cooling after reaching the solid state solubility limit. By proper heat treatment, the nano-precipitates are formed in PbS matrix as shown in Figure 2.12 (b), which leads to an effective suppression of lattice thermal conductivity. Combined with $PbCl_2$ doping, a maximum *zT* value of 1.06 was achieved at 923 K for a n-type PbS sample with 1 mol. % Sb_2S_3. Overall, PbS is very promising in terms of thermoelectric performance, but the toxicity of Pb is still an issue for future applications.

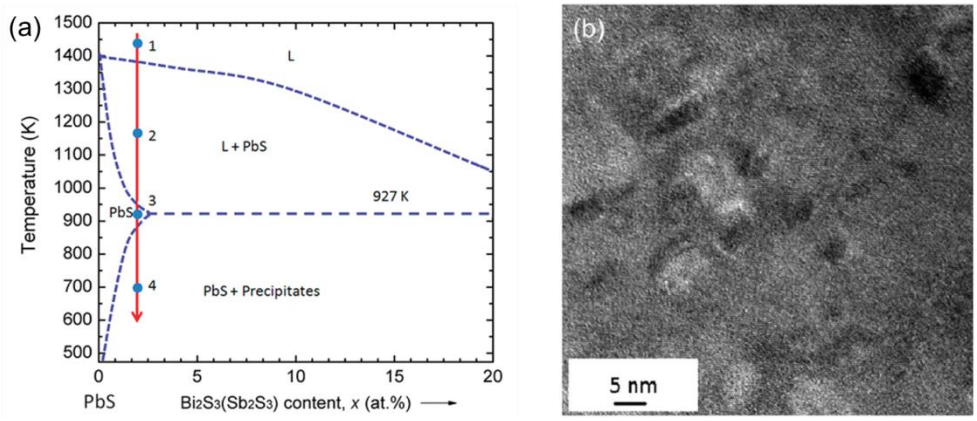

Figure 2.12: *(a) Binary phase diagram of PbS-Bi_2S_3(Sb_2S_3); (b) high-resolution TEM images of PbS with 1.0 mol. % Sb_2S_3 and doped with 1.0 mol. % $PbCl_2$ [41].*

2.5.4 Bismuth Sulfide (Bi_2S_3)

As the analogue of bismuth telluride, bismuth sulfide belongs to the same VA–VIA group compounds, possessing a similar layered structure. It has a direct band gap E_g of 1.3 eV, which is much larger than that of Bi_2Te_3 (0.15 eV). Because of its poor electrical conductivity (two orders lower than that of Bi_2Te_3), pristine Bi_2S_3 showed an unattractive *zT* value of 0.06 at 300 K from early research [42]. However, recent attempts show improved thermoelectric properties of the Bi_2S_3 due to its high Seebeck coefficient and low thermal conductivity. Yu et al. investigated n-type polycrystalline Ag-doped Bi_2S_3, prepared by mechanical alloying (MA) combined with spark plasma sintering (SPS). The electrical conductivity of Bi_2S_3 is increased largely by Ag doping and a sample with fine grains of 100~500nm showed a very low thermal conductivity. An enhanced maximum *zT* value of 0.25 was achieved at 573 K for the $Bi_{1.99}Ag_{0.01}S_3$ sample [43]. Chmielowski et al. reported a higher *zT* value of 0.6 for 0.25 mol. % $BiCl_3$ doped Bi_2S_3 (n-type) at a higher temperature of 700 K [44]. The stability of $BiCl_3$-doped Bi_2S_3 against thermal stress and current stress was investigated, and it was found to be promising to be used in thermoelectric devices. Recently, Liu et al. reported enhanced thermoelectric performance of n-type Bi_2S_3 by Br doping and Cu nanoparticles [45]. The electrical conductivity was increased with Br doping and Cu intercalation. Figure 2.13 shows the temperature dependence of lattice thermal conductivity and the TEM image of Cu nanoparticles. Because of the strong point defects produced by Br alloying and Cu nanoparticles, the lattice thermal conductivity of Bi_2S_3 with 1 mol. % CuBr was reduced

by more than 50 % in the investigated temperature range. A maximum *zT* of 0.72 at 773 K was obtained for a 0.5 mol. % $CuBr_2$ doped sample parallel to the press direction, which is the highest *zT* value ever reported for Bi_2S_3 system.

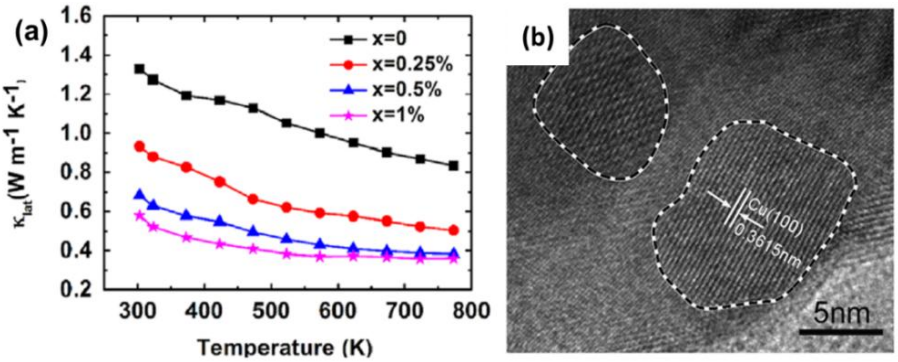

Figure 2.13: *(a) Temperature dependence of lattice thermal conductivity for Bi_2S_3 with $CuBr_2$ doping; (b) high magnification TEM image showing the Cu-nanoparticles [45].*

2.5.5 Tin Sulfide (SnS)

SnS belongs to the IV–VI compounds [GeS, GeSe, SnS, SnSe], which have the orthorhombic structure with the space-group of *Pnma*. It has lattice parameters of a = 3.99 Å, b = 4.34 Å and c = 11.2 Å. There are eight atoms per unit cell forming double-layer planes along the c-axis, as seen in Figure 2.14 [46]. The atoms in each layer are covalently bonded with the three neighboring atoms, while the layers are connected by long interactions of S and Sn.

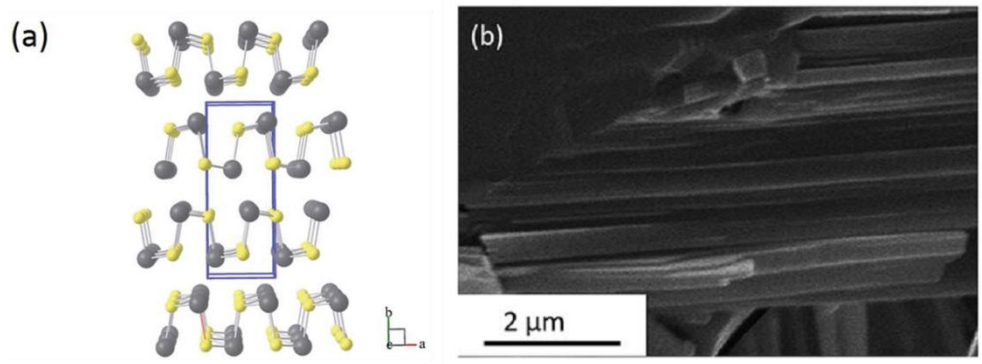

Figure 2.14: *(a) Crystal structure of SnS; (b) the fractured surface of SnS [47].*

The report on ultra-high *zT* value of 2.6 at 923 K in p-type SnSe single crystal [10], has led to a recent interest in thermoelectric properties of SnS. A pristine SnS sample prepared by mechanical alloying and SPS showed an intrinsically low thermal conductivity (below 1.0 $Wm^{-1}K^{-1}$) and a high Seebeck coefficient [48]. Tan et al. reported the enhanced thermoelectric performance of Ag-doped SnS (p-type) [47]. With 0.5 mol. % Ag doping, the power factor is improved by 300 % at 823 K. Meanwhile, the thermal conductivity is reduced due to the point defects introduced by Ag doping. A maximum *zT* value of 0.6 is achieved at 923K in 0.5 mol. % Ag doped SnS.

2.5.6 Titanium Sulfide

Besides bismuth sulfide and tin sulfide discussed above, titanium sulfide is another compound with layered structure that has been studied for thermoelectric applications. The crystal structure of TiS_2 is shown in Figure 2.15 (a), which possesses a hexagonal

layered structure ($P\bar{3}m1$). In each layer S and Ti atoms are covalently bonded and the layers are connected by weak S–S van der Waals forces along the *c* axis [49].

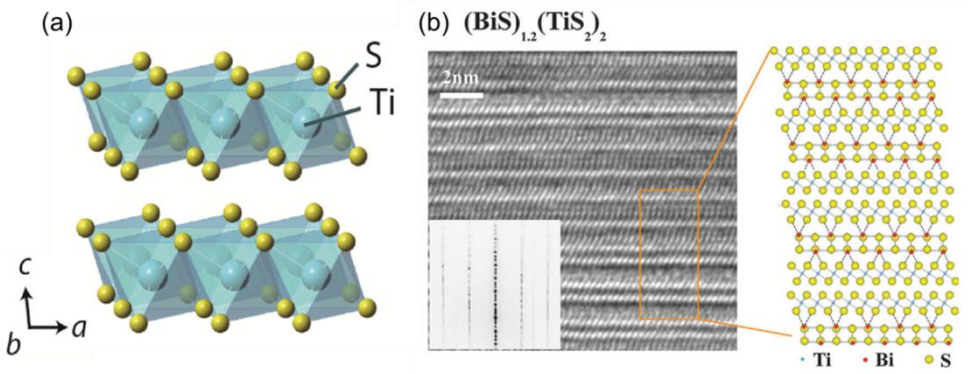

Figure 2.15: *(a) Crystal structure of TiS_2 [50]; (b) TEM images and simulated crystal structure of $(BiS)_{1.2}(TiS_2)_2$ [49].*

Moreover, this van der Waals gap can be filled by various guest atoms and guest layers, which makes TiS_2 well known as an intercalation compound. Intercalation has been proved to be an effective way to tune electrical properties and reduce lattice thermal conductivity of TiS_2. For example, Ti intercalation in TiS_2 (also called self-intercalation) can realize electron doping and phonon scattering at the same time. A maximum *zT* value of 0.48 is obtained at 700 K in n-type $Ti_{1.025}S_2$ [51]. Cu intercalation shows similar behavior in TiS_2, and a slightly higher *zT* value of 0.5 was reported in n-type $Cu_{0.1}TiS_2$ [52]. Beside atom intercalation, Guilmeau et al. reported misfit layer compounds $(MS)_{1+x}(TiS_2)_2$ by intercalating guest layer of MS (M = Pb, Sn, Bi) in TiS_2 [49]. Compared with atom intercalation, the layer intercalation seems more effective in phonon scattering.

For instance, $(BiS)_{1.2}(TiS_2)_2$ compound was found with extensive planar defects as seen in Figure 2.15 (b). A thermal conductivity of about 0.5 $Wm^{-1}K^{-1}$ was reported for this compound. However, the intercalated layers have strong electron transfer effect in $(BiS)_{1.2}(TiS_2)_2$, which causes a reduction in the power factor and an increase in the electronic thermal conductivity. So the *zT* value turns out to be very low.

2.5.7 Tetrahedrite

Tetrahedrite is a natural mineral which has the base composition of $Cu_{12}Sb_4S_{13}$. In recent years a lot of research has been done on tetrahedrite, due to its advantages of: (1) high symmetric crystal structure (cubic) with a large unit cell; (2) intrinsically low thermal conductivity; and (3) existence as a mineral with environmentally friendly and earth abundant element of sulfur.

The crystal structure of tetrahedrite ($Cu_{12}Sb_4S_{13}$) was confirmed by Wuensch in 1963 [53], and it possesses a complex cubic structure (space group $I\bar{4}3m$) with a large unit cell of 58 atoms as shown in Figure 2.16. There are two different Cu sites, where half of the Cu atoms occupy four-coordinate, distorted tetrahedral sites and the other half occupy three-coordinate triangular sites. The Sb atoms occupy tetrahedral sites but are bonded to only three S atoms, leaving lone pair electrons in the structure.

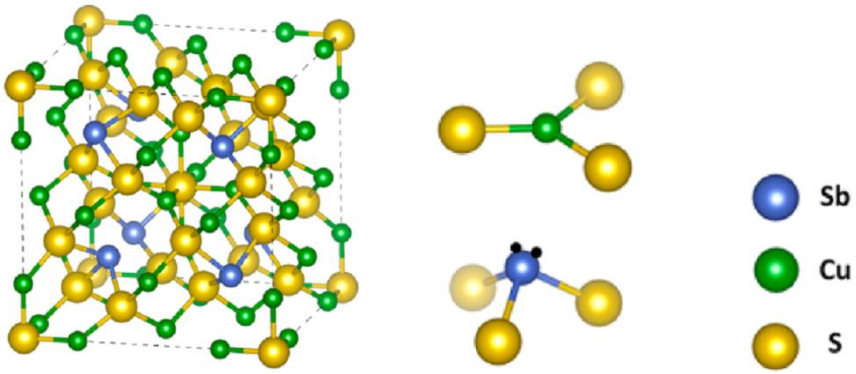

Figure 2.16: *Crystal structure of $Cu_{12}Sb_4S_{13}$ (left). The three-coordinate Cu atoms and the three-coordinate Sb atoms with lone-pair electrons (right) [54].*

The intrinsically low thermal conductivity in tetrahedrite is believed to derive from the three-coordinate Cu and Sb atoms. As seen in Figure 2.17, the calculation of atomic charges and bonding revealed the off-center position of Cu in [CuS3] planar induced by lone-pair electrons of Sb [55]. The Cu (48h) is estimated to have a vibration with energy of 4 meV, along the out-of-plane direction. This anharmonic rattling of Cu suppresses the acoustic phonon branch and contributes to the low thermal conductivity. According to simple valence counting, the formula of $Cu_{12}Sb_4S_{13}$ can be written as $Cu_{10}^{+}Cu_{2}^{2+}Sb_{4}^{3+}S_{13}^{2-}$ indicating 10 Cu atoms are monovalent and 2 Cu atoms are divalent. But the actual valence of Cu is still under debate, as the metallic behavior of $Cu_{12}Sb_4S_{13}$ implies that it is intrinsically electron deficient. This means that at least some of the nominally divalent Cu ions are in a monovalent or mixed valent state. The first-principles calculation of the electronic band structure of $Cu_{12}Sb_4S_{13}$ was reported [15], and it can be seen in Figure 2.18. It explains the metallic behavior of $Cu_{12}Sb_4S_{13}$ as the Fermi level lies in the valence

band. Besides, the valence band maximum (VBM) shows band degeneracy due to the high symmetry cubic structure of $Cu_{12}Sb_4S_{13}$, which is favorable for thermoelectric properties [27].

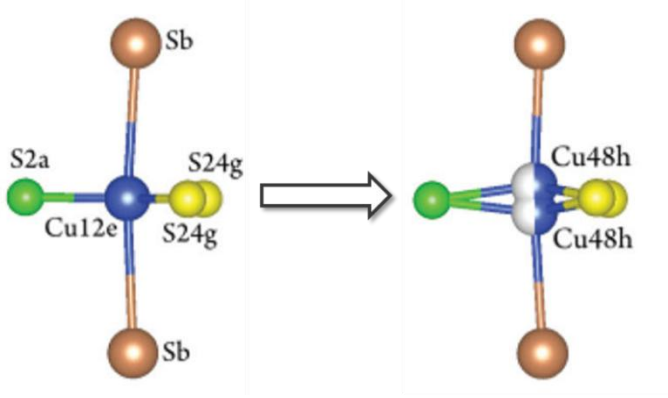

Figure 2.17: *Side view of the trigonal bipyramid in $Cu_{12}Sb_4S_{13}$ with Cu in the off-centered position [55].*

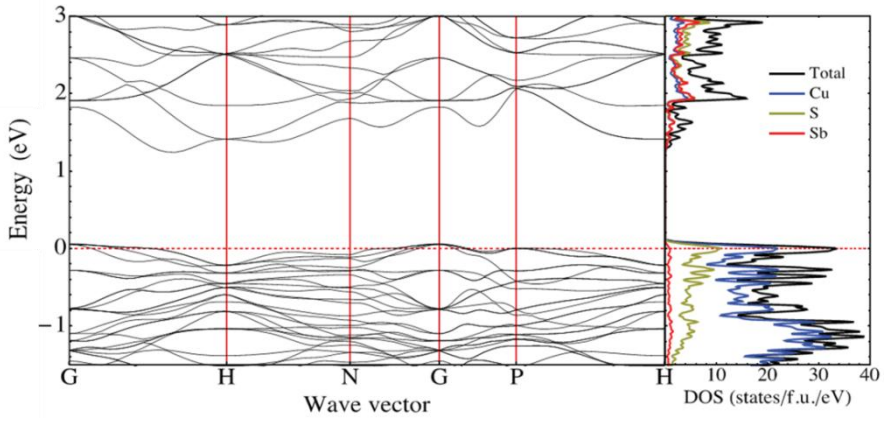

Figure 2.18: *Electronic band structure and density of states (DOS) of $Cu_{12}Sb_4S_{13}$ [15].*

In 2012, Suekuni et al. reported the low-temperature thermoelectric properties of synthetic tetrahedrite [56]. $Cu_{12}Sb_4S_{13}$ has a wide composition range, as up to 1/6 of the

Cu atoms can be substituted by various transition metals. A series of samples of $Cu_{10}Tr_2Sb_4S_{13}$ (Tr = Mn, Fe, Co, Ni, Cu and Zn) were synthesized by melting combined with hot pressing. The obtained bulk samples are not very dense with a relative density of 75 – 80 %, and the impurity phase of Cu_3SbS_4 is detected by XRD as shown in Figure 2.19 (a). Despite the low density and impurity, the resistivity, Seebeck coefficient and thermal conductivity of $Cu_{10}Tr_2Sb_4S_{13}$ samples were investigated at low temperature (Figure 2.19 (b)). All the samples show p-type conducting behavior and the electrical properties of $Cu_{12}Sb_4S_{13}$ are tunable by different substitutions on Cu sites. All the samples have very low lattice thermal conductivities, which are around 0.4 $Wm^{-1}K^{-1}$ at room temperature. This report concluded that tetrahedrite is promising for thermoelectric applications.

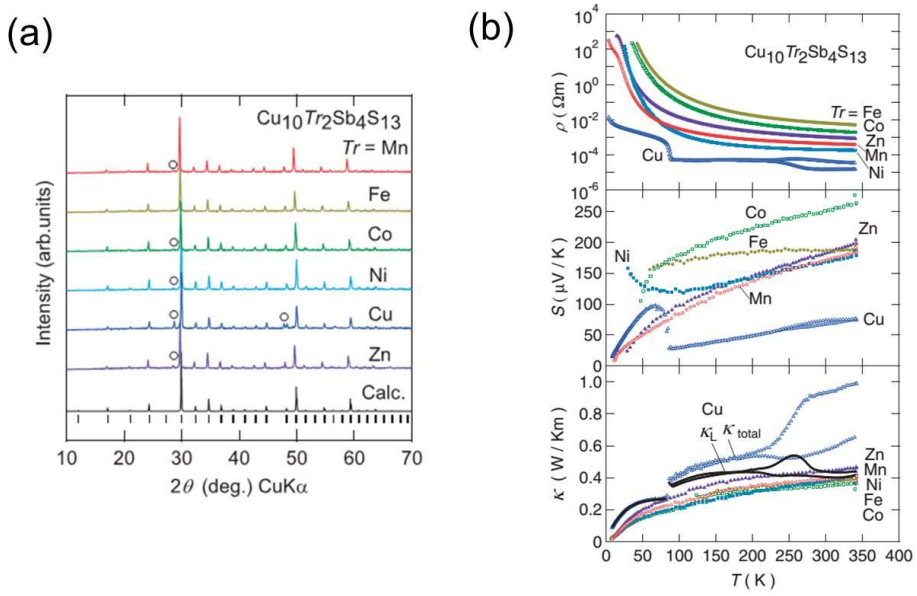

Figure 2.19: *(a) XRD patterns of $Cu_{10}Tr_2Sb_4S_{13}$ samples; (b) The temperature dependence of resistivity, Seebeck coefficient and thermal conductivity of $Cu_{10}Tr_2Sb_4S_{13}$ samples [56].*

More recently, the high temperature thermoelectric properties for both natural mineral tetrahedrite and synthesized tetrahedrite were reported, which highlighted the potential use of tetrahedrite in thermoelectric applications. Generally, the synthetic tetrahedrite powder is prepared by solid-sate reaction or melting in sealed tube from stoichiometric single elements and then hot-pressing or SPS is used for solidification [17, 54, 56-63]. A single phase and dense bulk sample of tetrahedrite can be obtained. This intrinsic tetrahedrite has metal-like behavior with very high hole concentration, which is not ideal for thermoelectric performance. So different dopants have been reported to reduce the hole concentration, which can optimize the power factor and reduce the electronic contribution to the total thermal conductivity. The *zT* value of tetrahedrite can be enhanced through different doping, which can be seen in Figure 2.20.

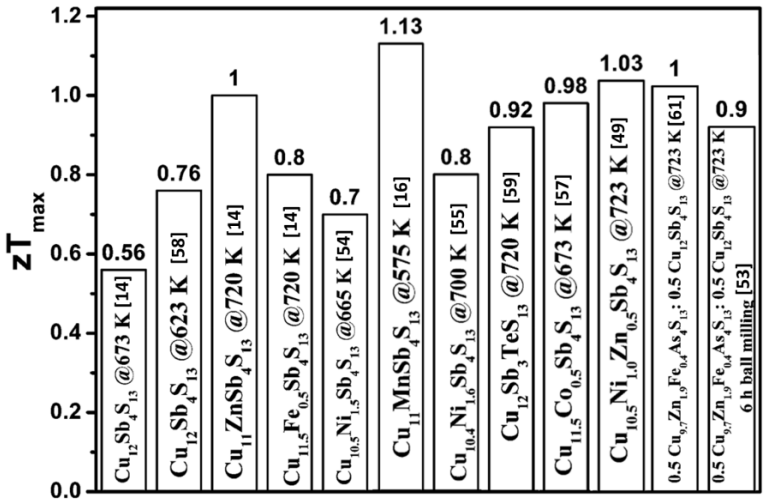

Figure 2.20: *Maximum zT values reported for tetrahedrite materials [64].*

The best thermoelectric performance of tetrahedrite was reported by Heo [17]. A series compounds of $Cu_{10}TM_2Sb_4S_{13}$ (TM=Mn, Fe, Co, Ni and Zn) were first studied. The temperature dependence of electrical conductivity, Seebeck coefficient, thermal conductivity and *zT* value of $Cu_{10}TM_2Sb_4S_{13}$ are shown in Figure 2.21. Compared with pure tetrahedrite, all the doped samples show lower electrical conductivities and higher Seebeck coefficients. Due to the reduction in electronic thermal conductivities and additional phonon scattering derived from the random distribution of the TMs in the materials, the doped samples show very low thermal conductivities, which are below 0.3 $Wm^{-1}K^{-1}$ from 325 K to 575 K. As Mn-doped sample has a moderate Seebeck coefficient and a relatively high electrical conductivity, it achieves a higher *zT* value than the other samples.

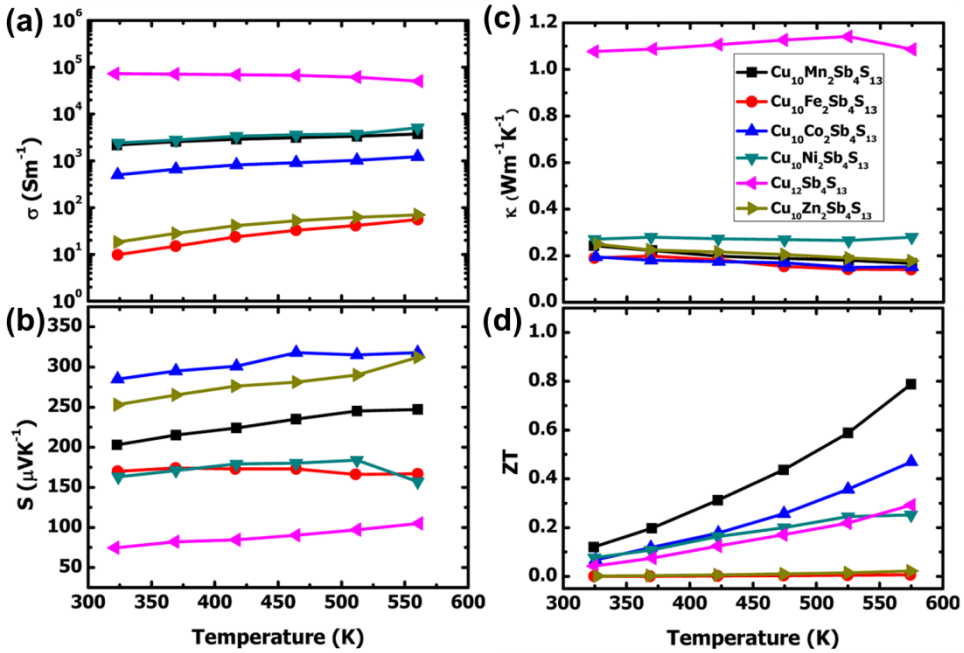

Figure 2.21: *The temperature dependence of (a) electrical conductivity, (b) Seebeck coefficient, (c) thermal conductivity and (d) zT value of $Cu_{10}TM_2Sb_4S_{13}$ samples [17].*

Following the above results, further research on tetrahedrite with different Mn doping concentrations was carried out. The thermoelectric properties at 575 K of $Cu_{12-x}Mn_xSb_4S_{13}$ (x = 0, 0.5, 1.0, 1.5 and 2.0) samples are shown in Figure 2.22. With increasing amount of Mn, the electrical conductivity decreases while Seebeck coefficient increases. The fine-tuned electrical transport properties and reduced thermal conductivity realize an enhanced zT = 1.13 in $Cu_{11}MnSb_4S_{13}$ sample, which is competitive with some conventional thermoelectric materials.

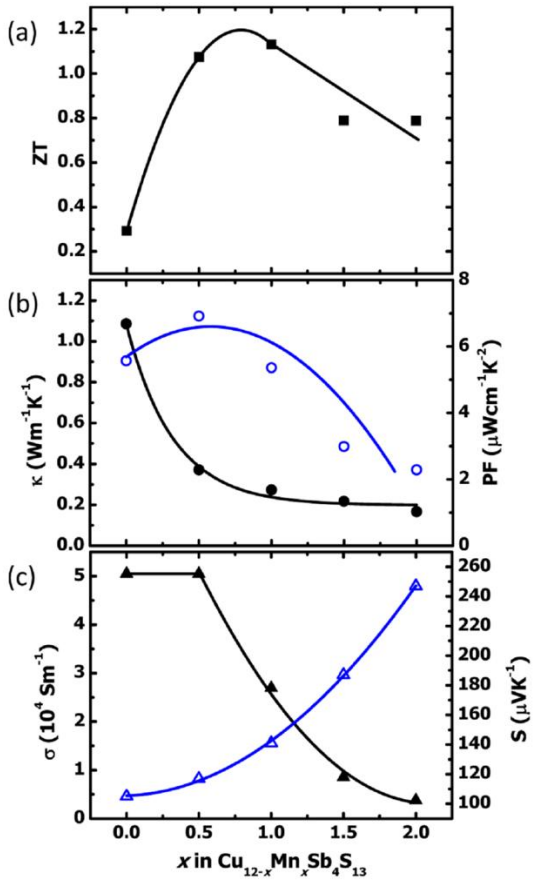

Figure 2.22: *(a) The zT value, (b) thermal conductivity and power factor, (c) electrical conductivity and Seebeck coefficient as a function of Mn concentration in $Cu_{12-x}Mn_xSb_4S_{13}$ samples at 575 K [17].*

Besides the good performance reported in synthetic tetrahedrite, it is also promising to use natural tetrahedrite minerals as thermoelectric materials. Generally, the synthesis of tetrahedrite is from high-purity starting materials and the process is time consuming. In contrast, using natural tetrahedrite minerals is much easier and cheaper. Lu et al. [57, 65] reported the thermoelectric properties of tetrahedrites based on natural minerals. However, natural tetrahedrite minerals exist as the solid solution of $Cu_{12}Sb_4S_{13}$ and $Cu_{12}As_4S_{13}$ with Fe or Zn substitution on Cu sites. In Lu's work, two natural mineral specimens (NM1 and NM2) were randomly chosen from a mineral specimen company [57]. By using energy-dispersive X-ray analysis (EDX), the compositions of NM1 and NM2 are determined to be $Cu_{10.5}Fe_{1.5}As_{3.6}Sb_{0.4}S_{13}$ and $Cu_{9.7}Zn_{1.9}Fe_{0.4}As_4S_{13}$, respectively. Due to the high concentration of Fe or Zn, the natural minerals have very low carrier concentrations and very poor electrical conductivities. In order to achieve optimum carrier concentration for thermoelectricity, a method of mixing the natural mineral specimens and synthetic tetrahedrite ($Cu_{12}Sb_4S_{13}$) was developed. The NM (natural mineral) powder and SYN (synthetic tetrahedrite) powder are mixed in mass ratios of 1:3, 1:1 and 3:1 and ball-milled for 30 min. The obtained bulk samples from hot-pressing were phase pure with relative densities above 98 %. The thermoelectric properties of mixed samples are shown in Figure 2.23. The closed symbols represent NM1 based samples and the open symbols represent NM2 based samples. The circles, squares and triangles represent samples containing 25 %, 50 % and 75 % of SYN, respectively. For both natural minerals, the resistivity and Seebeck coefficient decrease with increasing amount of synthetic

tetrahedrite. This indicates synthetic tetrahedrite can be used to adjust the composition and carrier concentration of natural minerals. The NM2 based samples have better electrical properties than that of MN1 based samples. A maximum *zT* value of 1 at 723 K was obtained in the sample containing 50 % NM2 and 50 % SYN, which is comparable to other p-type thermoelectric materials. As the natural tetrahedrite minerals are widespread and have a wide range of composition, there might be some natural minerals with suitable composition that can be directly consolidated with little effort. If so, it will reduce the cost for large scale thermoelectric applications.

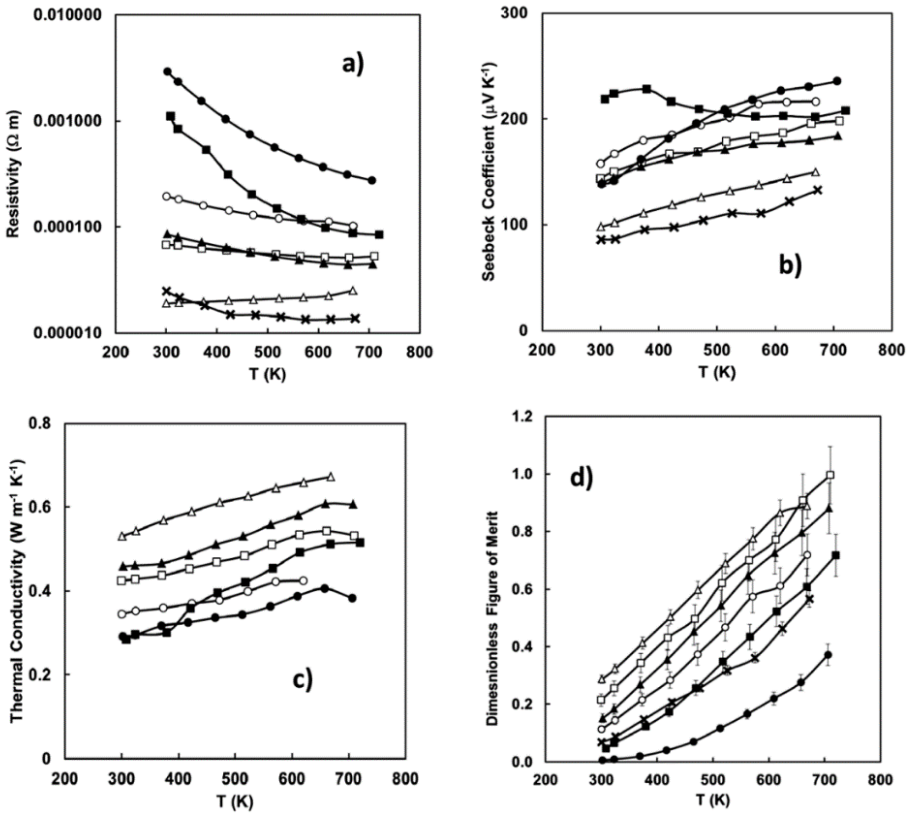

Figure 2.23: *The temperature dependence of (a) resistivity, (b) Seebeck coefficient, (c) thermal conductivity, and (d) zT value of natural mineral based tetrahedrites [57].*

2.5.8 Conclusions

The state-of-the-art thermoelectric sulfides were reviewed above. A summary of the best thermoelectric properties of each sulfide system can be seen in Figure 2.24. Although most of the sulfides have relatively low *zT* values when compared with selenides and tellurides, there are three sulfides, $Cu_{1.97}S$ [12], PbS [41] and $Cu_{11}MnSb_4S_{13}$ [17]; that have been reported to have *zT* values above 1. $Cu_{1.97}S$ exhibits very high *zT* value. Unfortunately, the migration of the Cu ions in this compound can cause serious degradation of the properties of the materials and devices. It will not suitable for applications unless this problem is resolved. As for the PbS system, the toxicity of Pb is a problem for mass market application. Overall, the good thermoelectric properties, earth-abundance and low-toxicity of tetrahedrite make it promising for thermoelectric applications. Thus, in this work, tetrahedrite ($Cu_{12}Sb_4S_{13}$) is chosen as a starting point for an extended research of Cu-Sb-S ternary compounds.

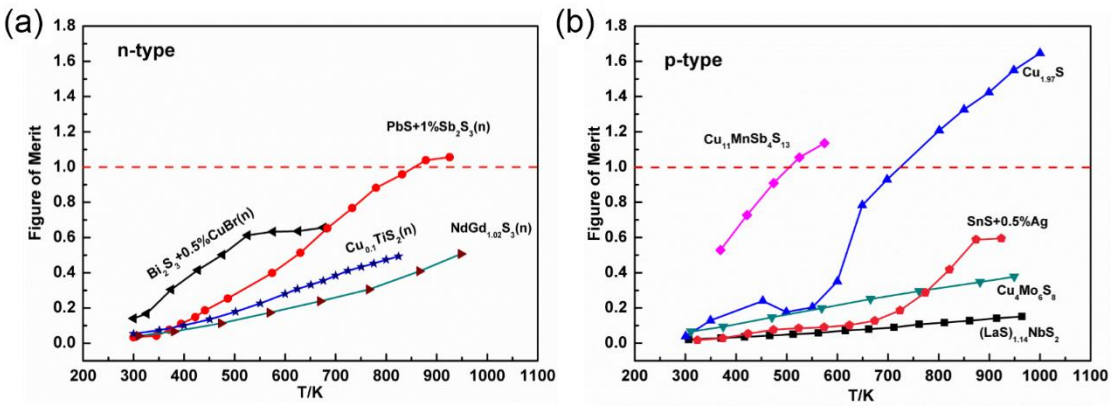

Figure 2.24: *The state-of-the-art thermoelectric sulfides (adapted from reference [12, 17, 41, 45, 47, 52]).*

2.6 Cu-Sb-S Ternary Compounds

2.6.1 Introduction

As discussed above, tetrahedrite ($Cu_{12}Sb_4S_{13}$) has many good properties for thermoelectric application, which leads our interest to the family of Cu-Sb-S ternary compounds. By searching the XRD crystallography database, it is found that four main phases exist in the Cu-Sb-S system, and they are $Cu_{12}Sb_4S_{13}$, $CuSbS_2$, Cu_3SbS_3 and Cu_3SbS_4. The phases and phase relations in the Cu-Sb-S system were studied by Skinner et.al in 1972 [66]. It was confirmed the all four ternary phases can form from pure elements. Figure 2.25 shows the phase relations in the Cu-Sb-S system at 500 ℃. It can be seen that the four phases are stable at 500 ℃ and they have very narrow composition filed except for $Cu_{12}Sb_4S_{13}$ which can form a copper rich phase. It indicates it is unlikely for the other three compounds to show non-stoichiometry. With studies at higher temperatures, it was found that $Cu_{12}Sb_4S_{13}$ breaks down at 543 ℃ and $CuSbS_2$, Cu_3SbS_3 and Cu_3SbS_4 melt at 553 ℃, 607.5 ℃ and 627 ℃, respectively. In terms of thermoelectric properties, there are very few reports about these compounds except for $Cu_{12}Sb_4S_{13}$, which has been intensively studied in recent years. These four compounds have the same constituent elements, but possess very different crystal structures and physical properties. It is worth trying to obtain a fundamental understanding between the structures and properties of these materials. It would be of interest to explore whether these three compounds are suitable for thermoelectric applications.

Abbreviation	Composition
cv	CuS
fcc	$Cu_{2-x}S$
Cu_{SS}	Copper solid-solution
β	Cu-Sb alloy
stb	Sb_2S_3
fm	Cu_3SbS_4
td	$Cu_{12}Sb_4S_{13}$
B	Cu_3SbS_3
cstb	$CuSbS_2$

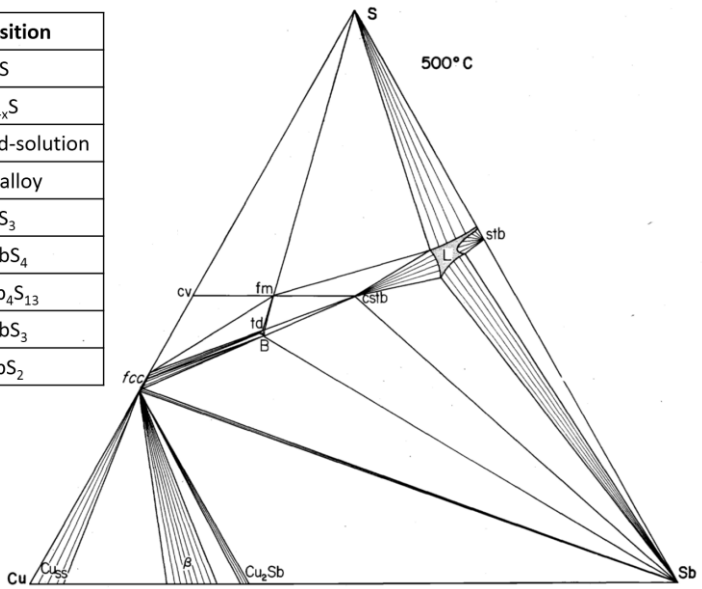

Figure 2.25: *Phase relations in the Cu-Sb-S system at 500 ℃. Compositions are plotted in atom percent. One-phase field appears as points or are stippled, two-phase fields are shaded by tie lines and three-phase fields are open [66].*

2.6.2 $CuSbS_2$ (Chalcostibite)

The $CuSbS_2$ compound, also known as the mineral Chalcostibite, has been studied as a promising earth-abundant photovoltaic absorber material. It has an orthorhombic structure with space group *Pnma* (no. 62) [67], which can be seen in Figure 2.26 (a). The Cu atom is four-coordinated forming CuS4 tetrahedron (blue). The Sb atom is five-coordinated forming SbS5 square pyramid (grey), leaving lone-pair electrons in the structure (Figure 2.26 (b)). This is the configuration predicted by assuming sp^3d^2 hybridization of orbitals on Sb, where Sb is six-coordinated with lone-pair electrons occupying one bonding site [68, 69]. The structure can be considered as SbS5 square

pyramids are edge sharing and forming continuous SbS2 chains along the b axis. The SbS2 chains are separated by CuS4 tetrahedrons which makes the square pyramids aligned to face one another, thus directing the Sb lone-pair electrons into the void separating the SbS5 square pyramids [67]. The stereochemical activity of the Sb $5s^2$ lone-pair electrons will cause considerable local distortions in the crystal structure. Also, it is believed to be the origin of low thermal conductivity reported in Sb containing ternary compounds [16, 55]. This implies $CuSbS_2$ could have an intrinsically low thermal conductivity. Recently, a reversible phase transition of $CuSbS_2$ from the orthorhombic structure to a triclinic type structure was observed under pressures above 11GPa [70]. The phase transition could generate some interesting physical properties under high pressure, which have not been studied.

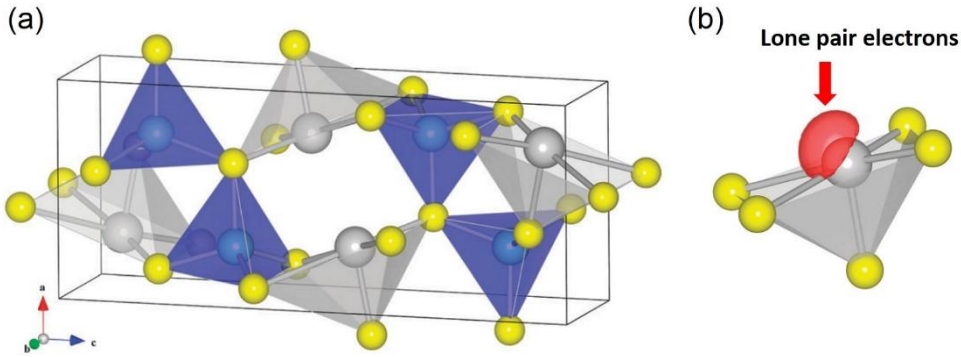

Figure 2.26: *(a) Structure of $CuSbS_2$ showing CuS4 tetrahedron (blue), SbS5 square pyramid (grey) and S atoms (yellow); (b) SbS5 square pyramid with lone-pair electrons (red) [67].*

The electronic band structure of $CuSbS_2$ has been reported. The band structure was calculated using first-principles DFT. The results indicate $CuSbS_2$ has an indirect band

gap. The calculated band gap is about 1.05 ~ 1.73 eV from different reports [67, 71, 72], which is large enough to prevent bipolar conduction for operating below its melting point (825 K). However, this large band gap might not be suitable for good thermoelectric materials, which generally have a small band gap below 1eV. Figure 2.27 shows the orbital-projected density of states for $CuSbS_2$. It can be seen the valence band maximum (VBM) is mainly composed of Cu-3d states, while the conduction band minimum is mainly composed of Sb-5p states [67]. The Fermi level lies in the band gap, and it is closer to the valence band maximum, indicating $CuSbS_2$ is a p-type semiconductor. As the Fermi level is about 0.5eV higher than the VBM, it could result in an intrinsic low hole concentration in $CuSbS_2$ [73]. But $CuSbS_2$ has been reported to have a large hole effective mass ($m^* = 3.7\ m_e$) [74], which suggests it will have a high Seebeck coefficient.

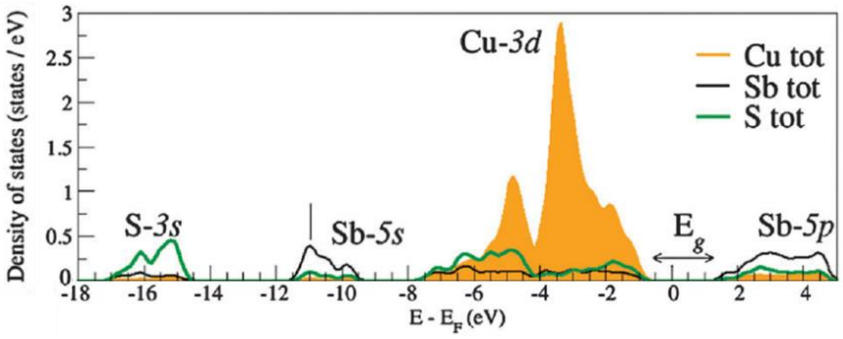

Figure 2.27: *Orbital-projected density of states for $CuSbS_2$ [67].*

Up to now there are very few reports about the thermoelectric properties of $CuSbS_2$. The low temperature resistivity of $CuSbS_2$ was reported by Wachtel and Noreika in 1980 [75]. As seen in Figure 2.28 (a), the resistivity of $CuSbS_2$ decreases exponentially with

increasing temperature, which is typical behavior for a semiconductor displaying intrinsic carrier excitation. It shows a relatively high resistivity around 40 Ωcm at room temperature, which must be reduced when developing $CuSbS_2$ as thermoelectric material. In 2013, the theoretical prediction of the thermoelectric properties for $CuSbS_2$ was reported by Vijay et al. [76]. The carrier concentration and temperature dependent Seebeck coefficients of $CuSbS_2$ were calculated by using Boltzmann transport theory, which can be seen in Figure 2.28 (b). The Seebeck coefficient increases with decreasing carrier concentration as in most TE materials. With a high hole concentration of 1.2×10^{20} cm^{-3}, the Seebeck coefficient was predicted to be 350 μVK^{-1} at 700 K, which is promising for good thermoelectric performance. However, there is no systemic research on thermoelectric properties of $CuSbS_2$.

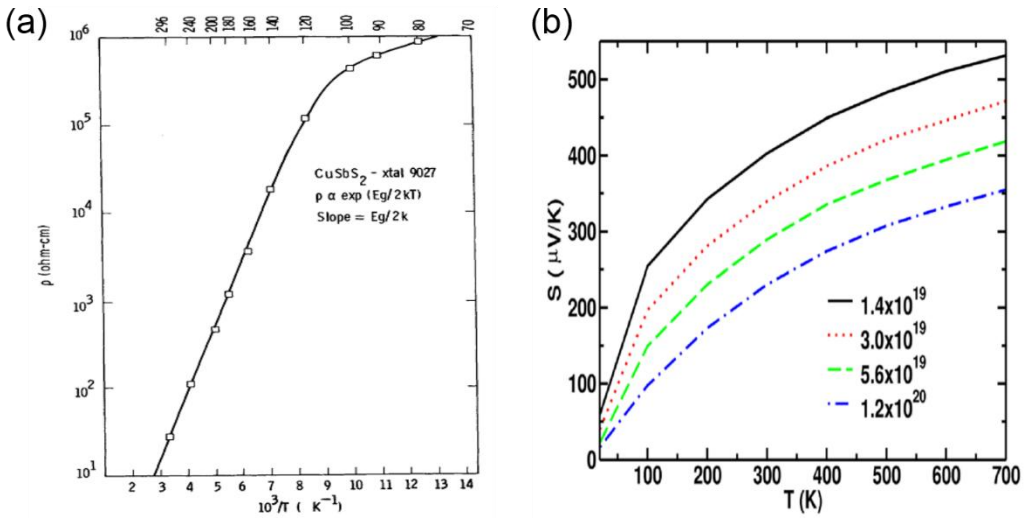

Figure 2.28: *(a)The temperature dependence of resistivity [75]; (b)The temperature dependence of theoretical Seebeck coefficient at different hole concentrations for $CuSbS_2$ [76].*

2.6.3 Cu_3SbS_3 (Skinnerite)

Skinnerite with composition of Cu_3SbS_3 has been explored as a potential photovoltaic absorber material due to its low-cost and low-toxicity [77-79]. Up to now there are no reports on its thermoelectric properties. However, its analog Cu_3SbSe_3 has been studied as a thermoelectric material with an ultralow thermal conductivity [16, 80-85]. In 2010, Skoug et al. first reported the thermal conductivity of polycrystalline Cu_3SbSe_3. The sample was prepared by melt processing, and showed a low thermal conductivity of 0.7 ~ 1.0 W m^{-1} K^{-1} at room temperature [80]. Later, Sevik et al. reported the theoretical thermoelectric properties of Cu_3SbSe_3, which were calculated using density-functional theory (DFT) and Boltzmann transport theory. A zT value of 0.7 at 600 K was predicted for p-type Cu_3SbSe_3 [81].

However, the high-temperature XRD analysis of Cu_3SbSe_3 revealed a reversible order/disorder phase transition around 175 ℃. As seen in Figure 2.29 (a), the lattice parameters exhibited nonlinear, but reversible and continuous, thermal expansion behavior around 175 ℃. The charge flipping analysis of HTXRD data indicated the Cu atoms become disordered at high temperature [86]. Also, a peak was observed around 175 ℃ in the heat capacity measurement (Figure 2.29 (b) inset), corresponding to the order/disorder transition. A minimum thermal conductivity of 0.3 $Wm^{-1}K^{-1}$ was obtained at the same temperature as the order/disorder transition occurred, suggesting an important structure–property relationship. But this transition could lead to micro-cracking of

materials when subjected to thermal cycling during use, which is a potential problem for applications.

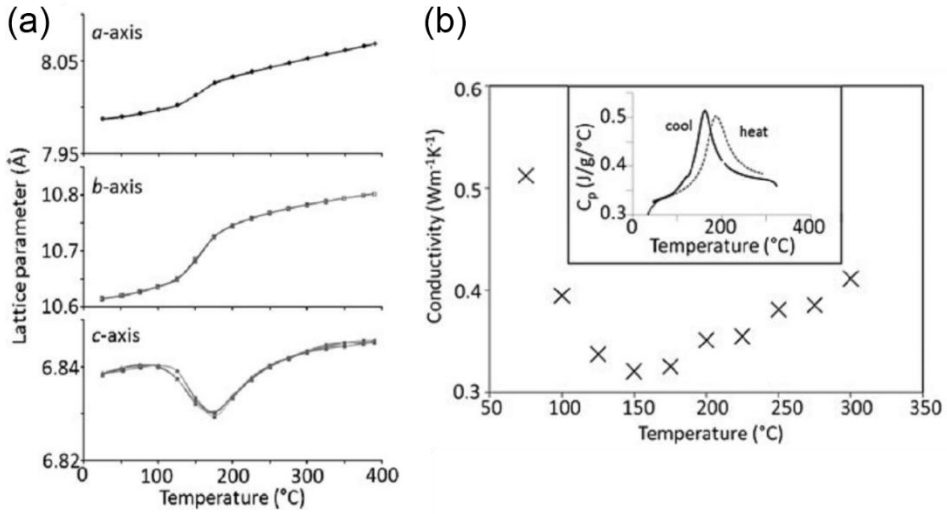

Figure 2.29: *The temperature dependence of (a) lattice parameters and (b) thermal conductivity and heat capacity for Cu_3SbSe_3 [86].*

In spite of the phase transition in Cu_3SbSe_3, a comprehensive study on the synthesis, characterization and evaluation of the thermoelectric properties of Cu_3SbSe_3 was reported. Figure 2.30 shows the temperature dependence of thermoelectric properties for Cu_3SbSe_3 from 300 K to 650 K [84]. Different methods have been used to prepare the samples. Sample Q-A-HP was prepared by melting, annealing and hot-pressing and sample MA-HP was prepared by ball-milling with hot-pressing. The annealed sample MA-HP was named as sample MA-HP-A. The measured Cp is consistent with other reports, indicating the phase transition is around 450 K. The effects of phase transition can be seen on the other thermoelectric properties as well. The resistivity and Seebeck coefficient decrease

with increasing temperature for all the samples, which is typical of the behavior of a non-degenerate semiconductor. The samples exhibit very high resistivity at 650 K, leading to a low power factor. This is because of the low hole concentration (~10^{16} cm^{-3}) and low hole mobility (10 ~ 20 $cm^2V^{-1}s^{-1}$) found in Cu_3SbSe_3. Attempts to increase the hole concentration by substituting with Ge for Sb or Te for Se failed. The ball-milled samples exhibited ultralow thermal conductivities less than 0.3 $Wm^{-1}K^{-1}$ at high temperature, which is believed to derive from its complex structure, the strong bond anharmonicity of Sb, the lone-pair electrons of Sb atoms and the disordered Cu atoms. A maximum *zT* value of 0.25 was obtained at 650 K in both Q-A-HP and MA-HP-A samples. Considering the phase transition and low *zT* value, Cu_3SbSe_3 does not have good potential as traditional thermoelectric material.

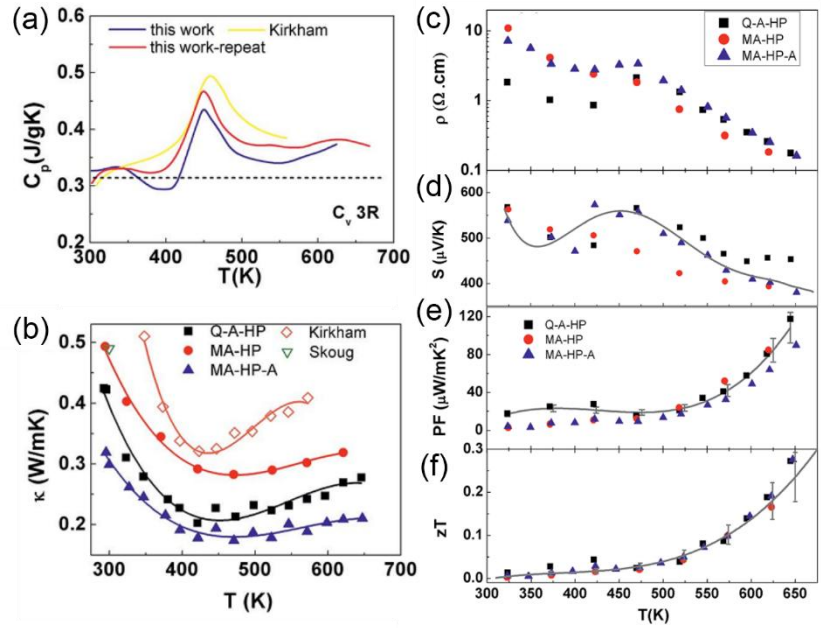

Figure 2.30: *The temperature dependence of (a) heat capacity, (b) thermal conductivity, (c) resistivity, (d) Seebeck coefficient, (e) power factor and (f) zT value for Cu_3SbSe_3[84].*

Based on the research of Cu_3SbSe_3, similar properties could be expected from Cu_3SbS_3. One similarity is that the phase transition was also found for Cu_3SbS_3. There are three known temperature-dependent crystal structures of Cu_3SbS_3 [87], which can be seen in Figure 2.31. Below 263 K, Cu_3SbS_3 has an orthorhombic structure (Figure 2.31 (a)) with space group $P2_12_12_1$ and lattice parameters of a = 7.884 Å, b =10.221 Å, and c = 6.624 Å [88]. The Sb atoms are coordinated to three S atoms forming a SbS3 pyramid with lone-pair electrons left while the Cu atoms are coordinated to three S atoms forming a distorted trigonal planar. Between 263 K and 395 K, the structure of Cu_3SbS_3 changes to a monoclinic structure (Figure 2.31 (b)) with space group $P2_1/c$ and lattice parameters of a = 7.808 Å, b = 10.233 Å, c = 13.268 Å and $\beta = 90.31°$ [89]. Compared with the low temperature structure, the atoms have the same coordination in this structure, but it has a small alternating distortion of the layers. Above 395 K, Cu_3SbS_3 has an orthorhombic structure (Figure 2.31 (c)) with space group *Pnma* and lattice parameters of a = 7.808 Å, b = 10.252 Å, and c = 6.587 Å [88]. The transition from room temperature phase to high temperature phase is similar with the order/disorder transition reported in Cu_3SbSe_3. The Cu atoms become disordered in the high temperature phase, which are distributed over five sites with trigonal plane or tetrahedral coordination.

Except the structural research of Cu_3SbS_3, there are very few reports about this compound, not to mention thermoelectric properties. Generally, the thermoelectric properties of sulfides are not as good as selenides. Since

Cu_3SbSe_3 is reported to be very poor in thermoelectricity, a good thermoelectric performance is not expected for Cu_3SbS_3. However, Cu_3SbS_3 could also have an ultralow thermal conductivity due to the lone-pair electrons of Sb atoms and the disordered Cu atoms, and it is still very helpful if the underlying physics and mechanisms can be well understood.

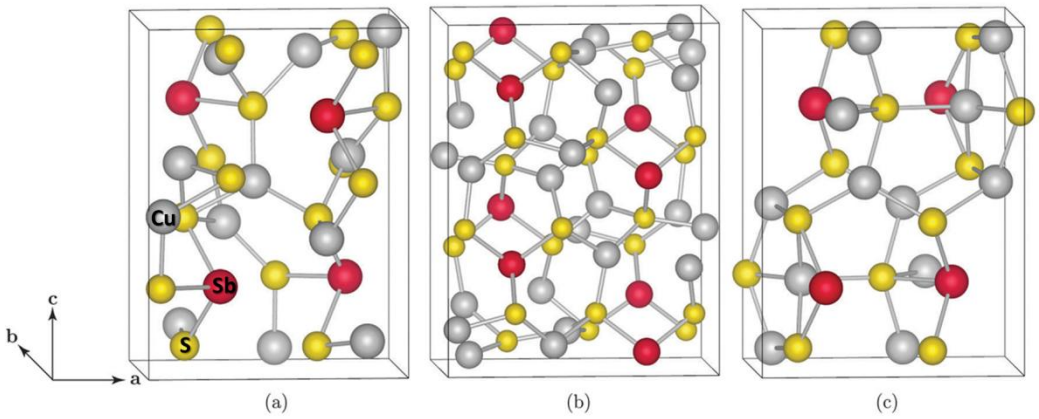

Figure 2.31: *The crystal structures of Cu_3SbS_3 at different temperature: (a) below 263 K, (b) between 263 K and 395 K, and (c) above 395 K [77].*

2.6.4 Cu_3SbS_4 (Famatinite)

The Cu_3SbS_4 compound, with mineral name of Famatinite, possesses a very simple crystal structure compared with the other three Cu-Sb-S ternary compounds. As shown in Figure 2.32 (a), Cu_3SbS_4 crystallizes into an ordered zinc-blende superstructure with the space group $I\bar{4}2m$ (no.121) and lattice parameters of a = b = 5.391(1) Å, c = 10.764(1) Å [90]. Both Cu atoms and Sb atoms are coordinated with four neighboring S atoms,

forming CuS4 and SbS4 tetrahedrons. Unlike the other three Cu-Sb-S ternary compounds, all the outer shell electrons of Sb atoms are involved in bonding and there are no lone-pair electrons in Cu_3SbS_4. As the lone-pair electrons play an important role in realizing intrinsically low thermal conductivity, the Cu_3SbS_4 compound could have a relatively high thermal conductivity. But a recent report indicates the structure of Cu_3SbS_4 is favorable for thermopower [91]. As the lattice parameters match $c \approx 2a$ ($c/2a = 0.998$), the structure of Cu_3SbS_4 can be considered as pesudocubic and it can realize cubic-like high degeneracy (such as PbTe [27] and Mg_2Si [92]) in its electronic bands, leading to a high thermopower. The calculated band structure of Cu_3SbS_4 can be seen in Figure 2.32 (b) [93]. The valence band maximum at the Γ point consists of three degenerate bands, which is consistent with the prediction based on its pesudocubic structure. Thus, Cu_3SbS_4 could be a potential p-type thermoelectric material.

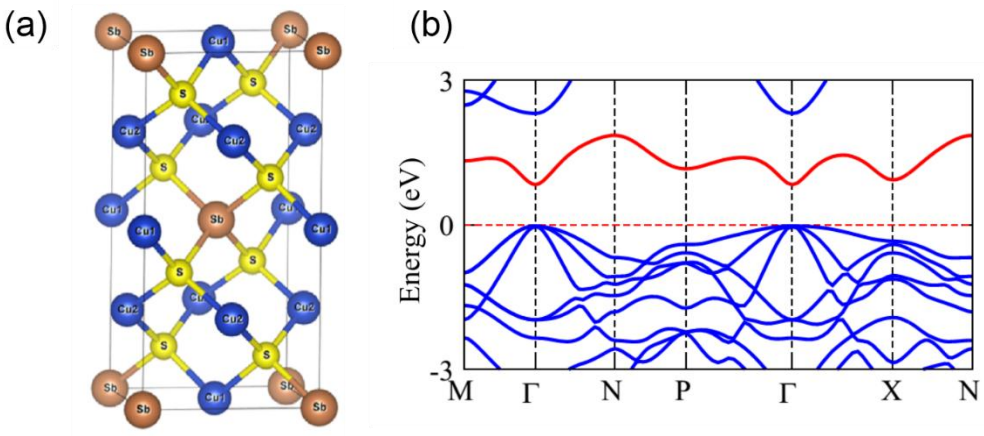

Figure 2.32: *(a) The crystal structure and (b) band structure of Cu_3SbS_4 [93].*

Moreover, as the isostructural analog of Cu_3SbS_4, Cu_3SbSe_4 has been reported as a good p-type thermoelectric material in recent years. It has the same structure as Cu_3SbS_4, with lager lattice parameters of a = b = 5.661 Å and c = 11.280 Å [94]. The first comprehensive study on the thermoelectric properties of Cu_3SbSe_4 was reported by Yang et al. in 2011 [94]. The polycrystalline Cu_3SbSe_4 samples were prepared by solid reaction combined with cold pressing and annealing, and the resultant bulk samples had relative densities of ~ 90 %. Sn was chosen as a dopant on the Sb site to optimize the electrical properties. The temperature dependence of thermoelectric properties can be seen in Figure 2.33.

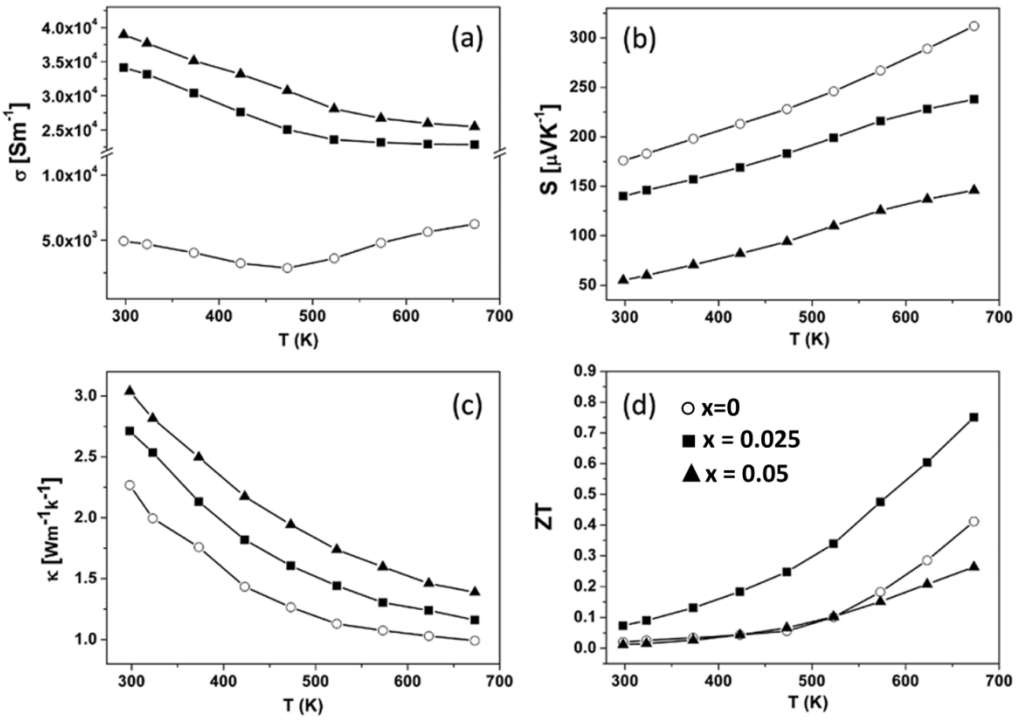

Figure 2.33: *The temperature dependence of (a) electrical conductivity, (b) Seebeck coefficient, (c) thermal conductivity, and (d) zT value for $Cu_3Sb_{1-x}Sn_xSe_4$ [94].*

The pristine Cu_3SbSe_4 sample has an electrical conductivity of 5000 Sm^{-1} at RT and shows a weak temperature dependence in the whole temperature range. With Sn doping, the carrier concentration was increased from 7.5×10^{18} cm^{-3} for Cu_3SbSe_4 to 7.8×10^{19} cm^{-3} for $Cu_3Sb_{0.95}Sn_{0.05}Se_4$, which led to a dramatic increase in electrical conductivity. The positive Seebeck coefficients indicate all the samples are p-type semiconductors. Due to the increased carrier concentration, the Seebeck coefficient dropped and thermal conductivity increased with increasing Sn doping. An optimized power factor was achieved in $Cu_3Sb_{0.975}Sn_{0.025}Se_4$ sample, leading to a maximum zT value of 0.75 at 673 K.

Other research groups reported the thermoelectric properties of Cu_3SbSe_4. Different synthetic methods and various dopants have been investigated [95-101]. A summary of the zT values from different reports is shown in Figure 2.34. Up to now, the best thermoelectric performance of Cu_3SbSe_4 was reported by Li et al, and a maximum zT value of 1.05 was obtained at 690 K [97]. In this report, the Cu_3SbSe_4 powder was prepared by chemical solution processing, and was in the form of flower-like nano-crystals. The hot-pressed bulk sample turns out to have very fine grain size, which is much smaller than that of the sample with same composition but prepared by MA + SPS method [99]. This fine microstructure led to a lower thermal conductivity and a higher zT value for Cu_3SbSe_4. Overall, all these researches indicate Cu_3SbSe_4 is promising for thermoelectric application for medium temperature.

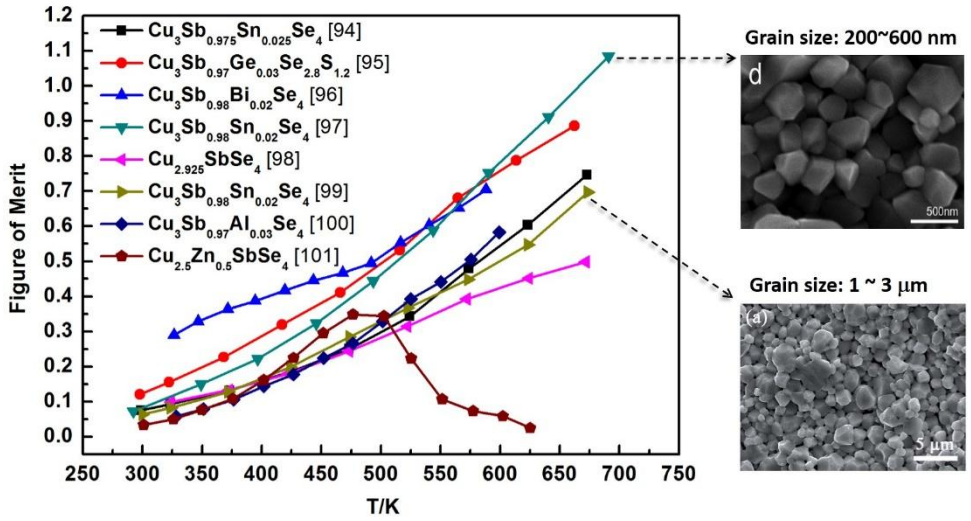

Figure 2.34: *The temperature dependence of zT values for Cu_3SbSe_4 from different reports (adapted from reference [94-101]).*

In spite of the good thermoelectric performance found for Cu_3SbSe_4, little research has been done on the thermoelectric properties of Cu_3SbS_4. In 1968, Katsumi reported the room temperature thermoelectric properties of Cu_3SbS_4 [102], showing it has an electrical conductivity of 3000 Sm^{-1}, a Seebeck coefficient of 151.8 μVK^{-1}, a thermal conductivity of 3.43 $Wm^{-1}K^{-1}$ and a very low *zT* value of 0.01 at 300K. Then there was no further research been reported, until Akitoshi et al. investigated the thermoelectric properties of Cu_3SbS_4 in 2014 [103]. The Cu_3SbS_4 powder was prepared by a two steps method. First, a Cu_3SbS_3 phase was prepared by direct fusion of pure elements in vacuum quartz ampoule at 1173 K for 12 h. Then the sample was mixed with S powder and heated in vacuum quartz ampoule at 673 K for 12h. After that the powder was sintered by SPS, and a single phase bulk sample was obtained. The backscattered electron image of Cu_3SbS_4

bulk sample (Figure 2.35) shows a uniform phase with porosity (black part). And the grain size of the sample is about 5 ~ 10 μm.

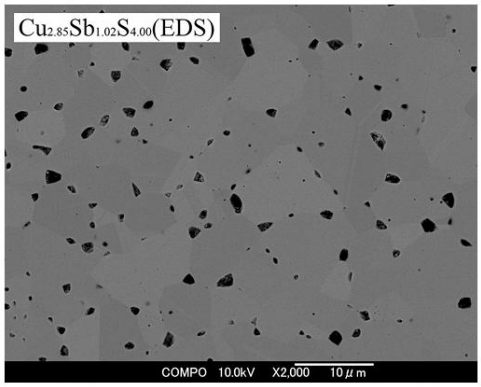

Figure 2.35: *The backscattered electron image of Cu_3SbS_4 bulk sample [103].*

The Ge was chosen as a dopant on Sb site to adjust the electrical properties of Cu_3SbS_4, The thermoelectric properties of $Cu_3Sb_{1-x}Ge_xS_4$ (x=0, 0.02, 0.04, 0.06, 0.08 and 1.0) samples were studied, which are shown in Figure 2.36. The undoped Cu_3SbS_4 shows very low electrical conductivity (15 S/cm), but a high Seebeck coefficient (500 μV/K) which is much higher than the value reported by Katsumi [102]. With increasing Ge-doping, the electrical conductivity increased significantly while the Seebeck coefficient dropped. The low-temperature Hall measurements indicate that undoped Cu_3SbS_4 has a semiconducting behavior as the hole concentration increased with temperature. With Ge-doping, the hole concentration increased significantly, which is in agreement with the electrical conductivity and Seebeck coefficient results. A maximum power factor of 16 $\mu Wcm^{-1}K^{-}$

^{2} was achieved in x = 0.08 sample at 573 K and this value is comparable with that reported in Cu_3SbSe_4. However, the thermal conductivities were only measured at room temperature in this report. The calculated *zT* values were below 0.1 at 323 K for all the samples, but a better performance could be achieved at high temperature.

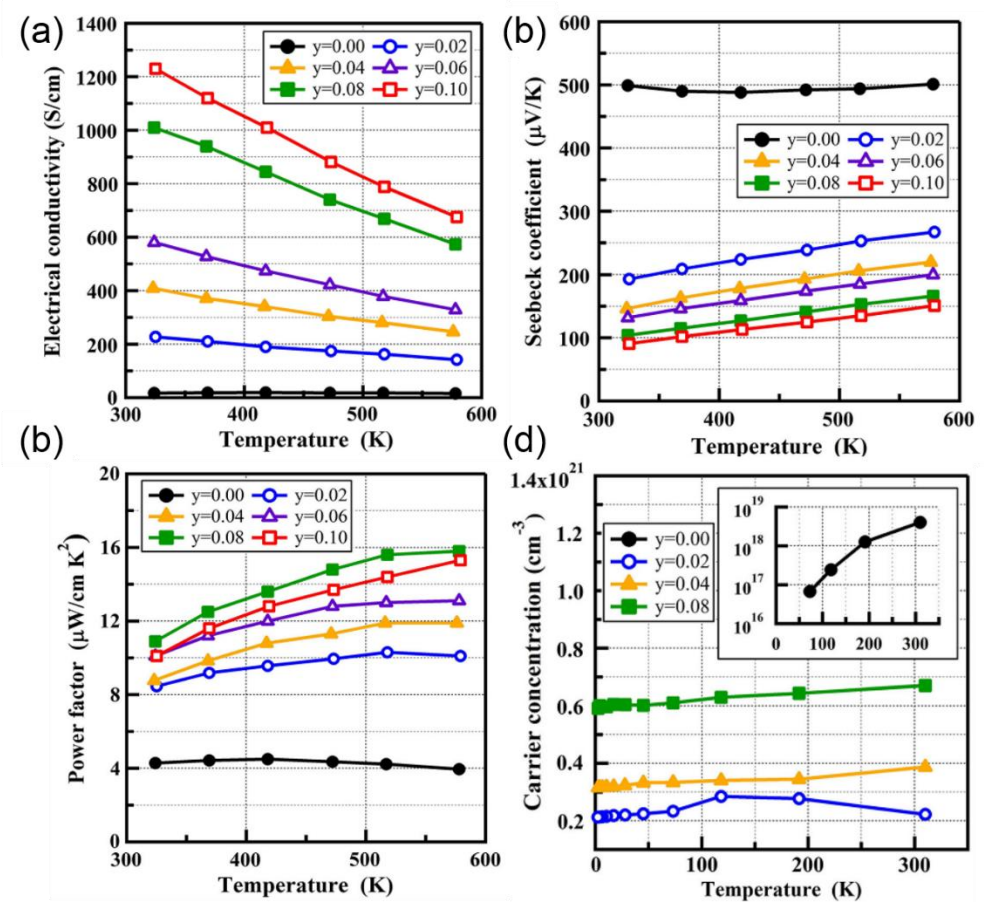

Figure 2.36: *The temperature dependence of (a) electrical conductivity, (b) Seebeck coefficient, (c) power factor, and (d) carrier concentration for* $Cu_3Sb_{1-x}Ge_xS_4$ *[103].*

2.6.5 Conclusions

The high earth-abundance, low toxicity and good thermoelectric performance of tetrahedrite ($Cu_{12}Sb_4S_{13}$) motivated the idea of exploring new thermoelectric Cu-Sb-S ternary compounds. Three other compounds of $CuSbS_2$, Cu_3SbS_3 and Cu_3SbS_4 were found in this family, but there is very limited research on them. Some structural and fundamental information on these compounds were learnt from literatures, which suggests that it is possible to find interesting thermoelectric properties for these compounds. Also, it is interesting to investigate the effects of lone-pair electrons on the properties of thermoelectric compounds. Therefore, it is worth having a systematic and comprehensive study on the synthesis, crystal structures and thermoelectric properties of Cu-Sb-S ternary compounds.

Chapter 3 Experimental Details

3.1 Sample Preparations

3.1.1 Mechanical Alloying

The powders of the Cu-Sb-S compounds were prepared by mechanical alloying (MA) in a planetary ball-milling machine (QM-3SP4, Nanjing University Instrument Plant, China) as shown in Figure 3.1(a). The stoichiometric elements of Cu (99.5 %, AlfaAesar), Sb (99.5 %, AlfaAesar) and S (reagent grade, purified by sublimation, Sigma-Aldrich) were loaded into stainless milling jars with stainless balls. The weight of power loaded in one jar is 15g and the weight ratio of powder to ball is 1:20. To avoid oxidation, the powder was handled in glove box (Figure 3.1 (b)) with argon atmosphere and the milling jars were sealed with argon inside. Then the powder was milled for 20 h at a speed of 420 rpm based on experience and different trials. After milling, the obtained powder was hand ground in an agate mortar as the powder was a bit aggregated.

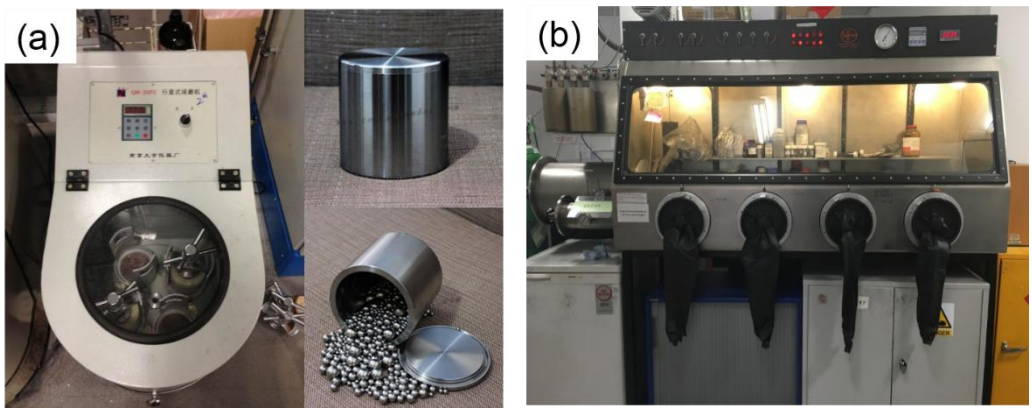

Figure 3.1: *(a) QM-3SP4 planetary ball-milling machine; (b) Saffron scientific glove box.*

3.1.2 Melt Processing

Some powders of Cu-Sb-S compounds were prepared by conventional melt processing in order to compare with the sample prepared by MA. The stoichiometric elements of Cu (99.5 %, AlfaAesar), Sb (99.5 %, AlfaAesar) and S (reagent grade, purified by sublimation, Sigma-Aldrich) were hand mixed in an agate mortar and then cold pressed in a 13 mm die with 1 ton force for 5 min. The cold pressed pellet was placed in a quartz ampoule (Figure 3.2 (a)), which was evacuated to 10^{-6} Torr and then sealed. After sealing, the ampoule was placed vertically in a box furnace (Figure 3.2 (b)). The furnace was slowly heated to 900 ℃ and kept at this temperature for 12 h. Then the furnace was cooled to 450 ℃ at a rate of 5 ℃/min and the sample was annealed at this temperature for 48 h. The obtained ingot was ground into powder in an agate mortar.

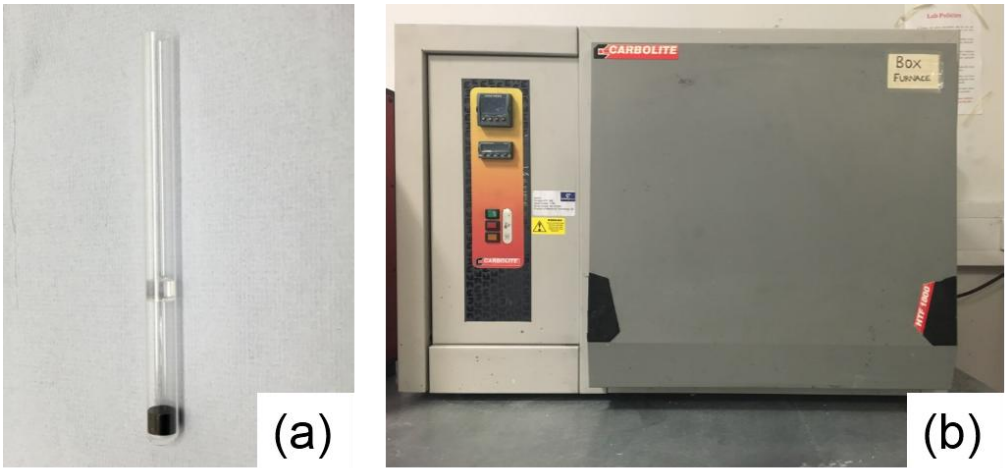

Figure 3.2: *(a) Quartz ampoule sealed in vacuum; (b) Box furnace (Carbolite HTF 1800).*

3.1.3 Spark Plasma Sintering (SPS)

Spark plasma sintering (SPS) is a low voltage (typically below 10V), pulsed direct current (typically from 1 to 10 kA) activated, pressure-assisted and fast synthesis technique [104]. Figure 3.3 shows the spark plasma sintering furnace (FCT, Germany) used in this work and its working schematic. The powder sample is placed in the conductive graphite die and a uniaxial pressure was applied to the powder through graphite punches. A high electric current will go through the die, punches and samples (conductive sample), which can achieve a high heating rate and the sintering can finish in several minutes. This fast sintering technique is widely used in thermoelectric materials to obtain fine microstructures. The powder obtained from mechanical alloying and melt processing was sintered using SPS. The $Cu_{12}Sb_4S_{13}$, $CuSbS_2$, Cu_3SbS_3 and Cu_3SbS_4 samples were sintered for 3 min at 350 ℃, 350 ℃, 400 ℃ and 450 ℃ respectively, under a pressure of 60 MPa. The sintering conditions used for different samples have been optimized to get dense samples. The vacuum level inside the furnace was below 10 Pa during sintering.

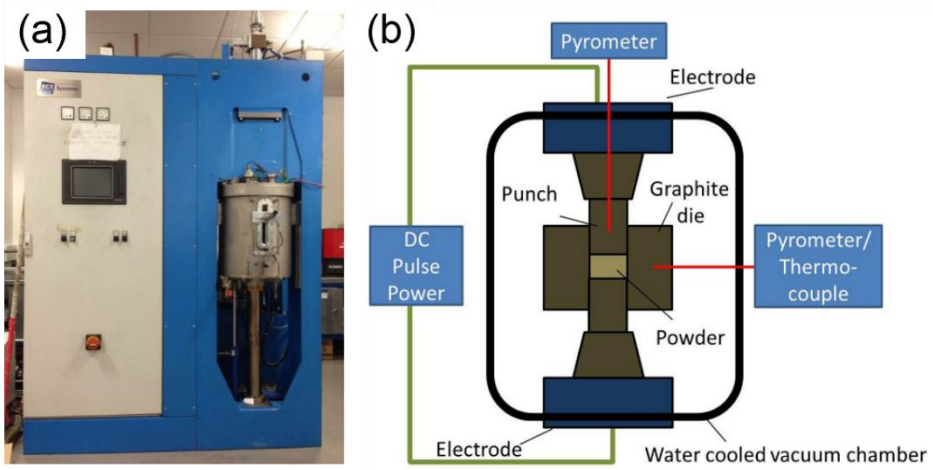

Figure 3.3: *(a) Spark plasma sintering furnace (FCT, Germany); (b) working schematic [104].*

3.2 Characterizations

3.2.1 Density Measurements

The densities of all the bulk samples were measured using Archimedes method. For nearly fully dense sample or the sample containing closed porosity, the density can be calculated by the following equation:

$$\rho = \frac{m_1 \rho_w}{m_1 - m_2}$$

Where m_1 is the mass of the sample in air, m_2 is the mass of the sample immersed in water, ρ_w is the density of water and ρ is the density of the sample. To minimize the error, every sample was measured three times and a mean value was used as the density of a sample. The advantage of Archimedes method is that it is capable of any shape of sample, but it is worth noting that this method is no suitable for a porous sample with open pores, as the water will fill in the pores and the density will be overestimated.

3.2.2 X-Ray Diffraction and X-Ray Photoelectron Spectroscopy

X-ray diffraction (XRD) is a non-destructive analytical technique based on Bragg's law, which can be used for phase, crystal structure and composition analysis of a material. In this work, the XRD data for phase identification of powder was collected on a X-ray diffractometer (Siemens D5000) using Cu Kα radiation over 2θ range 8 °to 70 °in steps

of 0.03 ° with a count rate of 10 s per step. The obtained XRD data was analysed using X'Pert HighScore software. The phases were identified by matching the data of samples with data from a standard XRD database. For mixed phases, the detection limit is ~ 2% of a sample.

X-Ray photoelectron spectroscopy (XPS) is a surface-sensitive quantitative spectroscopic technique that provides the information of elemental composition, chemical state and electronic state of the elements within the top 1-12 nm of the sample surface. The XPS data was collected on an ESCALAB 250 X-ray Photoelectron Spectrometer (Thermo Corp.) with monochromatized Al Kα (1486.5 eV) X-ray source and a pass energy of 20 eV. Carbon was used as a reference material for calibration.

3.2.3 Scanning Electron Microscopy

The microstructures of bulk samples were observed using a scanning electron microscope (SEM) (FEI, Inspect F), which uses a focused electrons beam to scan the samples and collects information from the interactions between electrons and atoms. The images of fracture surfaces of bulk samples were obtained using a secondary electrons detector. The elemental mapping of the microstructures were obtained on polished surfaces (final polishing with 1μm diamond suspension) of bulk samples using energy dispersive X-ray spectrometry (EDS) in SEM.

3.2.4 Electrical Characterizations

The electrical resistivity and Seebeck coefficients of the samples were measured simultaneously from room temperature to 623 K on a ZEM-3 (ULVAC-RIKO, Japan) at the University of Manchester. The samples were cut into bars with dimensions of 3×3×15 mm for the measurements. The schematic of measurements is showing in Figure 3.4.

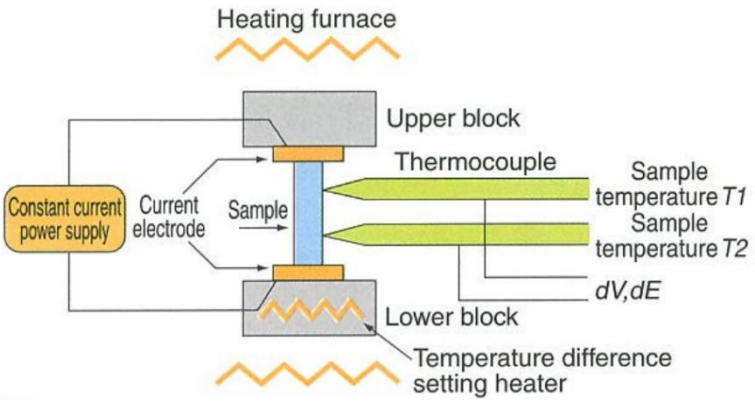

Figure 3.4: *Schematic of electrical resistivity and Seebeck coefficient measurements.*

The bar sample was set in a vertical position between the upper and lower blocks in the furnace. The sample is heated to and held at a specified temperature under flowing argon. Electrical resistivity (ρ) was measured using the dc four-terminal method, in which a constant current (I) is applied to the sample and the voltage drop (V) between the thermocouples is measured with subtraction of the thermo-electromotive force between leads. The electrical resistivity is calculated by the following equation:

$$\rho = \frac{V}{I}\frac{A}{d}$$

Where *A* is the area of cross section of the sample and *d* is the distance between the thermocouples. In order to measure the Seebeck coefficient (α), the sample is heated by the heater in the lower block to create a temperature gradient. The upper and lower temperatures (*T1* and *T2*) and the thermal electromotive force (ΔE) between the thermocouples are measured. The Seebeck coefficient is obtained by a static DC method based on the slope of ΔE versus temperature-difference (*T2*-*T1*) curve. Note that there is a 5% uncertainty in all the results.

The room temperature carrier concentrations of the samples were measured using the Van der Pauw method, on a Hall measurement system (Lake Shore 8400 Series) at Imperial College. The samples were cut and polished into a thin square pellet with dimensions of 10×10×0.5 mm for the measurements. The principles of measurement can be seen in Figure 3.5. With different combinations of the directions of current (*I*) and magnetic field (*B*), eight Hall voltages were measured. The carrier concentration (*n*) was calculated from the mean value of Hall voltages ($\bar{V}_{\mathrm{H}}$) by the following equation:

$$n = \frac{IB}{qd\bar{V}_{\mathrm{H}}}$$

Where *q* is the elementary charge and *d* is the thickness of the sample. Due to the relatively low magnetic field (1.5 T) in this system, the uncertainty of the result increases up to 20% with increasing carrier concentration (above 10^{20} cm^{-3}).

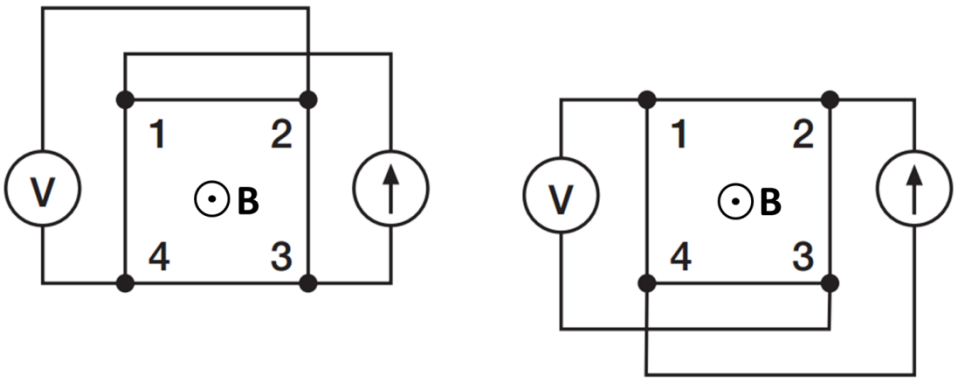

Figure 3.5: *Principles of Hall measurements.*

3.2.5 Thermal Characterizations

The thermal conductivities (κ) of the samples were calculated using the following equation:

$$\kappa = \rho C_P D$$

Where ρ is density, C_P is the specific heat capacity and D is the thermal diffusivity. The specific heat capacity was calculated using the Dulong-Petit law, which gives very good estimation at room temperature based on the results in compounds of $Cu_{12}Sb_4S_{13}$, Cu_3AsS_4 and Cu_3SbSe_4 [15, 105]. According to the reported results in $Cu_{12}Sb_4S_{13}$, the difference between calculated results and measured results is within 8 % up to 700 K [15]. Thermal diffusivity was measured on a laser flash system (Netszch LFA 457) and the schematic of measurements are shown in Figure 3.6. The sample for the measurement was a round pellet with 20 mm diameter and a uniform thickness of about 2.5 mm. The Graphite 33 spray (Kontakt-Chemie) was used to coat both surfaces of the sample to minimise laser reflection. The sample was heated to and held at a specified temperature

in N_2 flow. When the temperature was stable, the lower surface of the sample was first heated by a short energy pulse (Figure 3.6 (a)). The resulting temperature change on the upper surface of the sample was then measured with an infrared detector. The typical result of the signals is presented in Figure 3.6 (b). The steeper the signal increasing indicates the higher the sample's thermal diffusivity. Using the half time ($t_{1/2}$, time value at half signal height) and sample thickness (d), the thermal diffusivity (D) can be calculated by the equation of $D = 0.1388\frac{d^2}{t_{1/2}}$. To minimize the error, the equipment was calibrated with the standard samples and the sample was measured three times at every specified temperature. There is a 1% uncertainty in thermal diffusivity results.

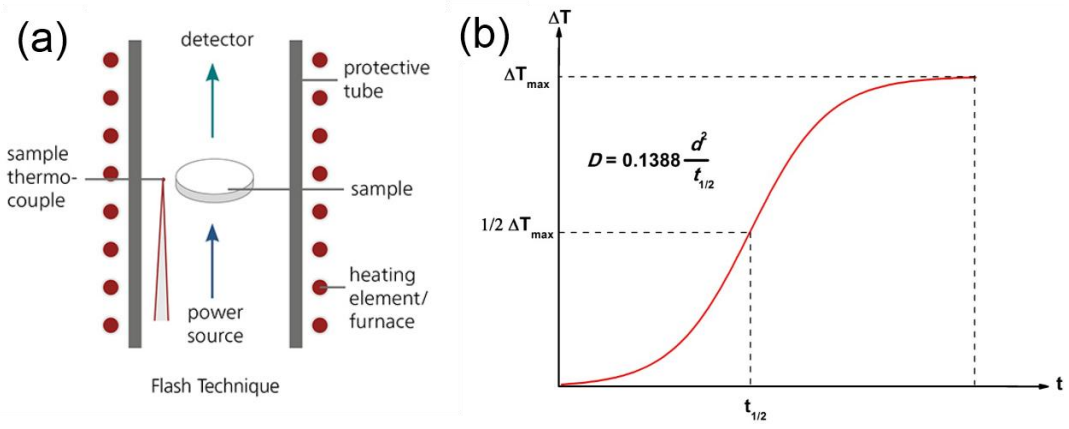

Figure 3.6: *Schematic of thermal diffusivity measurements.*

Chapter 4 Initial Investigation of Cu-Sb-S Compounds

4.1 Introduction

The thermoelectric properties of tetrahedrite ($Cu_{12}Sb_4S_{13}$) have been intensively studied in recent years, because of its advantages of low-cost, low-toxicity and intrinsically low thermal conductivity. However, there is very little research on the other three compounds of the Cu-Sb-S system. In order to explore the potential thermoelectric properties in the Cu_3SbS_3, $CuSbS_2$ and Cu_3SbS_4 compounds, the synthesis methods, phase structures, microstructures, electrical properties and thermal properties of all four compounds ($Cu_{12}Sb_4S_{13}$, Cu_3SbS_3, $CuSbS_2$ and Cu_3SbS_4) were investigated. In most reports, the Cu-Sb-S powders were prepared by traditional melt processing in sealed tube. In this work, mechanical alloying was employed to prepare Cu-Sb-S powders, which is easy, efficient and applicable in large-scale synthesis. Some Cu_3SbS_4 powder was prepared by melt processing, in order to compare the impacts of these two methods on samples' microstructures and properties. Dense bulk samples were obtained using spark plasma sintering (SPS). Due to their different stoichiometry and crystal structures, the four compounds showed different electrical and thermal behaviour. The lone-pair electrons of Sb has significant influence on the thermal conductivities of these compounds.

4.2 Experimental Details

Cu_3SbS_4 powder was prepared by both melt processing and mechanical alloying method. For melt processing, the stoichiometric amount (15 g) of the elements of Cu (99.5 %, AlfaAesar), Sb (99.5 %, AlfaAesar) and S (reagent grade, purified by sublimation, Sigma-Aldrich) were hand mixed in an agate mortar and then cold pressed into pellets. The pellets were sealed in an evacuated quartz tube and held at 1173 K for 12h. Then the sample was annealed at 723 K for 48h to obtain good homogeneity. The obtained ingot was hand ground into powder in an agate mortar for SPS. For mechanical alloying method, the same stoichiometric amount of the elements (15 g) were loaded in stainless jars with a powder to ball weight ratio of 1:20 and then sealed with argon. Then they were ball milled at a speed of 420 rpm for 20 h. The $Cu_{12}Sb_4S_{13}$, Cu_3SbS_3 and $CuSbS_2$ powders were prepared by mechanical alloying using the same conditions. The bulk samples of $Cu_{12}Sb_4S_{13}$, Cu_3SbS_3, $CuSbS_2$ and Cu_3SbS_4 were prepared by SPS at 623 K, 623 K, 673 K and 723 K respectively, under a pressure of 60 MPa. The sintering conditions for the four compounds were determined by systematic sintering studies.

4.3 Results and Discussions

4.3.1 Comparative Study of Synthesis Methods

The Cu_3SbS_4 samples prepared using melt processing and mechanical alloying (MA) (before and after SPS) were examined using XRD. Figure 4.1 (a) shows the XRD results of the Cu_3SbS_4 powder prepared by melt processing and bulk sample after SPS. There

was no difference between the XRD results before and after SPS. The main phase was confirmed as Cu_3SbS_4 (PDF: 00-035-0581), but a second phase of $Cu_{12}Sb_4S_{13}$ was detected. The formation of the second phase was caused by sulfur loss during melt processing. As sulfur has a low boiling point (444.7 ℃) and a high vapor pressure, some of the sulfur existed as vapor in the sealed tube at high temperature and did not take part in chemical reaction. For this reason, a second phase of $Cu_{12}Sb_4S_{13}$, which contains less sulfur than Cu_3SbS_4, was formed. A phase pure Cu_3SbS_4 sample might be obtained by adding excess sulfur, but it was difficult to determine the exact amount of sulfur required. Besides, the excess sulfur might cause an explosion of the quartz tube. By contrast, the mechanical alloying method was more suitable for sulfur containing compounds, in which a chemical reaction and phase formation took place near room temperature assisted by mechanical energy [106]. As shown in Figure 4.1 (b), the Cu_3SbS_4 powder prepared by mechanical alloying was phase pure. The broad XRD peaks suggested that the powder had small particle size. After SPS the bulk sample had very sharp XRD peaks, indicating that it was well crystallized.

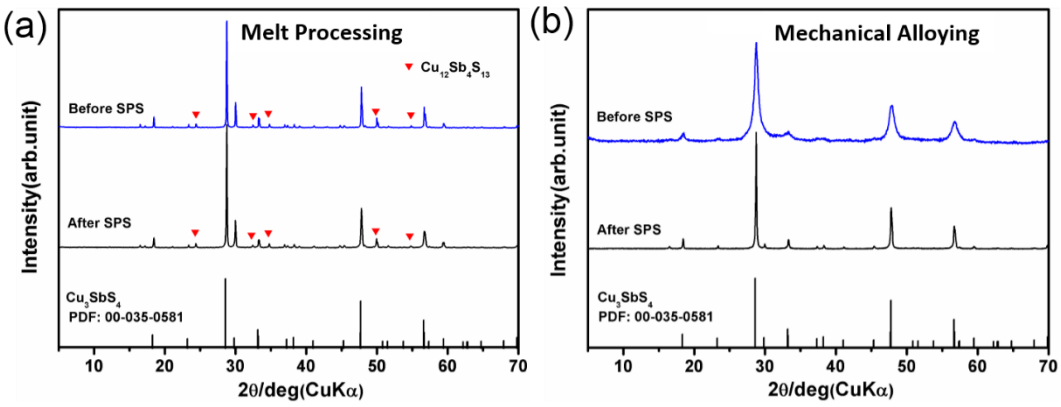

Figure 4.1: *XRD patterns of Cu_3SbS_4 samples prepared by (a) melt processing and (b) mechanical alloying method.*

Figure 4.2 shows SEM images of fracture surfaces of the bulk samples prepared using melt + SPS and MA + SPS. The sample prepared by melt + SPS showed some pores and had very large grains (> 20 μm), which is similar to the sample reported by Suzumura et al. [103]. The growth of grains was caused by the long-time heat treatment needed in the melt processing. In contrast, the sample prepared by MA + SPS showed very uniform microstructure with much smaller grains of 100 ~ 300 nm. The small grain size of bulk sample benefited from the mechanical alloying and the fast sintering technique (SPS).

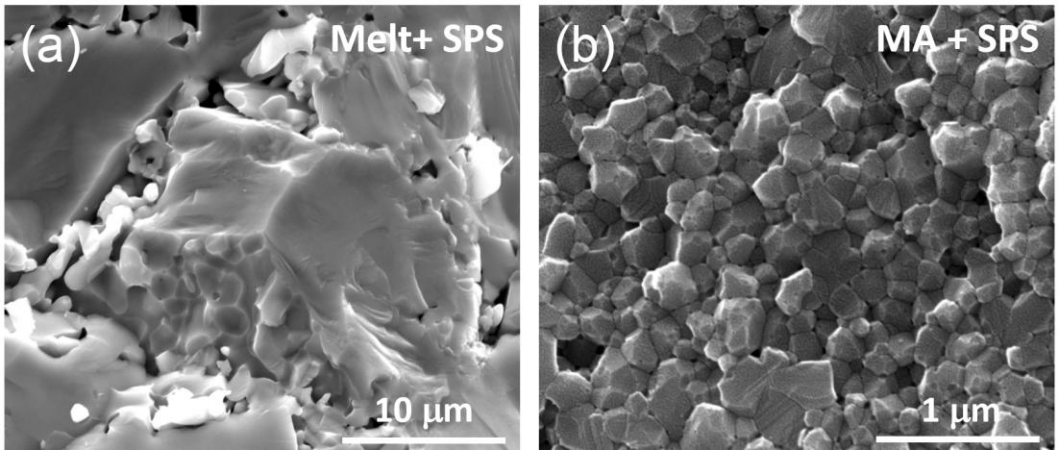

Figure 4.2: *SEM images of Cu_3SbS_4 samples prepared by (a) melting + SPS and (b) MA+SPS.*

Figure 4.3 shows SEM images of powder after ball milling. As the powder was dry-milled, it turned out to be aggregated. Some small particles with size of 100 nm were observed. Also, the particle size and grain size were estimated from XRD results based on the Scherrer equation,

$$D = \frac{0.94\lambda}{\beta \cos\theta}$$

Where D is the mean size of particle or grain, λ is the X-ray wavelength, β is the line broadening at half of the maximum intensity (FWHM) and θ is the Bragg angle. As shown in Figure 4.4, the main peak at 28.75 °(2θ) was chosen for the calculations. The calculated particle size of the powder was about 17 nm, while the calculated grain size of the bulk sample was about 124 nm. The calculated grain size is consistent with the average grain size observed in SEM images of bulk samples. The calculated particle size of powder was very small, but it was not able to observe from SEM images. This is probably because of the aggregation of powder, and it was difficult to confirm the particle size of powder from SEM. During a fast sintering using SPS, the grain growth was minimized leading to a very fine microstructure in dense bulk sample. Besides, the bulk sample prepared by MA + SPS method was polished for back scattering analysis as shown in Figure 4.5. The results suggested the sample was homogeneous.

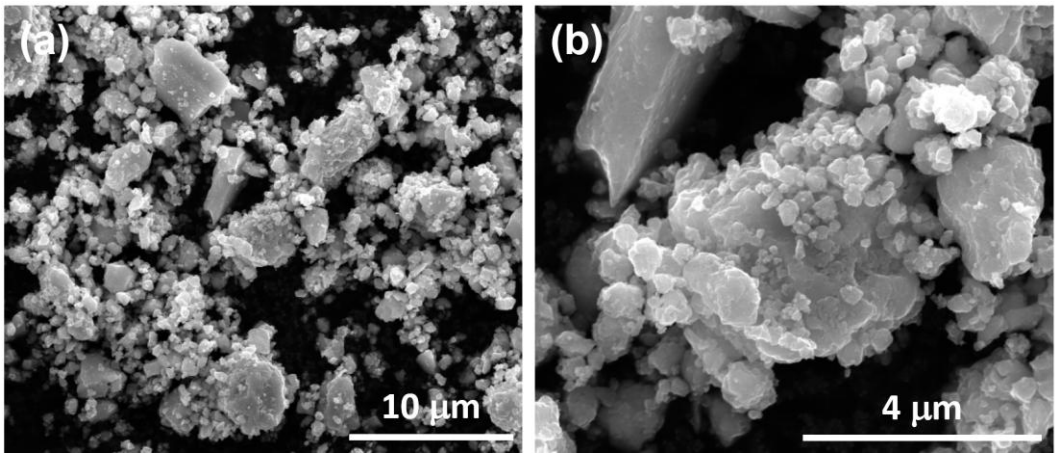

Figure 4.3: *SEM images of Cu_3SbS_4 powder after ball milling.*

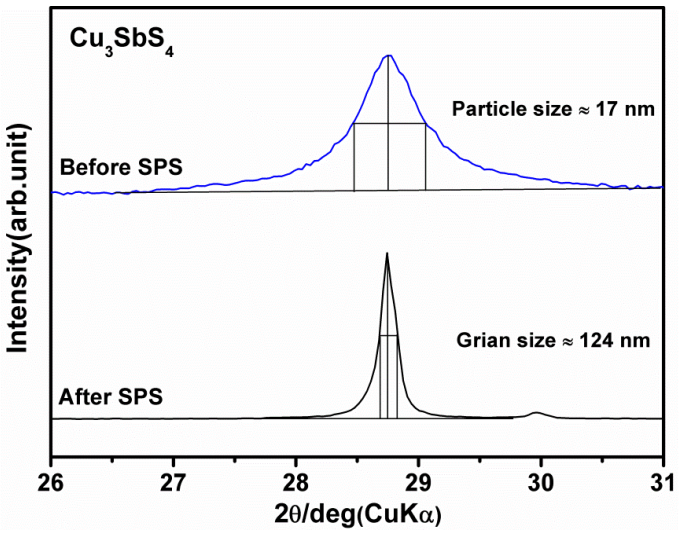

Figure 4.4: *XRD peak for particle and grain size calculations.*

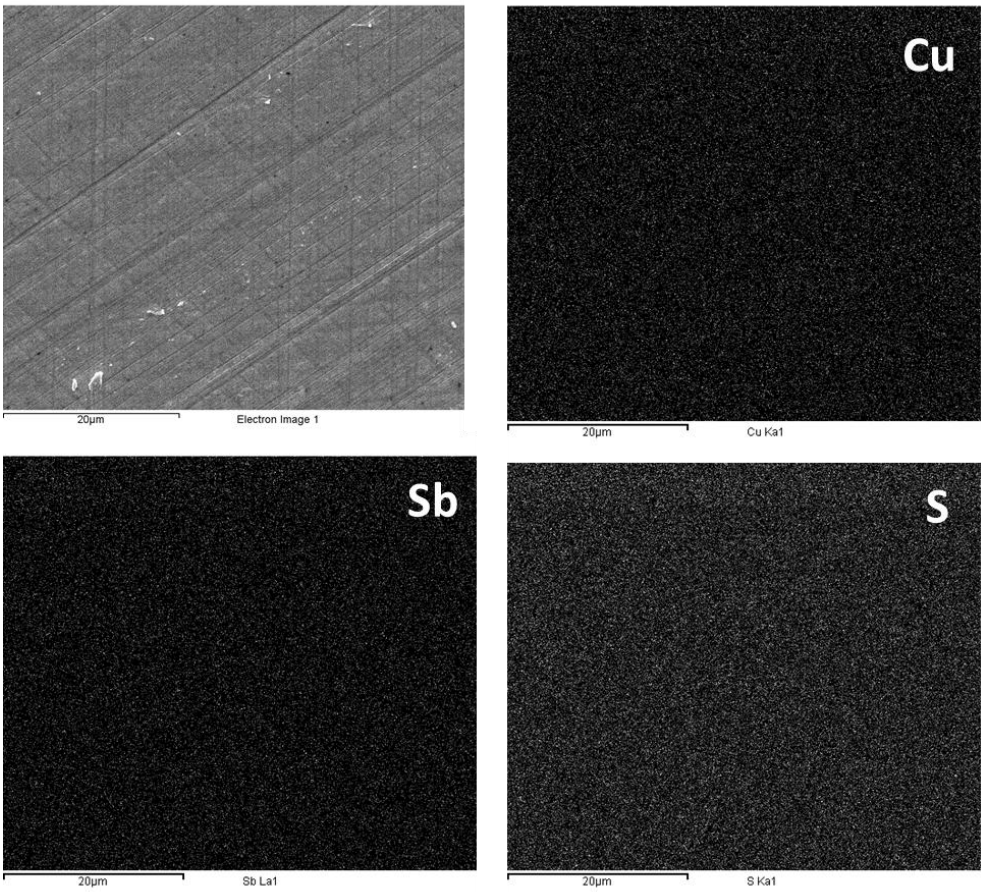

Figure 4.5: *Back scattered image and EDX mapping of Cu_3SbS_4 sample prepared by MA+SPS.*

Figure 4.6 shows the temperature dependence of thermal conductivities for samples prepared using the different processing methods. For both samples, the thermal conductivities decreased with increasing temperature and there was no sign of bipolar effects up to 673 K. The thermal conductivity of the sample prepared by melt + SPS was higher than that of the sample prepared by MA + SPS, which was expected from the difference in their microstructures. The lowest thermal conductivity of 0.63 $Wm^{-1}K^{-1}$ was achieved at 673 K, which was comparable with the lowest thermal conductivity (0.5 $Wm^{-1}K^{-1}$) reported for Cu_3SbSe_4 [97].

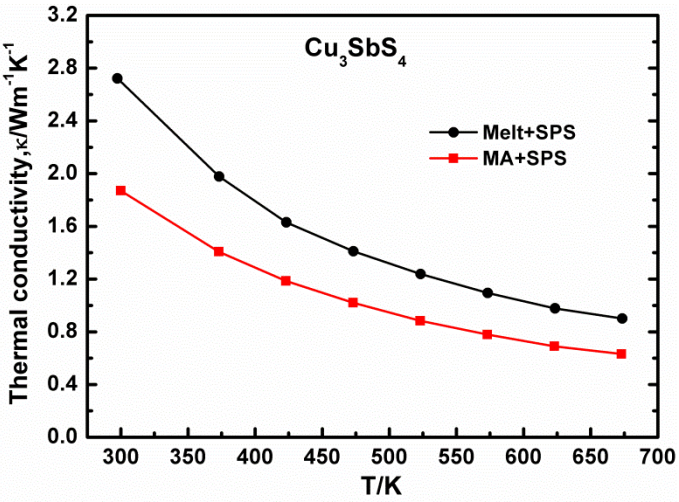

Figure 4.6: *The temperature dependence of thermal conductivities for Cu_3SbS_4 samples prepared by melting + SPS and MA + SPS. Note there is a 10 % uncertainty in all data points.*

Overall, the combination of mechanical alloying and SPS was an easy and effective method to prepare phase pure Cu_3SbS_4 sample with fine microstructures. Thus this synthesis method was used to prepare the other compounds investigated in this work.

4.3.2 Comparative Study of Undoped Cu-Sb-S Compounds

The $Cu_{12}Sb_4S_{13}$, Cu_3SbS_3, $CuSbS_2$ and Cu_3SbS_4 samples before and after SPS were examined using XRD, and the results are shown in Figure 4.7. For all four compounds, the XRD peaks of samples before SPS were broader than those of the samples after SPS due to the small particle size of the powders produced by mechanical alloying. For $Cu_{12}Sb_4S_{13}$ ceramics, a small amount of second phase Cu_3SbS_4 was found before and after SPS. As seen in Figure 4.7 (a), the intensity of the second phase peaks (marked by red triangles) was much smaller than those of $Cu_{12}Sb_4S_{13}$. It seems that the second phase of Cu_3SbS_4 was easily formed in $Cu_{12}Sb_4S_{13}$ as it was also found in other reports, in which the powders were prepared by melt processing [56, 59, 61, 62].

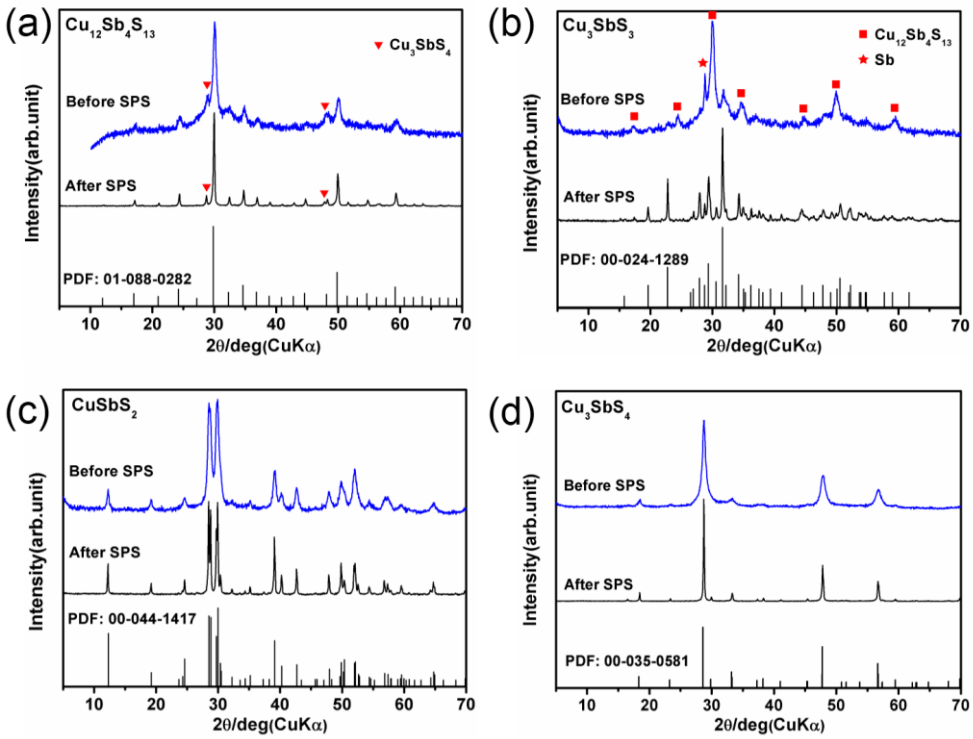

Figure 4.7: *XRD patterns of (a) $Cu_{12}Sb_4S_{13}$, (b) Cu_3SbS_3, (c) $CuSbS_2$, and (d) Cu_3SbS_4 samples before and after SPS.*

In the case of Cu_3SbS_3, it was very different from the other three compounds. As shown in Figure 4.7 (b), the sample before SPS was a mixture of $Cu_{12}Sb_4S_{13}$, Sb and Cu_3SbS_3. The target phase Cu_3SbS_3 was not completely formed during mechanical alloying. However, a phase pure Cu_3SbS_3 sample was obtained after SPS, which indicated that the single phase formation was assisted by the heat and pressure during SPS sintering. For the $CuSbS_2$ and Cu_3SbS_4 samples, all the peaks could be indexed to standard XRD data and there was no second phase observed before and after SPS, which can be seen in Figure 4.7 (c) and 4.7 (d). The theoretical, measured and relative densities of bulk samples for all four compounds are shown in Table 4.1. All the samples had a relative density around 98 %.

Sample Name	**Theoretical Density (g/cc)**	**Measured Density (g/cc)**	**Relative Density (%)**
$Cu_{12}Sb_4S_{13}$	5.07	4.99	98.4
Cu_3SbS_3	5.14	5.01	97.4
$CuSbS_2$	5.01	4.93	98.4
Cu_3SbS_4	4.69	4.60	98.1

Table 4.1: *The theoretical, measured and relative densities of $Cu_{12}Sb_4S_{13}$, Cu_3SbS_3, $CuSbS_2$ and Cu_3SbS_4 bulk samples.*

The microstructures of $Cu_{12}Sb_4S_{13}$, Cu_3SbS_3, $CuSbS_2$ and Cu_3SbS_4 samples were observed using SEM. The fracture surfaces of all four samples are shown in Figure 4.8. The samples had different morphologies. Except for Cu_3SbS_3, the other three samples had fine and uniform microstructures. The Cu_3SbS_3 sample had relatively large grains and some pores were observed at the grain boundaries. The pores were produced by the chemical reactions and phase formation during SPS sintering, as the Cu_3SbS_3 powder was not phase pure before SPS.

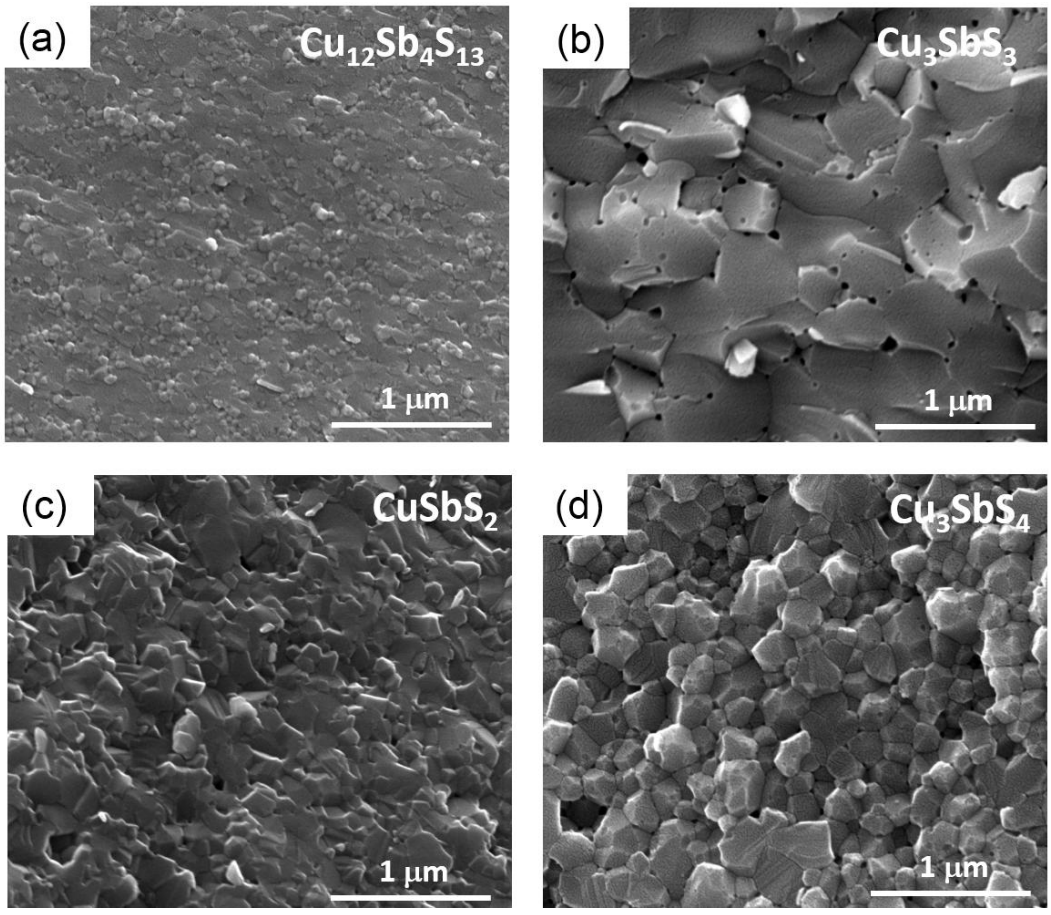

Figure 4.8: *The fracture surface SEM images of (a) $Cu_{12}Sb_4S_{13}$, (b) Cu_3SbS_3, (c) $CuSbS_2$, and (d) Cu_3SbS_4 bulk samples.*

The thermoelectric properties of undoped $Cu_{12}Sb_4S_{13}$, Cu_3SbS_3, $CuSbS_2$ and Cu_3SbS_4 samples were characterized from 300 K to 623 K. The temperature dependence of the electrical resistivities, Seebeck coefficients and power factors for all four samples are shown in Figure 4.9. The electrical resistivities of all four samples decreased with increasing temperature, indicating semiconducting behavior. As $Cu_{12}Sb_4S_{13}$ possesses an electron-deficient structure and intrinsically high carrier concentration (3.6×10^{21} cm^{-3}) [64, 107], the $Cu_{12}Sb_4S_{13}$ sample exhibited a low electrical resistivity, which was about 50 to 20 μΩm from 300 K to 623 K. By contrast, the other three samples had very high electrical resistivities (10^3~10^6 μΩm), due to their intrinsically low carrier concentrations (10^{13}~10^{18} cm^{-3}) [84, 103, 108].

The Seebeck coefficients of all the samples were positive, which implied they were all p-type semiconductors. Based on the Mott equation [109], the Seebeck coefficient (α) can be written as,

$$\alpha = \frac{8\pi^2 k_B^2}{3eh^2} m^* T \left(\frac{\pi}{3n}\right)^{2/3}$$

Where k_B is the Boltzmann constant, h is the Planck constant, e is the elementary charge, m^* is the effective mass, n is the carrier concentration and T is the temperature. It indicates that the Seebeck coefficient is directly proportional to the effective mass m^* and inversely proportional to the carrier concentration n. This can be used to explain the differences in the Seebeck coefficients for the four different compounds. As undoped $CuSbS_2$ and Cu_3SbS_4 samples had low carrier concentrations and large effective masses of 3.7 m_e [108]

and 3.0 m_e [110] respectively, they showed very high Seebeck coefficients (> 600 μVK^{-1}). The Cu_3SbS_3 sample had a low carrier concentration as well, but it showed much lower Seebeck coefficient (200~300 μVK^{-1}) due to its small effective mass of 0.453 m_e [77]. The $Cu_{12}Sb_4S_{13}$ sample has a moderate effective mass of 1.3 m_e [64], but its high carrier concentration lead to the lowest Seebeck coefficient in these four compounds.

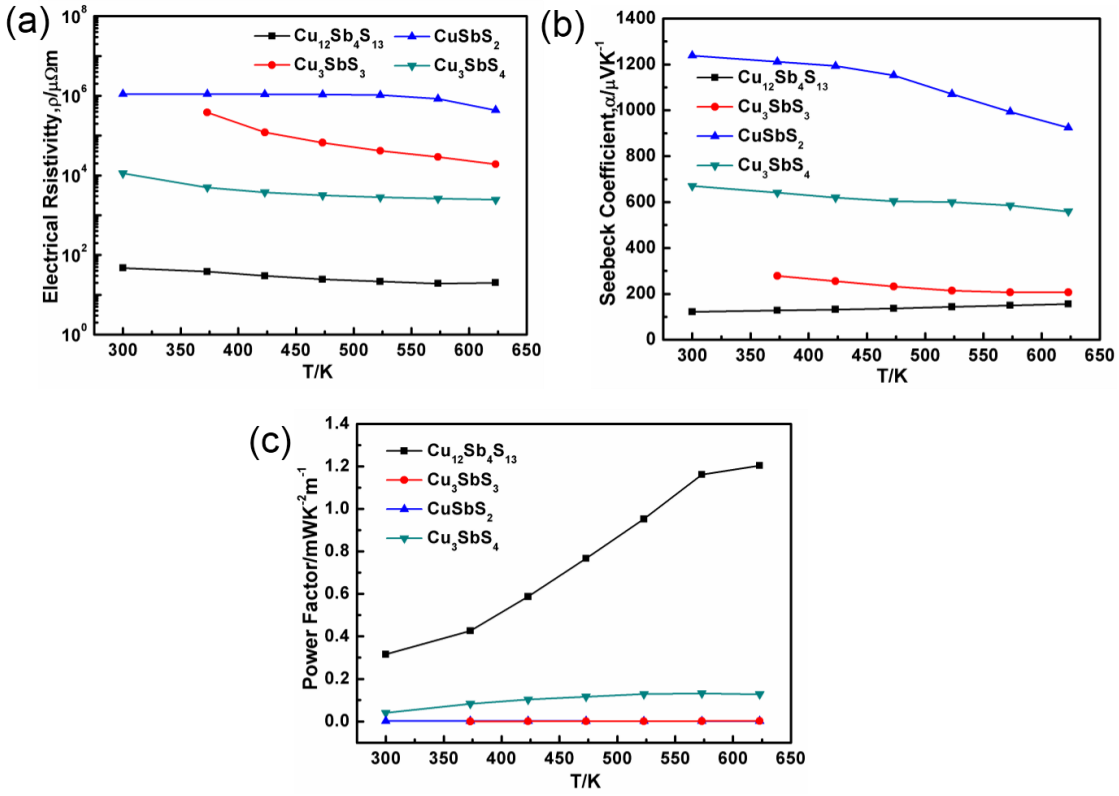

Figure 4.9: *The temperature dependence of (a) electrical resistivities, (b) Seebeck coefficients and (c) power factors for $Cu_{12}Sb_4S_{13}$, Cu_3SbS_3, $CuSbS_2$, and Cu_3SbS_4 samples. Note there is a 5 % uncertainty in all data points.*

However, the values of electrical resistivity (50 to 20 μΩm) and Seebeck coefficient (120~150 μVK^{-1}) obtained for $Cu_{12}Sb_4S_{13}$ were typical for a good thermoelectric material. Therefore, the $Cu_{12}Sb_4S_{13}$ sample showed a high power factor of ~ 1.2 $mWK^{-2}m^{-1}$ at 623 K, which was in agreement with the other reports. Due to the extremely high electrical resistivities of the Cu_3SbS_3 and $CuSbS_2$ samples, they showed very low power factors of lower than 10^{-3} $mWK^{-2}m^{-1}$. The Cu_3SbS_4 sample had a moderate resistivity, but it was still too high for good thermoelectric properties. The maximum power factor obtained in undoped Cu_3SbS_4 sample was only 0.13 $mWK^{-2}m^{-1}$.

Figure 4.10 shows the temperature dependence of thermal conductivities and lattice thermal conductivities for the Cu-Sb-S compounds. The thermal conductivity (κ) is comprised of the electronic thermal conductivity (κ_e) and lattice thermal conductivity (κ_L). The electronic thermal conductivity can be calculated using Wiedemann-Franz law,

$$\kappa_e = LT/\rho$$

Where L is Lorenz number, T is temperature and ρ is electrical resistivity. Due to the high electrical resistivities of the Cu_3SbS_3, $CuSbS_2$ and Cu_3SbS_4 samples, the electronic thermal conductivities were negligible and the lattice thermal conductivities were nearly the same as the total thermal conductivities. The lattice thermal conductivity of $Cu_{12}Sb_4S_{13}$ was calculated by subtracting its electronic thermal conductivity from its total thermal conductivity.

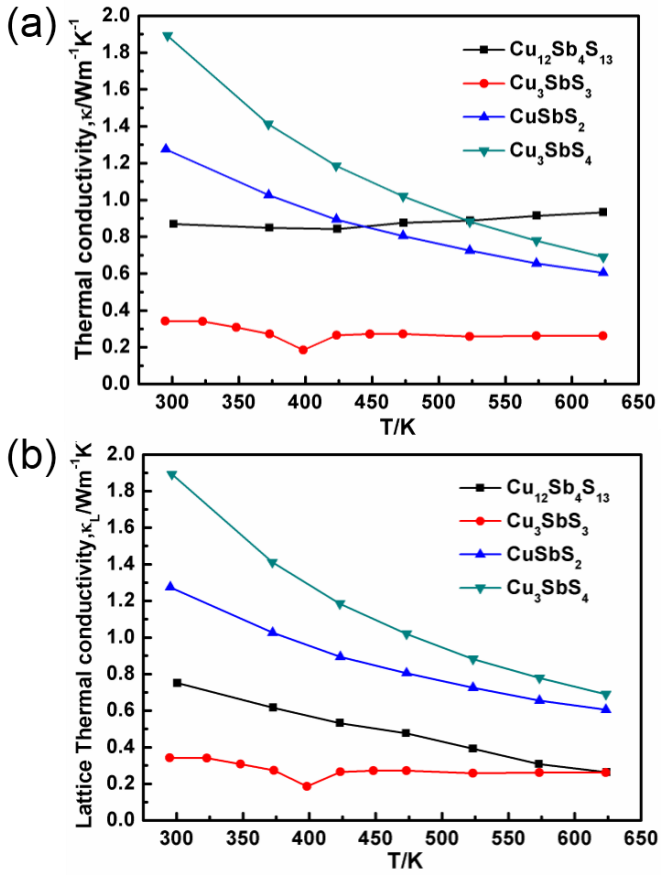

Figure 4.10: *The temperature dependence of (a) thermal conductivities and (b) lattice thermal conductivities for $Cu_{12}Sb_4S_{13}$, Cu_3SbS_3, $CuSbS_2$, and Cu_3SbS_4 samples. Note there is a 10% uncertainty in all data points.*

In order to show the trend of the lattice thermal conductivity, the temperature dependence of the lattice thermal conductivity was plotted individually for each sample as shown in Figure 4.11. Based on the Debye model, if the phonon-phonon scattering (Umklapp process) is the dominant scattering effect, the lattice thermal conductivity above the Debye temperature can be estimated using the equation,

$$\kappa_L = \frac{(6\pi^2)^{2/3}}{4\pi^2}\frac{\bar{M}v_s^3}{TV^{2/3}\gamma^2}$$

Where $\bar{M}$ is the average mass, v_s is the average speed of sound, V is the volume per atom, γ is the Grüneisen parameter and T is temperature (K). For a certain material, the lattice thermal conductivity shows an inverse relation to temperature ($\kappa_L \propto T^{-1}$). As seen in Figure 4.11 (a), (b) and (c), the lattice thermal conductivities of the $Cu_{12}Sb_4S_{13}$, $CuSbS_2$ and Cu_3SbS_4 samples decreased with increasing temperature, following the T^{-1} relation. The results indicated the dominant role of the Umklapp processes in phonon-phonon interactions over a wide temperature range for $Cu_{12}Sb_4S_{13}$, $CuSbS_2$ and Cu_3SbS_4 samples. Due to the order/disorder transition in Cu_3SbS_3 [77], its lattice thermal conductivity showed a very different temperature dependence. As seen in Figure 4.11 (d), the lattice thermal conductivity of the Cu_3SbS_3 sample decreased with increasing temperature at lower temperatures, and then it suddenly dropped to a minimum value of about 0.2 $Wm^{-1}K^{-1}$ at 398 K, which is near the order/disorder transition temperature in Cu_3SbS_3. Above 398K, the lattice thermal conductivity was almost temperature independent. The lattice thermal conductivities showed good agreement between heating and cooling, indicating the transition was reversible.

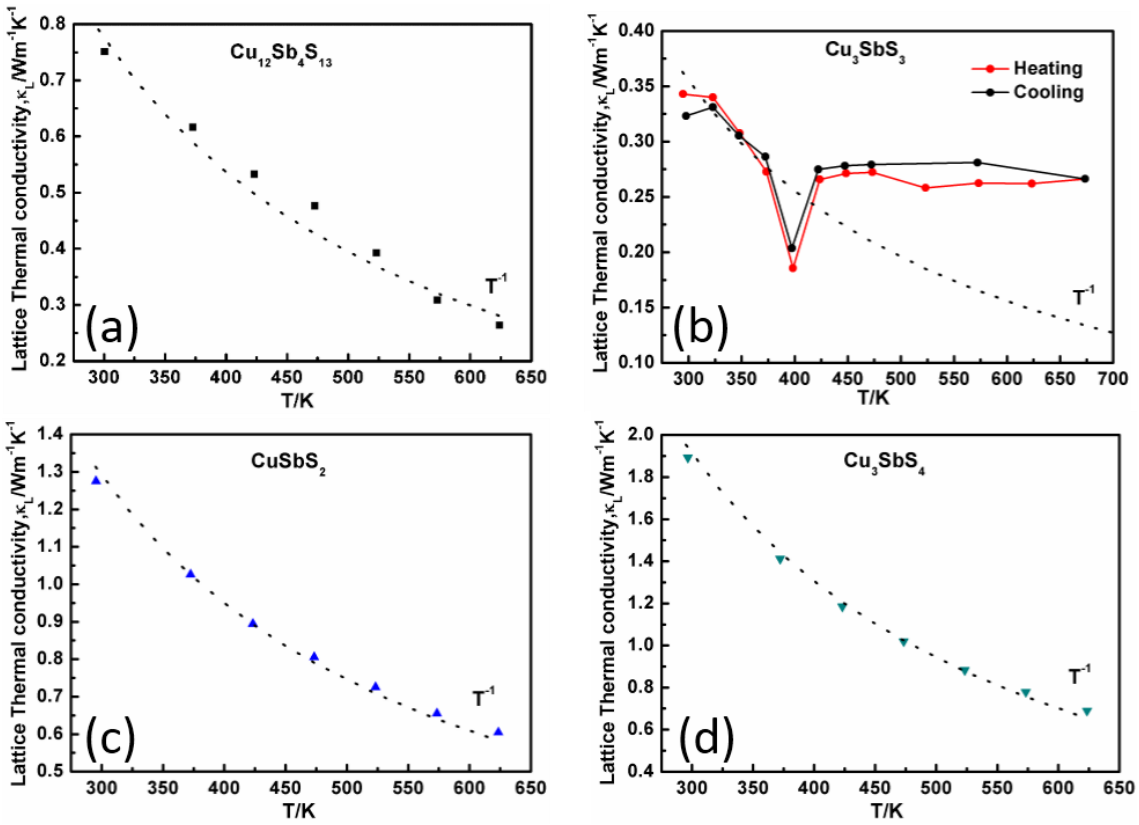

Figure 4.11: *The temperature dependence of lattice thermal conductivity for $Cu_{12}Sb_4S_{13}$, Cu_3SbS_3, $CuSbS_2$ and Cu_3SbS_4 samples, individually. Note there is a 10% uncertainty in all data points.*

As known, the lone-pair electrons of Sb have a significant impact on lattice thermal conductivity, which has been reported for $AgSbTe_2$, Cu_3SbSe_3, $CuSbSe_2$ and $Cu_{12}SbS_{13}$ [16, 55, 111]. Skoug et al. proposed a concept to explain the relationship between lone-pair electrons and lattice thermal conductivity [16]. It was suggested that the electrostatic repulsion between Sb lone-pair electrons and neighboring atoms creates anharmonicity in the lattice, which leads to low thermal conductivity. With larger X-Sb-X bond angle (where X represents a chalcogen atom), the Sb 5s lone-pair electrons are farther removed

away from the Sb nucleus due to Coulomb repulsion, which can intensify the anharmonic interactions with adjacent atoms and lower lattice thermal conductivity.

In the case of Cu-Sb-S compounds, the value of lattice thermal conductivity was in order of Cu_3SbS_4 > $CuSbS_2$ > $Cu_{12}Sb_4S_{13}$ > Cu_3SbS_3, as seen in Figure 4.10 (b). The difference in the lattice thermal conductivity can be explained using the concept of lone-pair electrons, and the average bond angles of S-Sb-S in these compounds are shown in Figure 4.12. The outer shell electrons of Sb atoms in Cu_3SbS_4 are fully bonded and Sb atoms are coordinated with four sulfur atoms forming [SbS4] tetrahedrons. There are no lone-pair electrons in Cu_3SbS_4, so it shows the highest lattice thermal conductivity. Among the other three compounds with lone-pair electrons, Cu_3SbS_3 has the largest S-Sb-S bond angle, which imparts it with the lowest lattice thermal conductivity. However, it is worth noting that $CuSbS_2$ and $Cu_{12}Sb_4S_{13}$ have similar S-Sb-S bond angles, but $Cu_{12}Sb_4S_{13}$ shows lower lattice thermal conductivity than that of $CuSbS_2$. This is because of the extra phonon scattering introduced by the anharmonic rattling of Cu in [CuS3] trigonal plane of $Cu_{12}Sb_4S_{13}$ [55]. The results indicate that the local bonding asymmetry, such as three-coordinated Sb and three-coordinated Cu, can help to achieve low thermal conductivity. Although it is difficult to design and realize such bonding asymmetry in known materials, it can be used as a guideline to search for new thermoelectric materials with low lattice thermal conductivity.

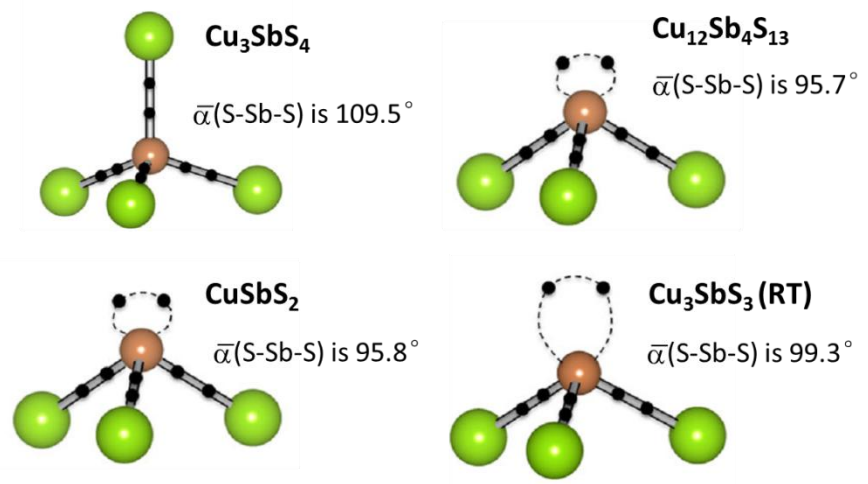

Figure 4.12: *The average bond angles of S-Sb-S for Cu_3SbS_4 [90], $Cu_{12}Sb_4S_{13}$ [112], $CuSbS_2$ [113], and Cu_3SbS_3 [114], individually.*

Figure 4.13 shows the temperature dependence of *zT* value for the Cu-Sb-S ceramics. The $Cu_{12}Sb_4S_{13}$ has the highest *zT* value, and a maximum value of 0.8 was achieved at 623 K which is consistent with the other reports [17, 54, 58]. The other three compounds show much lower *zT* values, due to their poor electrical properties. The Cu_3SbS_4 has a maximum *zT* value of 0.12 at 623 K, while the $CuSbS_2$ and Cu_3SbS_3 have the *zT* values lower than 0.01. The thermoelectric properties of Cu_3SbS_4, $CuSbS_2$ and Cu_3SbS_3 are very poor mainly due to their high electrical resistivities.

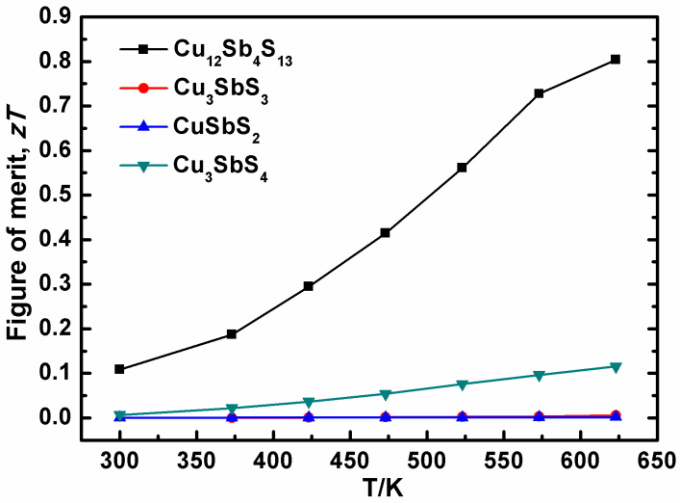

Figure 4.13: *The temperature dependence of zT value for $Cu_{12}Sb_4S_{13}$, $CuSbS_2$, Cu_3SbS_4 and Cu_3SbS_3 samples. Note there is a 20 % uncertainty in all data points.*

4.3.3 Attempts to Optimize Electrical Properties of $CuSbS_2$

From previous results, the $CuSbS_2$ was found to have a low thermal conductivity of 1.3 $Wm^{-1}K^{-1}$ at 300 K, which drops to 0.6 $Wm^{-1}K^{-1}$ at 623 K and has a high Seebeck coefficient above 900 μVK^{-1}. However, it has an extremely high electrical resistivity of 10^6 $\mu\Omega m$ which leads to a very low *zT* value. So the key point to improve the thermoelectric performance of the $CuSbS_2$ is reducing the electrical resistivity by proper dopant. As the main carriers in the $CuSbS_2$ are holes, its electrical resistivity can be reduced by introducing more holes in the system. The elements of Sn, In and Co are chosen to dope on Sb site, which have less outer shell electrons and smaller ionic radius compared with Sb. Figure 4.14 shows the XRD results of the $CuSbS_2$ with different

dopants. Second phases were observed in all doped samples, which indicate these elements are not able to substitute Sb or have very low solubility in $CuSbS_2$. The room temperature electrical resistances of all doped samples were measured by ohmmeter and there was no obvious change in the electrical resistance. It seems very difficult to introduce holes by substituting Sb with other elements in the $CuSbS_2$ system.

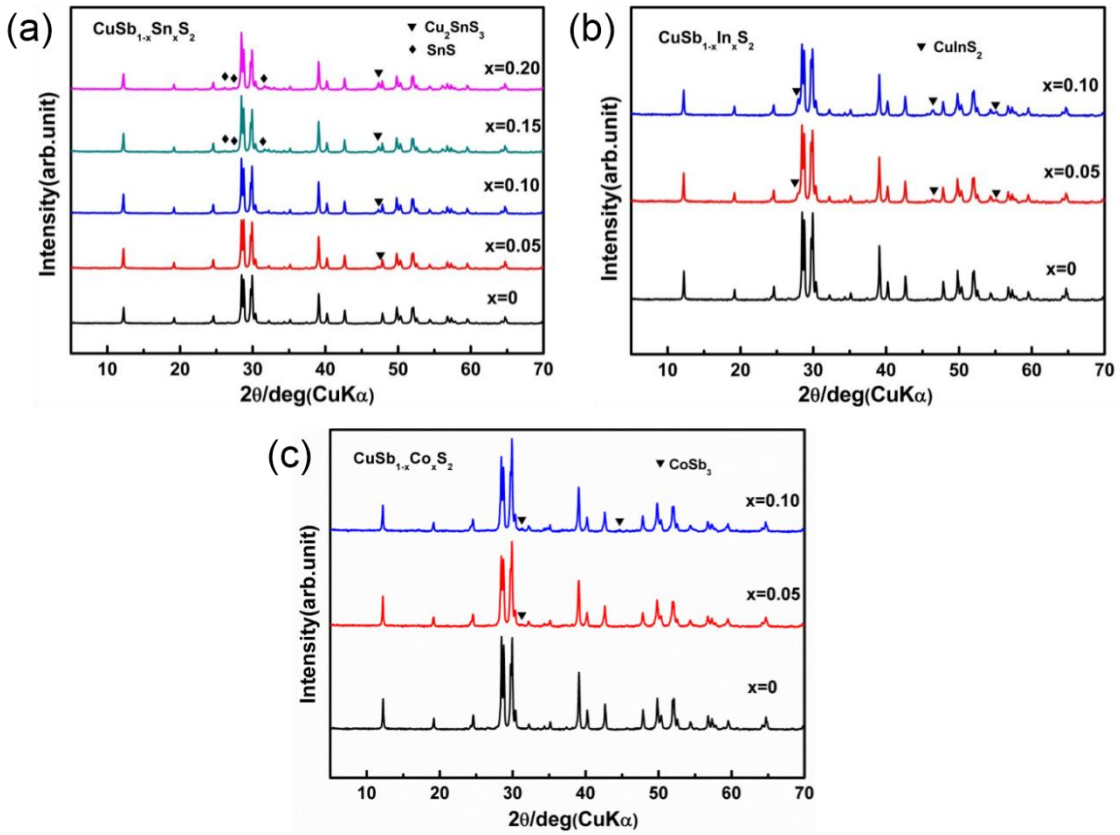

Figure 4.14: *The XRD results of $CuSbS_2$ with (a) Sn-doping, (b) In- doping and (c) Co-doping.*

Besides, the Cu deficiency can introduce extra holes theoretically and it was reported in the Cu_3SbSe_4 system [98]. Therefore, the $Cu_{1-x}SbS_2$ (x = 0.005, 0.01, 0.02 and 0.05)

samples were prepared and the XRD results are shown in Figure 4.15. All the peaks can be indexed as a main phase $CuSbS_2$ except a second phase of Sb_2S_3 was observed when Cu deficiency level increases to 0.05. It indicates $CuSbS_2$ has a stoichiometric range up to 5 mol. % Cu deficiency. The room temperature electrical resistances of all samples were measured by ohmmeter. Still there was no obvious change in the electrical resistance, and it was too large for thermoelectric applications.

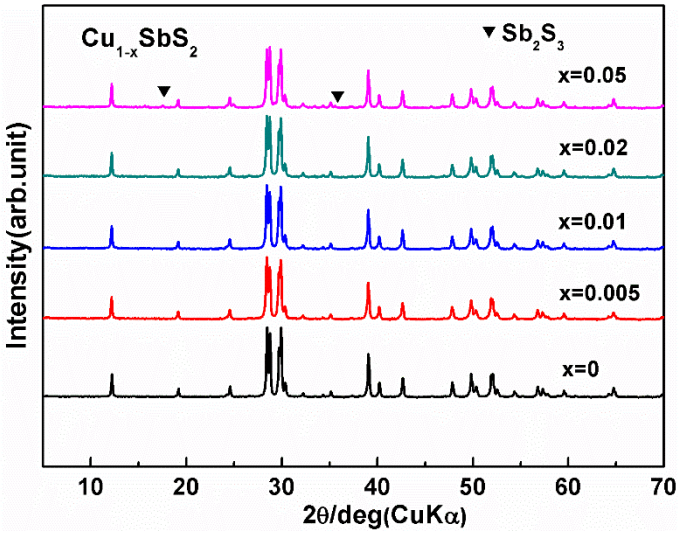

Figure 4.15: *The XRD results of $Cu_{1-x}SbS_2$ (x = 0 ~ 0.05) samples.*

4.4 Conclusions

The synthesis methods of melt + SPS and MA + SPS to prepare Cu_3SbS_4 compound were compared. The results indicate that the MA + SPS processing route can produce very fine microstructures and the small grains of 100 ~ 300 nm can introduce effective phonon scattering (more grain boundaries) which leads to a much lower thermal conductivity. All

four Cu-Sb-S compounds prepared by this method had high purity and high density. The lone-pair electrons of Sb and the [CuS3] plane play important roles in realizing very low lattice thermal conductivity. The lattice thermal conductivities of $Cu_{12}Sb_4S_{13}$, $CuSbS_2$ and Cu_3SbS_4 were governed by Umklapp phonon scattering, and a T^{-1} dependence was observed for these samples. A phase transition at 398 K was found in Cu_3SbS_3, which is similar to that in Cu_3SbSe_3. Except for $Cu_{12}Sb_4S_{13}$, which is known as a good thermoelectric material, the other three compounds showed very poor thermoelectric performance due to their high electrical resistivities. It is noteworthy that the phase transition in Cu_3SbS_3 will cause mechanical problems, which makes it unsuitable for application, in spite of its extremely low thermal conductivity (lower than 0.35 $Wm^{-1}K^{-1}$). Although $CuSbS_2$ has very low thermal conductivity as well, its large band gap and complex structure lead to the difficulty in improving its electrical properties by doping. Attempts to optimize electrical properties of $CuSbS_2$ were failed in this work. Therefore, more work was focused on Cu_3SbS_4 compounds to improve its thermoelectric properties.

Chapter 5 Thermoelectric Properties of Ge-doped Cu_3SbS_4

5.1 Introduction

Cu_3SbS_4 is isostructural and isoelectronic to the good p-type thermoelectric material Cu_3SbSe_4 (zT value is above 0.8 at 650 K) [95] and it has the advantages of low-cost and low-toxicity. The results in last chapter showed that Cu_3SbS_4 had a high Seebeck coefficient of about 600 μVK^{-1}, and a relatively low lattice thermal conductivity of 1.9 $Wm^{-1}K^{-1}$ at 300 K, which dropped to 0.7 $Wm^{-1}K^{-1}$ at 623 K. But it had a high electrical resistivity of about 10^{-2} Ωm, which led to a low power factor and a low zT value. In order to improve the thermoelectric performance of Cu_3SbS_4, Ge was chosen as a p-type dopant on the Sb site to optimize the carrier concentration, as Ge-doping can introduce extra holes into the system. The microstructures and thermoelectric properties of $Cu_3Sb_{1-x}Ge_xS_4$ (x = 0, 0.0125, 0.025, 0.05, 0.075, 0.1 and 0.15) samples were investigated from 300 K to 623 K. Ge was found to be an effective dopant, but it partially formed a second phase. The second phase did not show obvious effect on the transport properties of the samples. The power factor was largely enhanced with optimized carrier concentration. A high zT value of 0.63 was obtained at 623 K in Ge-doped Cu_3SbS_4, which is four times higher than that of undoped Cu_3SbS_4.

5.2 Experimental Details

Polycrystalline $Cu_3Sb_{1-x}Ge_xS_4$ samples with nominal Ge doping of x = 0, 0.0125, 0.025, 0.05, 0.075, 0.1 and 0.15 were prepared by mechanical alloying (MA) combined with spark plasma sintering (SPS) (FCT, Rauenstein, Germany). 15g of starting elements of Cu (99.5 %, AlfaAesar), Sb (99.5 %, AlfaAesar), Ge (99.999 %, AlfaAesar), and S (reagent grade, purified by sublimation, Sigma-Aldrich) were ball milled with a powder to ball weight ratio of 1:20 in argon for 20 h. The obtained powders were loaded into a graphite die, and sintered using SPS at 723 K for 3 min under a pressure of 60 MPa.

5.3 Results and Discussions

Polycrystalline $Cu_3Sb_{1-x}Ge_xS_4$ bulk samples were examined by XRD and the results can be seen in Figure 5.1. The samples with Ge amount below 0.1 were phase pure as all the peaks could be indexed to standard data of Cu_3SbS_4 (PDF: 00-035-0581). For the x = 0.1 and 0.15 samples, an extra peak belonging to Cu_2GeS_3 was observed. From the enlarged figure, it can be seen that the peaks of Cu_3SbS_4 shift to slightly higher angles with increasing Ge content, as a result of the fact that Ge has a slightly smaller ionic radius than that of Sb. Unexpectedly, not only for the x = 0.1 and 0.15 samples, the second phase was also seen in SEM images of all the Ge-doped samples. Figure 5.2 shows the fracture surface of the sample with lowest Ge-doping amount (x = 0.0125). From Figure 5.2 (a), (b) and (c), it can be seen that the sample had very fine grains, similar to that of the undoped samples. However, a second phase was found when checking the surface very

carefully, and it was very distinctive from the main phase as shown in Figure 5.2 (d).

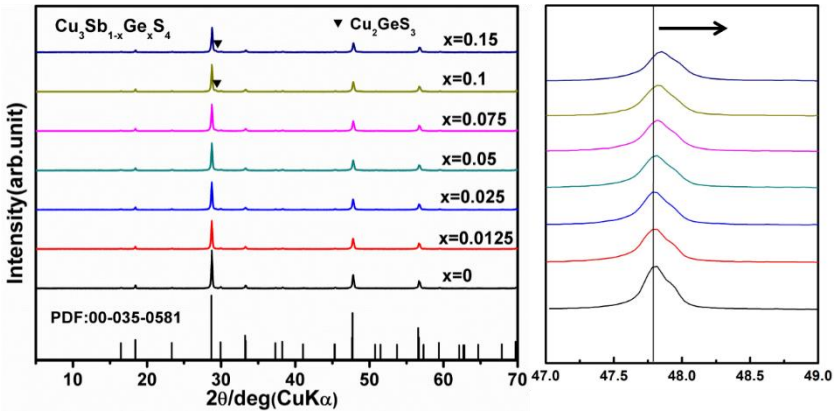

Figure 5.1: *XRD patterns of $Cu_3Sb_{1-x}Ge_xS_4$ (x = 0 ~ 0.15) samples and the enlarged figure shows the peak shift.*

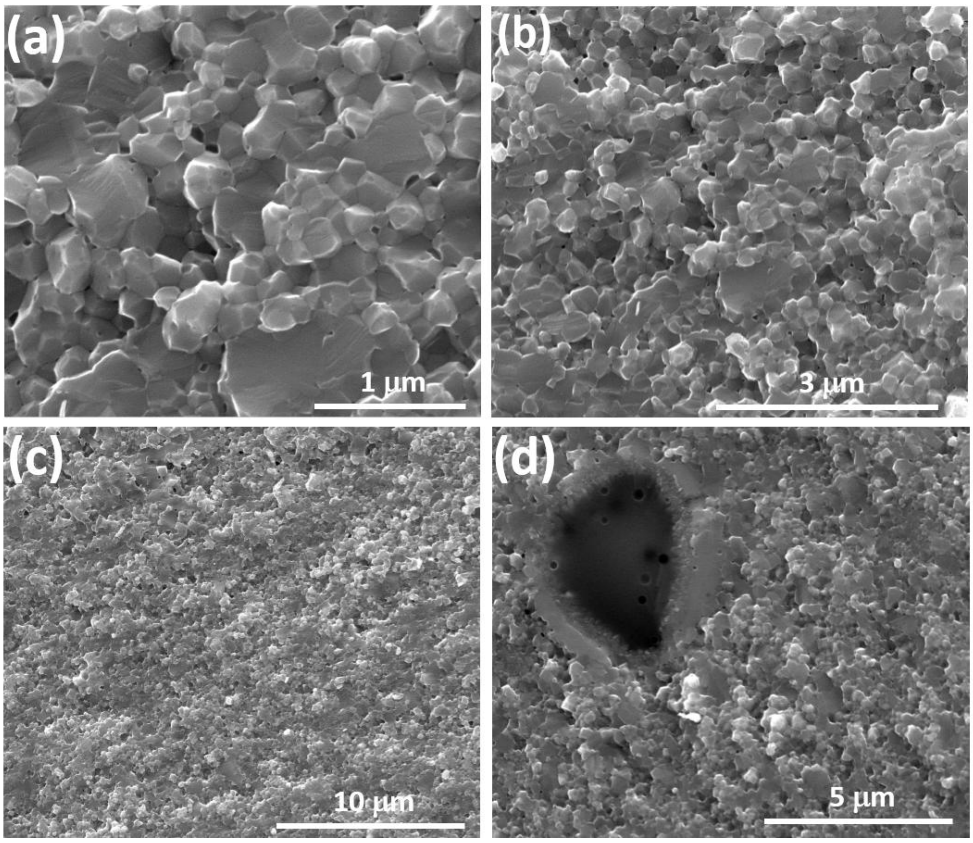

Figure 5.2: *SEM images of fracture surface for $Cu_3Sb_{1-x}Ge_xS_4$ (x = 0.0125) sample.*

Figure 5.3 shows SEM images of samples with higher Ge-doping. It can be seen that an increasing amount of second phase was observed with increasing Ge doping. All the second phase particles have similar round-like shape, and the size of the second phase is about several micrometer, which is much larger than the grain size of the main phase.

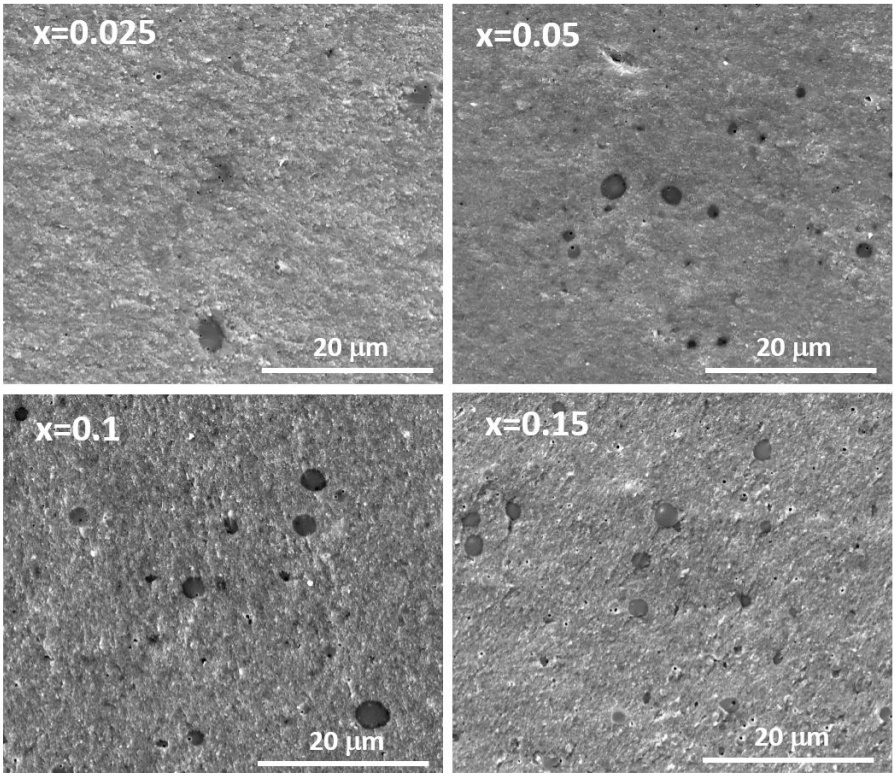

Figure 5.3: *SEM images of fracture surface for $Cu_3Sb_{1-x}Ge_xS_4$ (x = 0.025, 0.05, 0.1 and 0.15) samples.*

A typical area containing the second phase was chosen for EDX analysis as shown in Figure 5.4. The spectrum A and B are the EDX results obtained from the second phase and the main phase, respectively, which indicate the second phase is Ge-rich. Combined with XRD results, the second phase was identified as Cu_2GeS_3. From the phase analysis

and microstructures of the Ge-doped samples, it was found that Ge was not fully doped on Sb sites as it was partially forming a second phase. This resulted in the actual doping level being lower than the nominal doping level for $Cu_3Sb_{1-x}Ge_xS_4$ samples.

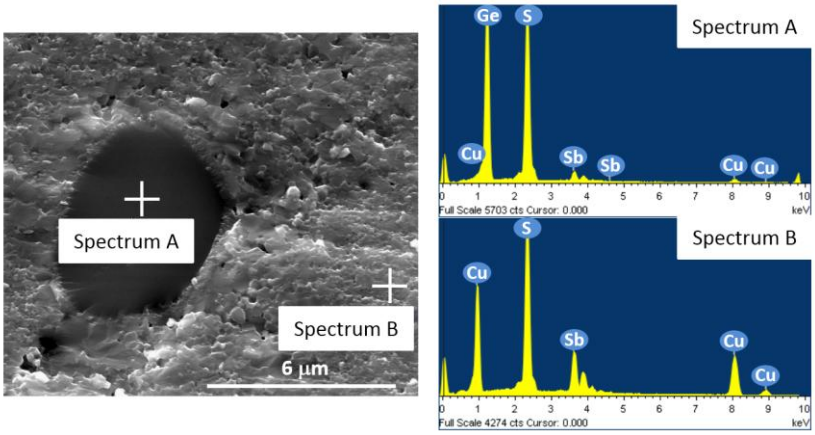

Figure 5.4: *EDX analysis for Ge-doped Cu_3SbS_4 with the second phase.*

Table 5.1 shows the room temperature physical properties of the $Cu_3Sb_{1-x}Ge_xS_4$ samples. All the samples had positive Hall coefficients suggesting they are p-type semiconductors, which is consistent with their positive Seebeck coefficients. The undoped Cu_3SbS_4 is an intrinsic semiconductor with a carrier concentration of around 10^{17} cm^{-3}. With Ge doping, the carrier concentration was increased up to 4.79×10^{20} cm^{-3}, which indicates Ge is an effective p-type dopant. Due to the increased carrier concentration, the electrical resistivity was largely reduced, while the carrier mobility and Seebeck coefficient dropped. For samples with high carrier concentrations (above 10^{20} cm^{-3}), there is a 20 % uncertainty in Hall measurements which makes the change of mobility mainly caused by error.

Table 5.1 *Room temperature Hall coefficient, carrier concentration, carrier mobility, Seebeck coefficient and electrical resistivity of $Cu_3Sb_{1-x}Ge_xS_4$ (x = 0 ~ 0.15) samples.*

Nominal doping	Hall coefficient R_H (cm^3C^{-1})	Carrier concentration n (10^{20} cm^{-3})	Carrier mobility μ ($cm^2V^{-1}s^{-1}$)	Electrical resistivity ρ (μΩm)	Seebeck coefficient α (μVK^{-1})
x = 0	19	0.0032	16.4	11231.9	670.1
x = 0.0125	0.45	0.13	9.3	625.3	351.7
x = 0.025	0.19	0.33	6.8	196.3	284.5
x = 0.05	0.064	0.98	5.3	107.5	208.7
x = 0.075	0.039	1.61	5.3	49.1	174.2
x = 0.10	0.020	3.07	5.2	35.7	150.8
x = 0.15	0.013	4.79	5.3	19.4	113.7

As Ge was partially forming a second phase in all Ge-doped samples, the actual doping level is lower than the expected doping level as shown in Figure 5.5. The solid line represents the theoretical carrier concentration assuming each Ge atom provides one hole to $Cu_3Sb_{1-x}Ge_xS_4$. The actual doping level was approximately half of the nominal doping level.

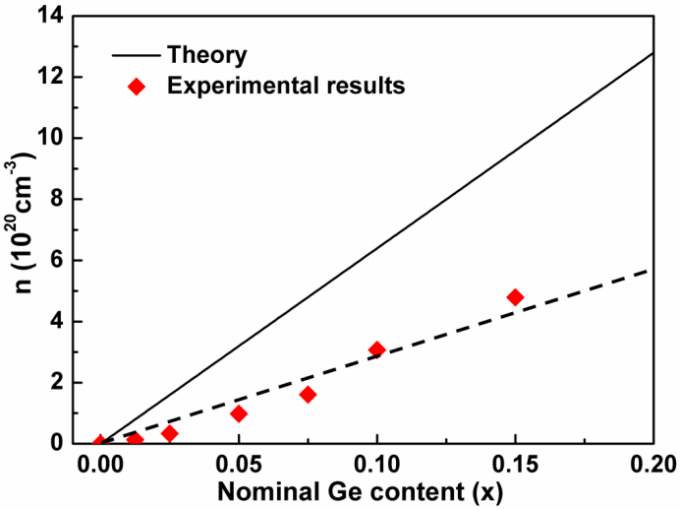

Figure 5.5: *The theoretical and experimental carrier concentration as a function of nominal Ge content in $Cu_3Sb_{1-x}Ge_xS_4$ system.*

The thermoelectric properties of Ge-doped Cu_3SbS_4 samples were investigated from 300 K to 623 K. The temperature dependence of the electrical resistivity, Seebeck coefficient and power factor are shown in Figure 5.6. The electrical resistivity was significantly reduced by the Ge doping over the investigated temperature range. The undoped sample showed semiconductor type transport behavior, as its electrical resistivity decreased with increasing temperature. Due to the increased carrier concentration, the Ge-doped samples showed metal-like transport behavior, as their electrical resistivities increased with increasing temperature. The Seebeck coefficient had a similar temperature dependence to the electrical resistivity for every sample. With increasing Ge-doping amount, the Seebeck coefficient dropped due to the increased carrier concentration. It is common in thermoelectric materials that the Seebeck coefficient is sacrificed when reducing the electrical resistivity. However, the power factor was significantly enhanced with Ge-doping. A maximum power factor of 1.08 $mWK^{-2}m^{-1}$ was achieved at 623 K in the x = 0.15 sample with carrier concentration of 4.79×10^{20} cm^{-3}, which was about 10 times larger than that of the undoped sample. This value is similar to the optimized value of 1.05 ~ 1.3 $mWK^{-2}m^{-1}$ in Cu_3SbSe_4 [94, 95, 100].

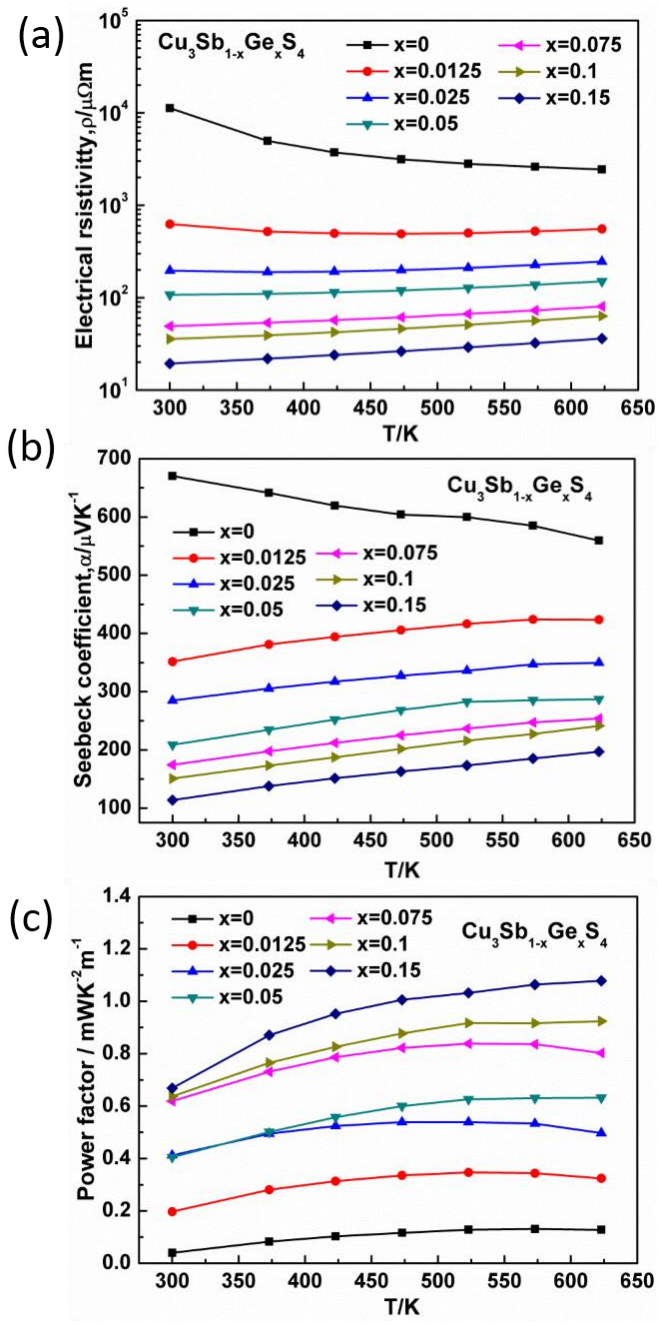

Figure 5.6 *The temperature dependence of (a) electrical resistivity, (b) Seebeck coefficient and (c) power factor for $Cu_3Sb_{1-x}Ge_xS_4$ (x = 0 ~ 0.15) samples. Note there is a 5 % uncertainty in all data points.*

To investigate the impact of Ge-doping on the electronic structure of Cu_3SbS_4, the experimental results were analyzed within a single parabolic band (SPB) model. The SPB

model is based on Boltzmann transport equation and the relaxation time approximation [115], which is widely used in thermoelectric materials. In the SPB model, the Seebeck coefficient (α) and carrier concentration (n) can be written as Equation 5.1 and Equation 5.2.

$$\alpha = \pm \frac{k_B}{e}\left[\frac{(2+r)F_{1+r}(\eta)}{(1+r)F_r(\eta)} - \eta\right] \quad 5.1$$

$$n = \frac{4\pi(2k_B T m^*)^{3/2}}{h^3} F_{1/2}(\eta) \quad 5.2$$

$$F_i(\eta) = \int_0^\infty \frac{x^i dx}{1+\exp(x-\eta)} \quad 5.3$$

Where k_B is the Boltzmann constant, e is the elementary charge, r is the scattering factor (In this work, the acoustic phonon scattering is assumed to be dominant for charge carrier transport, r = 0.), h is the Planck constant, m^* is the density-of-state effective mass for carrier, η is the reduced Fermi energy, $F_i(\eta)$ is the Fermi integral defined in Equation 5.3 and x is the reduced energy. Based on the experimental α and n, the m^* can be estimated using these equations. The carrier concentration dependence of Seebeck coefficient at 300 K is shown in Figure 5.7. The solid line represents the theoretical dependence with m^* = 3.0 m_e, which is also known as Pisarenko line. The doped samples with second phase are on the same Pisarenko line as the undoped sample (phase pure), indicating that the transport properties of the samples are dominated by the Cu_3SbS_4 phase and the Ge-doping and the second phase had on obvious impact on the electronic structure as m^* was

unchanged. However, it is worth noting that the calculated results for heavily doped samples (above 10^{20} cm^{-3}) could have significant errors, as there are more complicated scattering mechanisms in heavily doped materials.

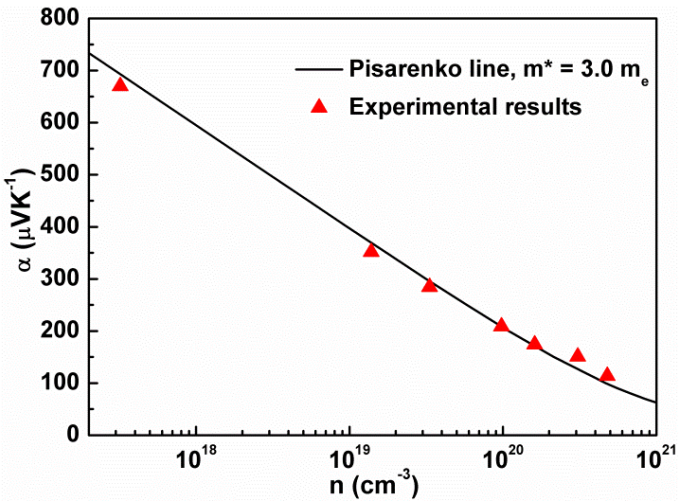

Figure 5.7 *The carrier concentration (n) dependence of Seebeck coefficient (α) at 300 K and the Pisarenko line with m* = 3.0 m_e.*

A theoretical calculation of Cu_3SbS_4 based on density functional theory (DFT) was done by Dr Cedric Weber and Dr Bonini Nicola at King's College as part of a collaboration. Figure 5.8 shows the calculated band structure and corresponding density-of-state (DOS) for Cu_3SbS_4. A band gap of ~ 0.6 eV was determined by the energy difference between the conduction band minimum (CBM) and the valence band maximum (VBM), which is consistent with reported results [116]. A distinctive feature here is the presence of three distinct bands at VBM at Γ, which results in a high density of state at the band edge. The density-of-state effective mass (m^*) of holes computed from DFT is 2.2 m_e, which is

slightly different from the m^* estimated using the SPB model (3.0 m_e). This suggests that effects beyond the single band approximation are important, but can be effectively simulated by an increased effective mass. However, both results reveal Cu_3SbS_4 has very large m^* among thermoelectric materials. As is known, a large m^* is favourable for high Seebeck coefficient. It can be used to explain the high Seebeck coefficient (670 μVK^{-1} at 300 K) of Cu_3SbS_4, which is higher than the value (375 μVK^{-1} at 300 K) reported in Cu_3SbSe_4 with a m^* of about 1.5 m_e (estimated by SPB model) [99].

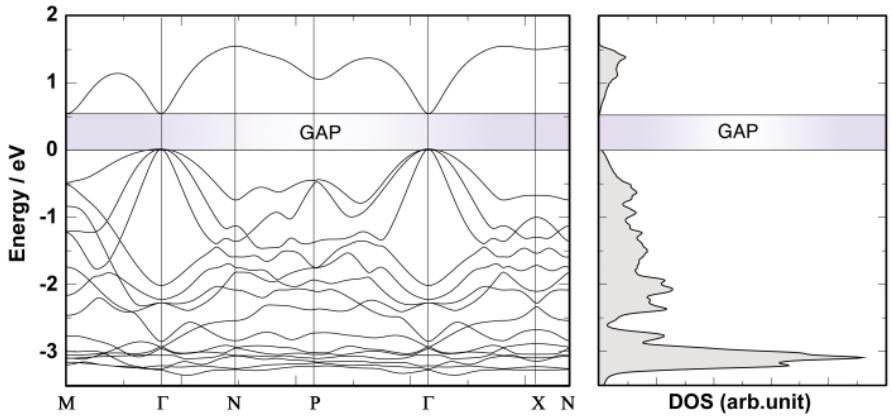

Figure 5.8 *The calculated band structure of Cu_3SbS_4 (left) and corresponding density-of-state (DOS) (right).* (*The results are courtesy of C. Weber and N. Bonini, King's College, London.)*

To assess the effect of Ge-doping on the electronic structure of Cu_3SbS_4, the density-of-state of Ge-doped $Cu_3Sb_{1-x}Ge_xS_4$ (x = 0.125) was calculated. As shown in Figure 5.9, compared with the density-of-state of undoped Cu_3SbS_4, the extra holes introduced by the Ge dopants resulted in a shift of the Fermi level, without altering the high density-of-

state at the band edge of the undoped compound. This is consistent with the SPB result, as a constant density-of-state effective mass was estimated for all samples. Also the power factor of Ge-doped Cu_3SbS_4 at 600 K was calculated based on DFT and Boltzmann transport theory. As seen in Figure 5.10, the solid line represents the calculated power factor as a function of carrier concentration at 600 K. The power factor reaches a maximum value with a carrier concentration of about 7×10^{20} cm^{-3}. If we assume the carrier concentration does not change at 600 K since the doped samples exhibited metal-like behaviors, the experimental power factor (■) shows good agreement with the calculated results. The predicted maximum power factor was nearly achieved in the x = 0.15 sample with a carrier concentration of 4.79×10^{20} cm^{-3}.

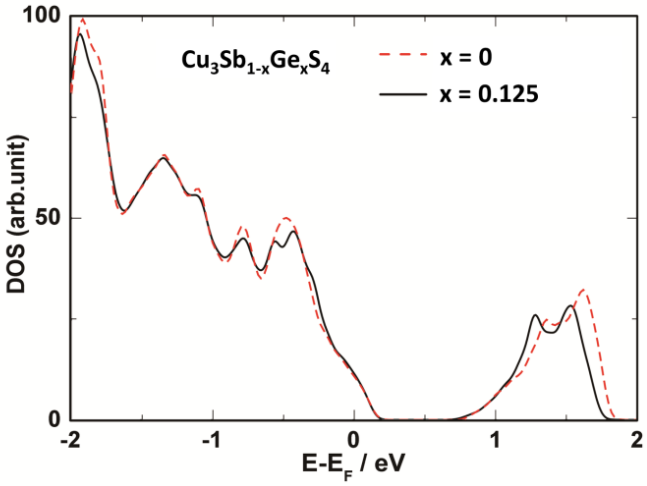

Figure 5.9 *The density-of-state of undoped Cu_3SbS_4 and Ge-doped Cu_3SbS_4. The DOS of undoped Cu_3SbS_4 has been shifted to account for the extra hole introduced by Ge-doping. (The results are courtesy of C. Weber and N. Bonini, King's College, London.)*

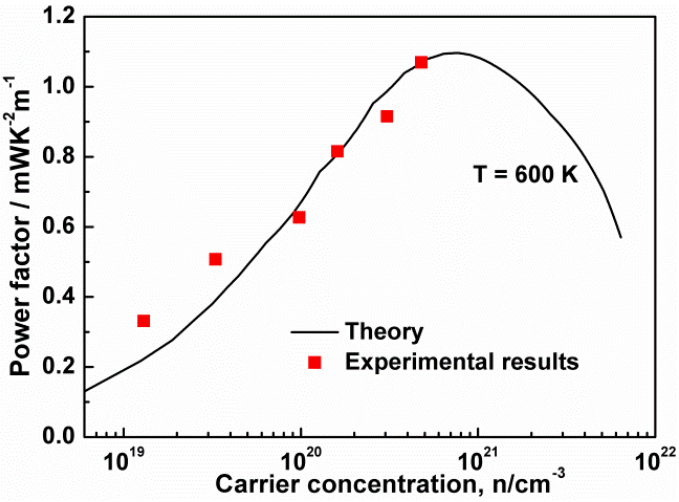

Figure 5.10 *The theoretical and experimental power factor (PF) as a function of carrier concentration (n) at 600 K. (The results are courtesy of C. Weber and N. Bonini, King's College, London.)*

The thermal transport properties of $Cu_3Sb_{1-x}Ge_xS_4$ samples were investigated from 300 K to 623 K. Figure 5.11 shows the temperature dependence of the total thermal conductivities of all of the samples. The total thermal conductivity decreased with increasing temperature and there was no sign of bipolar effects. With increasing Ge doping, the thermal conductivity increased over the investigated temperature range due to the increased electronic contribution.

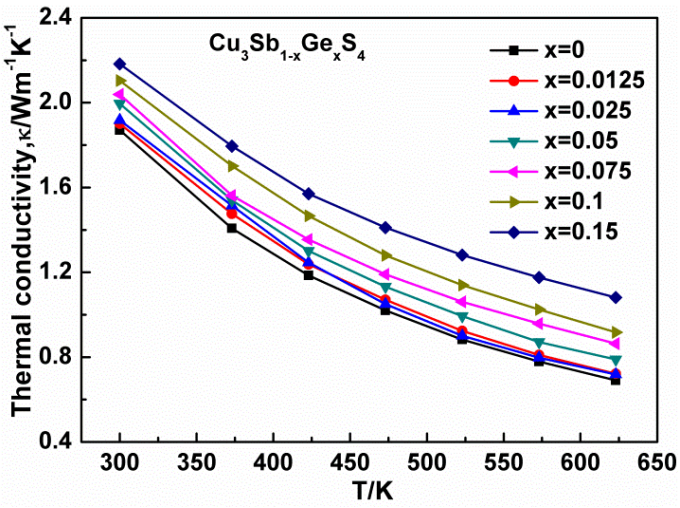

Figure 5.11 *The temperature dependence of total thermal conductivity for $Cu_3Sb_{1-x}Ge_xS_4$ (x = 0 ~ 0.15) samples. Note there is a 10% uncertainty in all data points.*

The lattice thermal conductivity (κ_L) was calculated by subtracting the electronic thermal conductivity (κ_e) from the total thermal conductivity, $\kappa_L = \kappa - \kappa_e$. The κ_e was estimated based on the Wiedemann-Franz law, $\kappa_e = LT/\rho$, where L is the Lorenz number. Based on the classical free-electron model the L was determined as 2.44×10^{-8} $W\Omega K^{-2}$ by Sommerfeld in 1927 [117], which is often used to estimate the lattice thermal conductivity at room temperature for metals or heavily doped semiconductors. But this value is not accurate for most materials as L is related to the detailed band structure, position of the Fermi level, carrier concentration and the temperature [118]. To obtain a more accurate evaluation of the lattice thermal conductivity, the Lorenz number for $Cu_3Sb_{1-x}Ge_xS_4$ was calculated within the SPB model, where L can be written as Equation 5.4.

$$L = \frac{k_B}{e^2}\left[\frac{(1+r)(3+r)F_r(\eta)F_{1+r}(\eta) - (2+r)^2 F_{r+1}^2(\eta)}{(1+r)^2 F_r^{\,2}(\eta)}\right] \qquad 5.4$$

Combined with Equation 5.1 and 5.3, L was calculated form the experimental Seebeck coefficient as shown in Figure 5.12 (a). The values are between 1.49×10^{-8} $W\Omega K^{-2}$ and 1.85×10^{-8} $W\Omega K^{-2}$ which are smaller than 2.44×10^{-8} $W\Omega K^{-2}$. Figure 5.12 (b) shows the temperature dependence of the lattice thermal conductivity for all of the samples. The lattice thermal conductivities of all of the samples decreased with increasing temperature following a T^{-1} relation, indicating that phonon–phonon scattering (Umklapp process) was dominant for thermal transport over the investigated temperature range [28]. The lattice thermal conductivity of undoped Cu_3SbS_4 is about 1.9 $Wm^{-1}K^{-1}$ at room temperature and drops to 0.7 $Wm^{-1}K^{-1}$ at 623 K. These values are much lower than the reported value of a sample prepared using the solid reaction method [103]. This low lattice thermal conductivity was a benefit from the MA and SPS processing, which produced a much smaller grain size (100 ~ 300 nm) than the solid state reaction method (3 ~ 10 μm). With increasing Ge doping, the lattice thermal conductivity slightly increased due to the second phase with its large grain size. The x = 0.15 sample has the highest lattice thermal conductivity of 0.8 $Wm^{-1}K^{-1}$ at 623 K.

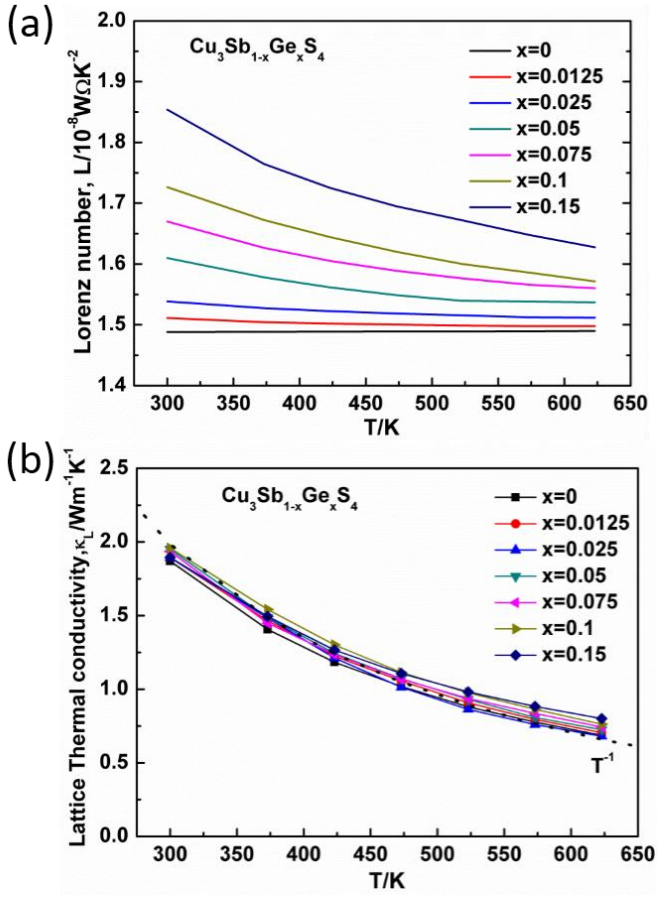

Figure 5.12 *(a) The calculated Lorenz number and (b) the temperature dependence of lattice thermal conductivity for $Cu_3Sb_{1-x}Ge_xS_4$ (x = 0 ~ 0.15) samples. Note there is a 10 % uncertainty in all data points.*

Figure 5.13 shows the temperature dependence of the *zT* value for the $Cu_3Sb_{1-x}Ge_xS_4$ samples. The *zT* value of all of the samples increased linearly with increasing temperature. With Ge-doping, the *zT* value was significantly enhanced, due to the improvement in electrical properties. Combined with the low lattice thermal conductivity, a maximum *zT* value of about 0.63 was achieved at 623 K in both the x = 0.1 and 0.15 samples, which is

about 6 times higher than that of undoped Cu_3SbS_4.

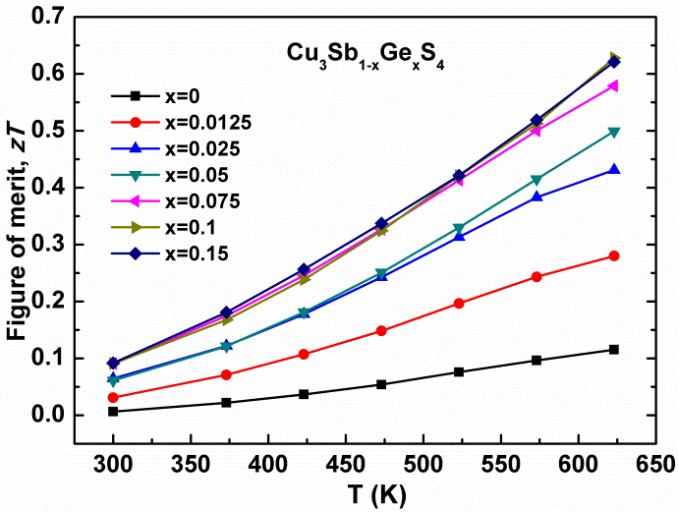

Figure 5.13 *The temperature dependence of the zT value for $Cu_3Sb_{1-x}Ge_xS_4$ (x = 0 ~ 0.15) samples. Note there is a 20 % uncertainty in all data points.*

5.4 Conclusions

Polycrystalline Ge-doped Cu_3SbS_4 samples were prepared by mechanical alloying and spark plasma sintering. All of the samples had very fine microstructures with grain size of 50 ~ 300 nm, which resulted in a low lattice thermal conductivity. Ge doping produced small amount of second phase Cu_2GeS_3, but it was still working as an effective p-type dopant, increasing the carrier concentration up to 4.79×10^{20} cm^{-3}. The transport properties were analysed using the single parabolic band (SPB) model, and a large effective mass of 3.0 m_e was estimated for undoped and Ge-doped Cu_3SbS_4. This large m^* was derived from the three degenerate bands at VBM in the calculated band structure.

Ge doping slightly shifted the Fermi level, without altering the electronic structure of Cu_3SbS_4. The thermal conductivity was dominated by Umklapp phonon scattering, and a T^{-1} dependence was observed for all samples. The second phase of Cu_2GeS_3 had no obvious effect on the transport properties. A maximum zT value of 0.63 was obtained at 673 K in Cu_3SbS_4 samples with 10 mol. % and 15 mol. % Ge doping.

Chapter 6 Thermoelectric Properties of Sn-doped Cu_3SbS_4

6.1 Introduction

As discussed in the previous chapter, Ge-doped Cu_3SbS_4 has promising thermoelectric properties. The power factor was improved with Ge-doping on the Sb site, and resulted in an enhanced zT value of 0.63 at 673 K. However, a second phase of Cu_2GeS_3 was found in Ge-doped Cu_3SbS_4 samples and Ge was only a partial dopant. In contrast to Ge, Sn has a closer ionic radius and similar valance configuration to Sb, which are $4d^{10}5s^25p^2$ and $4d^{10}5s^25p^3$, respectively. It suggests Sn could have higher solubility in Cu_3SbS_4 than Ge, without forming any second phase. With one less outer shell electron, Sn also can introduce extra holes by substituting for Sb. Thus, the phase structures, microstructures and thermoelectric properties of $Cu_3Sb_{1-x}Sn_xS_4$ samples were investigated. Sn was found to have very high solubility in Cu_3SbS_4 and there was no second phase observed with Sn-doping up to 50 mol. %. Sn was more effective as a p-type dopant than Ge, and the carrier concentration was increased to 10^{21} cm^{-3} with 15 mol. % Sn-doping. The optimal carrier concentration for Cu_3SbS_4 was found to be around 5×10^{20} cm^{-3} and the zT value started to decline with higher carrier concentrations. Compared with Ge-doped Cu_3SbS_4, a similar zT value of 0.69 was obtained at 623 K for Sn-doped samples.

6.2 Experimental Details

Polycrystalline $Cu_3Sb_{1-x}Sn_xS_4$ samples with nominal Sn doping up to 50 mol. % were prepared by mechanical alloying (MA) combined with park plasma sintering (SPS) (FCT, Rauenstein, Germany). 15 g of starting elements of Cu (99.5 %, AlfaAesar), Sb (99.5 %, AlfaAesar), Sn (99.999 %, AlfaAesar), and S (reagent grade, Sigma-Aldrich) were ball milled with a powder to ball weight ratio of 1:20 in argon for 20 h. The obtained powders were loaded into a graphite die, and sintered using SPS at 723 K for 3 min under a pressure of 60 MPa.

6.3 Results and Discussions

Polycrystalline $Cu_3Sb_{1-x}Sn_xS_4$ ($x = 0 \sim 0.5$) bulk samples were examined using XRD and the results can be seen in Figure 6.1. All of the samples were phase pure and the peak shifted to a higher angle (Figure 6.1 left) with Sn-doping, as Sn has a smaller ionic radius than that of Sb. It suggests Sn has very high solubility in Cu_3SbS_4. Figure 6.2 shows the SEM images of $Cu_3Sb_{1-x}Sn_xS_4$ samples ($x = 0$, 0.1, 0.3 and 0.5). It can be seen that the fracture surfaces are slightly different for different samples. This is because some of the samples showed a more intergranular fracture while others showed a more transgranular fracture. Actually, all of the samples have similar microstructure with small and uniform grain size. There was no second phase observed for all samples, which was consistent with XRD results. And all of the samples have a relative density above 98 %.

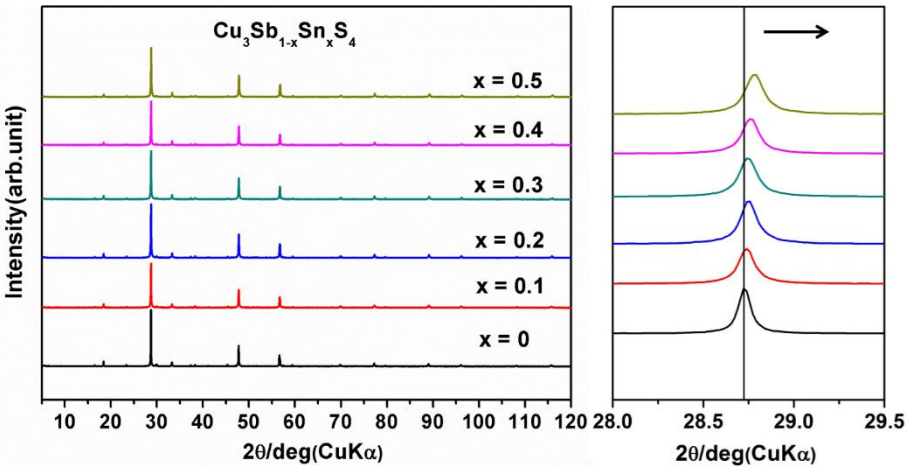

Figure 6.1: *(a) XRD patterns of $Cu_3Sb_{1-x}Sn_xS_4$ (x = 0 ~ 0.5) samples and (b) the enlarged figure shows the peak shift.*

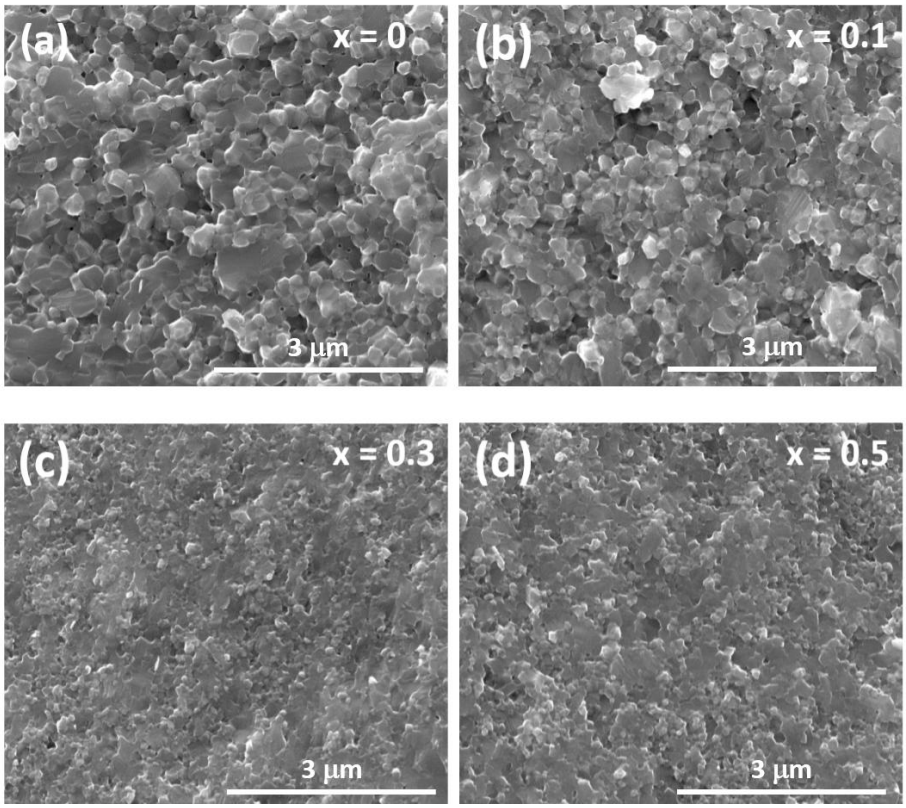

Figure 6.2: *SEM images of fracture surface for $Cu_3Sb_{1-x}Sn_xS_4$ (x = 0, 0.1, 0.3 and 0.5) samples.*

To investigate the oxidation states of elements and the compositions of $Cu_3Sb_{1-x}Sn_xS_4$ samples, X-ray photoelectron spectroscopy (XPS) was performed for the x=0, 0.1, 0.3 and 0.5 samples. A comparison of the survey spectrum is shown in Figure 6.3.

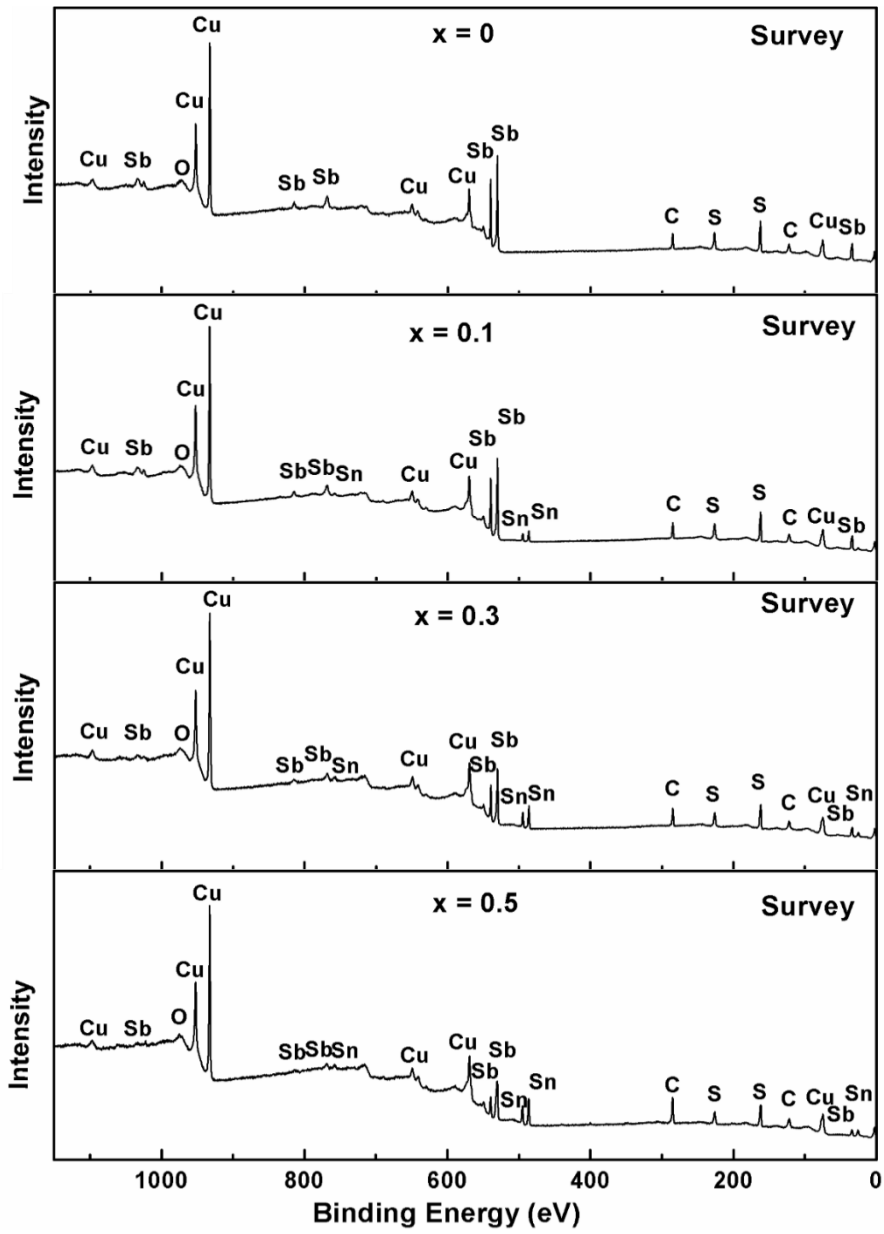

Figure 6.3: *X-ray photoelectron spectra (XPS) survey spectrum of $Cu_3Sb_{1-x}Sn_xS_4$ (x = 0, 0.1, 0.3 and 0.5) samples.*

Except for oxygen and carbon, the spectrums only show the peaks for copper, antimony, tin and sulfur. The presence of oxygen and carbon was because of the samples were exposed to air. The results further confirmed the composition and high purity of the samples. It also can be seen that, with increasing Sn-doping amount the peak intensity of Sb decreased and the peak intensity of Sn increased. This confirms that Sb was substituted by Sn, which is consistent with XRD results.

According to a simple valence counting, the Cu, Sb and S in Cu_3SbS_4 are expected to have oxidation state of +1, +5 and -2 respectively. To confirm the oxidation states of these elements, the high resolution XPS spectrum of Cu2p core level, Sb3d core level and S2p core level for Cu_3SbS_4 were analyzed as shown in Figure 6.4. All of the spectrums were calibrated using C1s with a binding energy of 284.8 eV. The black circle represents raw data, the blue line represents background and the red line represents peak fitting.

Cu2p shows well separated spin orbital components of $Cu2p_{1/2}$ and $Cu2p_{3/2}$. The $Cu2p_{1/2}$ and $Cu2p_{3/2}$ peaks were located at binding energies of 952.4 eV and 932.6 eV with a separation of 19.8 eV, which is consistent with Cu^+ [119-121], as expected for Cu_3SbS_4. Besides, there were no shake-up or satellite peaks around 942 eV which confirms the nonexistence of Cu^{2+} [122].

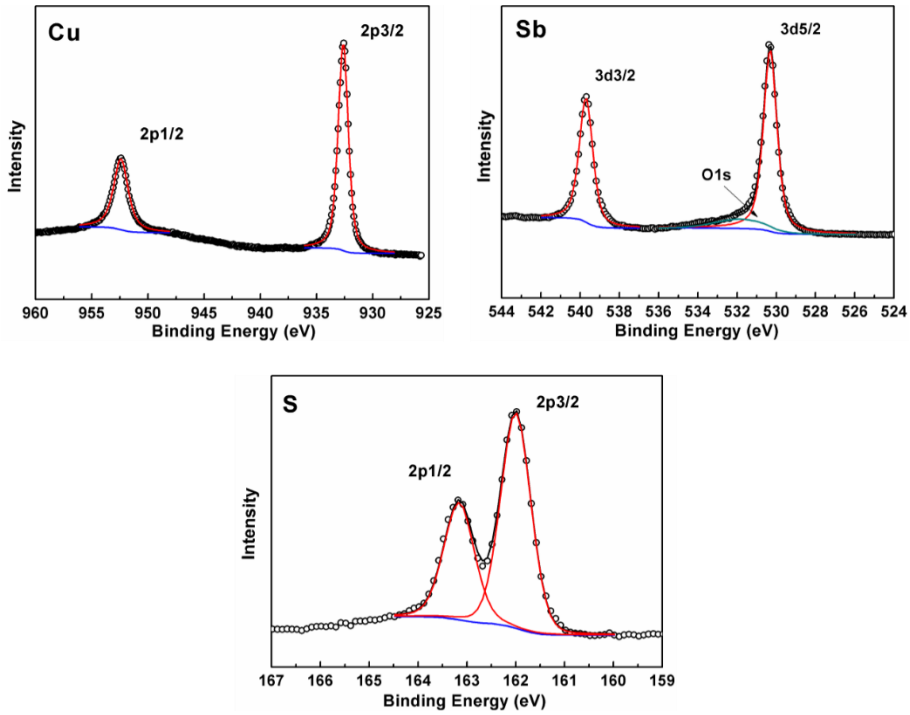

Figure 6.4: *X-ray photoelectron spectra (XPS) spectrum of Cu2p core level, Sb3d core level and S2p core level for Cu_3SbS_4 sample.*

Sb3d also shows well separated spin orbital components of $Sb3d_{3/2}$ and $Sb3d_{5/2}$. As $Sb3d_{5/2}$ overlaps with O1s [123], $Sb3d_{3/2}$ was used as a guide for peak fitting to minimize the effect of O1s. The $Sb3d_{3/2}$ and $Sb3d_{5/2}$ peaks are located at binding energies of 539.7 eV and 530.3 eV with a separation of 9.4 eV, which perfectly matches with Sb3d doublet (3d3/2 and 3d5/2) reported in the literature [124]. The binding energy of $Sb3d_{3/2}$ peak is very close to the reported value of 540 eV for Sb^{5+} [125], as expected for Cu_3SbS_4. To further confirm the oxidation state of Sb, the Sb3d core level of Cu_3SbS_4 was compared with that of $CuSbS_2$ which is expected to have Sb^{3+}. As seen in Figure 6.5, it is very clear that the binding energy of Sb3d for Cu_3SbS_4 is higher than that for $CuSbS_2$. As known, a higher positive oxidation state exhibit a higher binding energy due to the extra columbic

interaction between the photoemitted electron and the ion core. So the oxidation state of Sb in Cu_3SbS_4 is confirmed as +5.

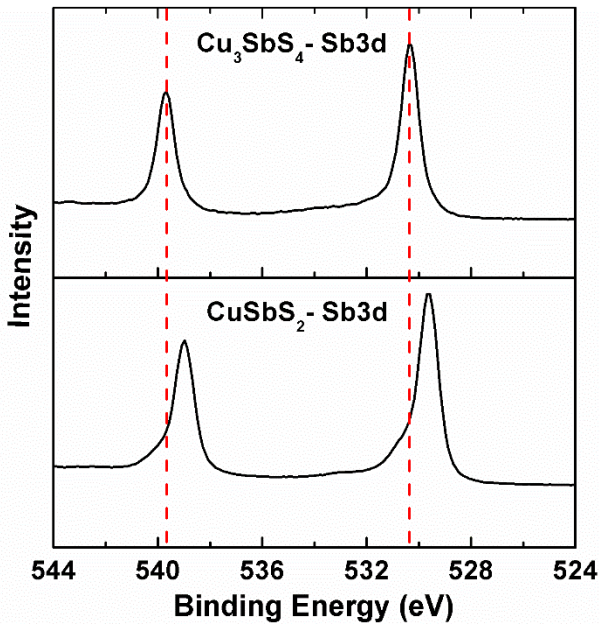

Figure 6.5: *X-ray photoelectron spectra (XPS) spectrum of Sb3d core level for Cu_3SbS_4 and $CuSbS_2$ samples.*

In terms of sulfur, the S2p peak has closely spaced spin-orbit components of $S2p_{1/2}$ and $S2p_{3/2}$. The $S2p_{1/2}$ and $S2p_{3/2}$ peaks are located at binding energies of 163.3 eV and 162.1 eV with a separation of 1.2 eV, which perfectly matches with the S2p doublet. The binding energies of the S2p peaks are consistent with those reported in metal sulfides when the oxidation state of sulfur is -2 [124]. Therefore, the oxidation states for this compound is $Cu_3^{1+}Sb^{5+}S_4^{2-}$. Figure 6.6 shows the comparison of XPS results for $Cu_3Sb_{1-x}Sn_xS_4$ (x = 0, 0.1, 0.3 and 0.5) samples. For the Cu2p core level, there is no obvious change in peak intensity, peak shape and binding energy with increasing Sn-doping amount as seen in

Figure 6.6 (a). This suggests that Sn-doping has no effect on Cu and all of the samples have Cu^{1+} oxidation state. With increasing Sn-doping, the intensity of the Sb3d peaks decrease while the intensity of the Sn3d peaks increase as Sb was substituted by Sn as seen in Figure 6.6 (b) and (c). The Sn3d shows well separated spin orbital components of $Sn3d_{3/2}$ and $Sn3d_{5/2}$. The $Sn3d_{3/2}$ and $Sn3d_{5/2}$ peaks are located at binding energies of 494.8 eV and 486.4eV with a separation of 8.4 eV, which perfectly matches the Sn3d doublet (3d3/2 and 3d5/2) [124]. The binding energy is consistent with the reported value for Sn^{4+} [122, 126]. For the Sb3d core level, the peak appears broadened due to the overlapping with the O1s core level and the decreased intensity of the Sb3d peaks. In fact, there is no change in Sb3d with increasing Sn-doping, except for the intensity. However, the S2p peaks showed very obvious peak broadening and the peaks slightly shifted to a lower binding energy, especially in the x = 0.5 sample. It is known that the exact binding energy of an electron depends not only on the core level and the oxidation state of the atom, but also on the local chemical and physical environment. As S is coordinated to both Cu and Sb in Cu_3SbS_4, substituting Sb with Sn will change the local chemical environment of S. Actually, the S2p peaks of the x = 0.5 sample could be fitted into two sets of $S2p_{1/2}$ and $S2p_{3/2}$ peaks (Figure 6.6 (d)), which can be regarded as the S-Sb bonds and S-Sn bonds. So the oxidation state of S in all Sn-doped samples was unchanged. Overall, the XPS results suggest that all of the $Cu_3Sb_{1-x}Sn_xS_4$ samples have high purity and there is no change in oxidation state of any element with Sn-doping.

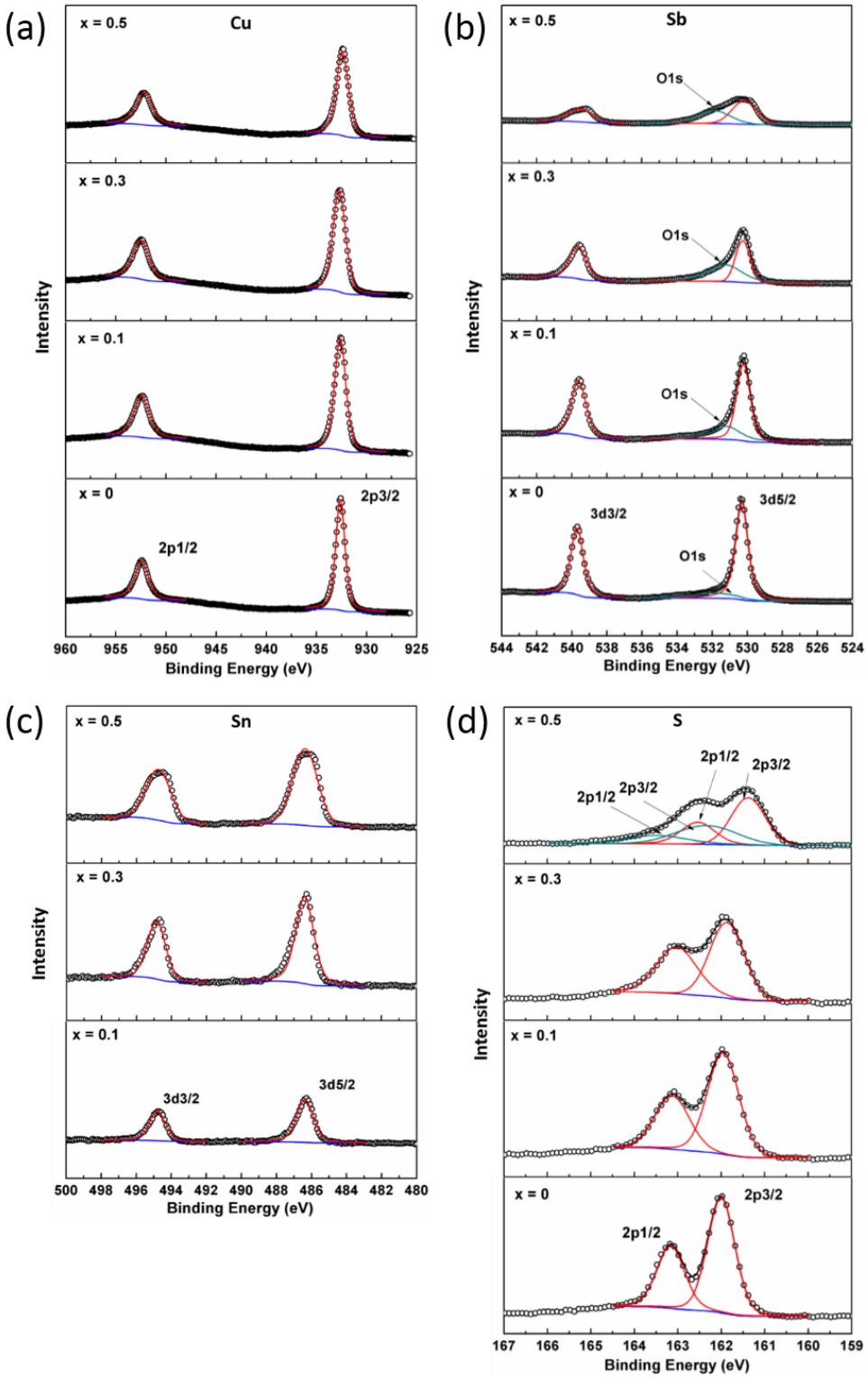

Figure 6.6: *X-ray photoelectron spectra (XPS) spectrum of (a) Cu2p, (b) Sb3d, (c) Sn3d and (d) S2p for $Cu_3Sb_{1-x}Sn_xS_4$ (x = 0, 0.1, 0.3 and 0.5) samples.*

The thermoelectric properties of $Cu_3Sb_{1-x}Sn_xS_4$ (x = 0 ~ 0.5) were investigated from 300 K to 573 K. Figure 6.7 shows the temperature dependence of electrical resistivity, Seebeck coefficient, and power factor. The electrical resistivity was significantly reduced by Sn doping over the investigated temperature range. The undoped sample showed semiconductor transport behavior, as its electrical resistivity decreased with increasing temperature. All of the Sn-doped samples showed metal-like transport behaviors, as their electrical resistivities increased with increasing temperature. Comparing with the Ge-doped samples, the 10 mol. % Sn-doped sample has a lower electrical resistivity than that of the 10 mol. % Ge-doped sample, which is 10.5 and 35.7 μΩm at 300 K, respectively. This suggests that Sn is more effective as a p-type dopant in Cu_3SbS_4. The Seebeck coefficient had a similar temperature dependence as the electrical resistivity for every sample. With increasing Sn-doping amount, the Seebeck coefficient decreased. For the x = 0.5 sample, it has a very low electrical resistivity of 3.2 μΩm but its Seebeck coefficient dropped to a value of 28.3 μVK^{-1} at 300 K. A maximum power factor of 1.35 $mWK^{-2}m^{-1}$ was achieved at 573 K for the x = 0.1 sample, which is higher than the maximum value of 1.08 $mWK^{-2}m^{-1}$ achieved with Ge-doping. The power factor started to drop when the Sn doping was higher than 10 mol. %, as the Seebeck coefficient was too low. This indicates a Sn-doping concentration of around 10 mol. % can realize an optimum carrier concentration to balance the resistivity and Seebeck coefficient in Cu_3SbS_4.

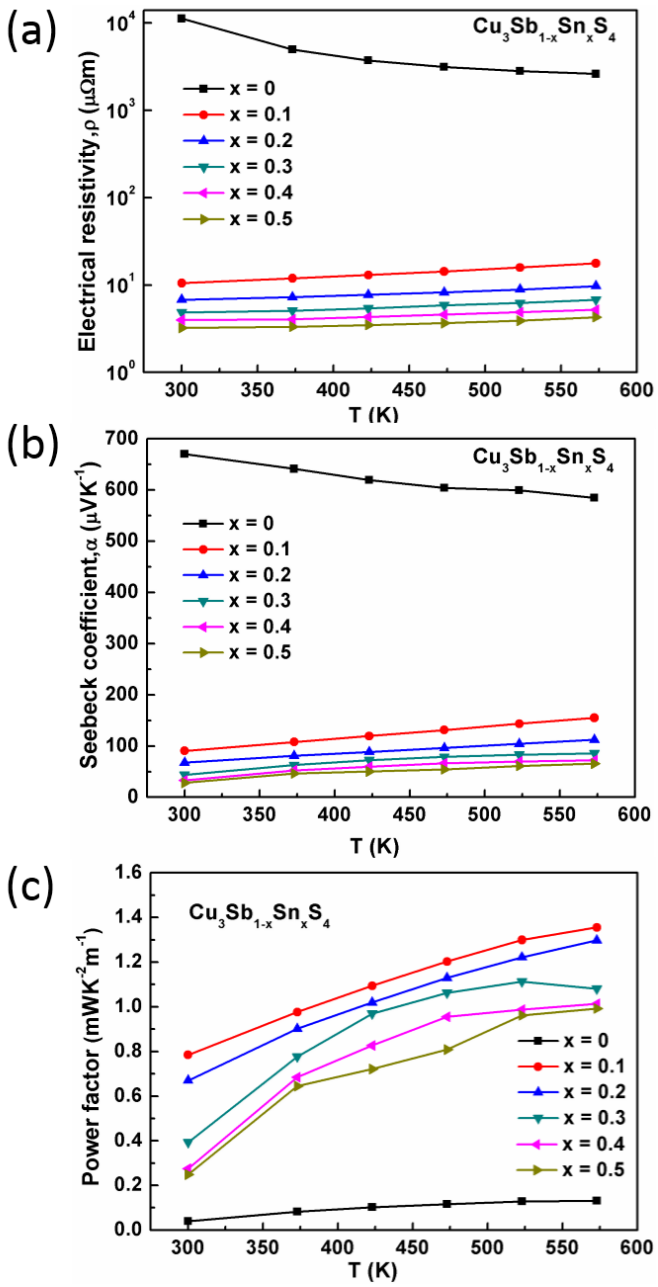

Figure 6.7 *The temperature dependence of (a) electrical resistivity, (b) Seebeck coefficient and (c) power factor for $Cu_3Sb_{1-x}Sn_xS_4$ (x = 0 ~ 0.5) samples. Note there is a 5 % uncertainty in all data points.*

The thermal transport properties of the $Cu_3Sb_{1-x}Sn_xS_4$ (x = 0 ~ 0.5) samples were investigated from 300 K to 573 K. Figure 6.8 (a) shows the temperature dependence of

the total thermal conductivities of all of the samples. The total thermal conductivity decreased with increasing temperature and there was no sign of bipolar effects. With increasing Sn doping, the thermal conductivity increased over the investigated temperature range due to the increased electronic contribution. The x = 0.5 sample has a thermal conductivity of 5.5 $Wm^{-1}K^{-1}$ at 300 K, which is about 3 times higher than that of the undoped sample. Figure 6.8 (b) shows the temperature dependence of the lattice thermal conductivity of the $Cu_3Sb_{1-x}Sn_xS_4$ samples. The lattice thermal conductivity (κ_L) was calculated by subtracting the electronic thermal conductivity (κ_e) from the total thermal conductivity, $\kappa_L = \kappa - \kappa_e$. The κ_e was estimated based on the Wiedemann-Franz law, $\kappa_e = LT/\rho$, where L is the Lorenz number. L was calculated based on the SPB model as discussed in last chapter, and the results are shown in Figure 6.8 (c). With increasing Sn doping amount, the lattice thermal conductivity increased. This is probably caused by the high lattice thermal conductivity of Cu_3SnS_4 (about 3.7 $Wm^{-1}K^{-1}$ at 300 K). It is very interesting that the Cu_3SnS_4 has such high lattice thermal conductivity as Sn is slightly lighter than Sb.

Figure 6.9 shows the temperature dependence of the *zT* value for the $Cu_3Sb_{1-x}Sn_xS_4$ (x = 0 ~ 0.5) samples. The *zT* value of all the samples increased linearly with increasing temperature. The thermoelectric performance of Cu_3SbS_4 was enhanced with Sn doping. A maximum *zT* value of about 0.52 was achieved at 573 K for the x = 0.1 sample. With higher amount of Sn-doping, the *zT* value started to drop due to a low Seebeck coefficient

and a high thermal conductivity. It indicates the optimal Sn-doping concentration for Cu_3SbS_4 is around or below 10 mol. %.

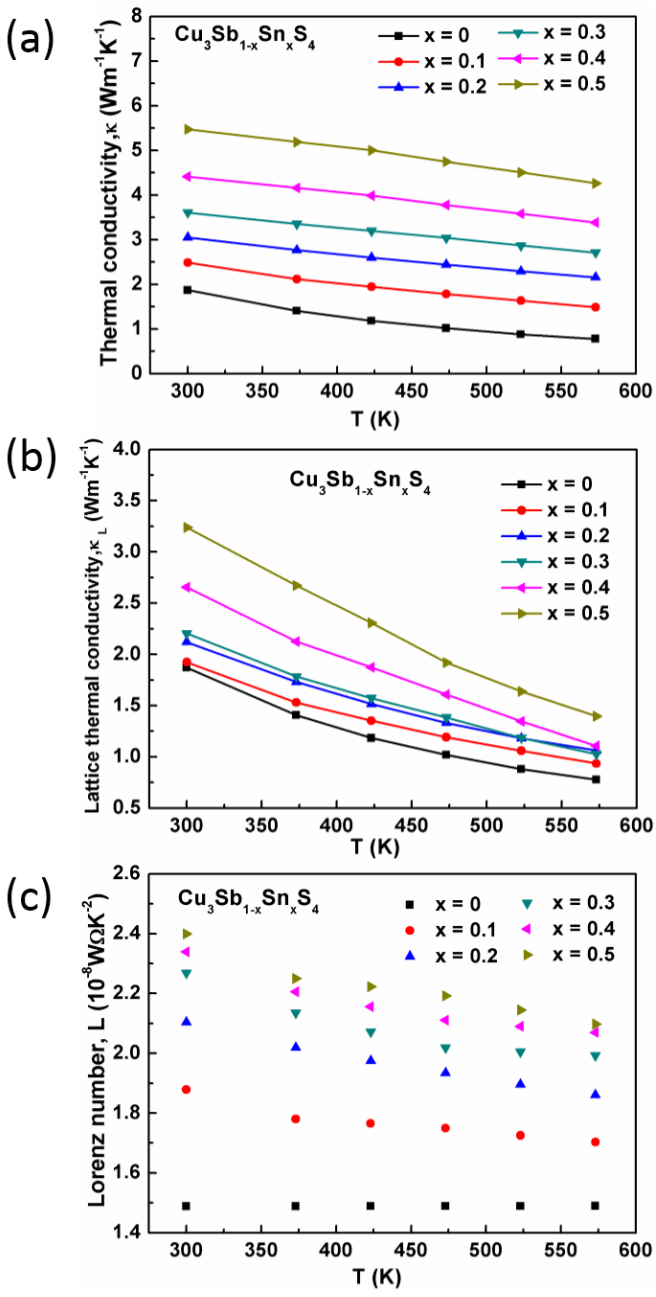

Figure 6.8 *The temperature dependence of (a) thermal conductivity, (b) lattice thermal conductivity and (c) calculated Lorenz number for $Cu_3Sb_{1-x}Ge_xS_4$ (x = 0 ~ 0.5) samples. Note there is a 10 % uncertainty in all data points.*

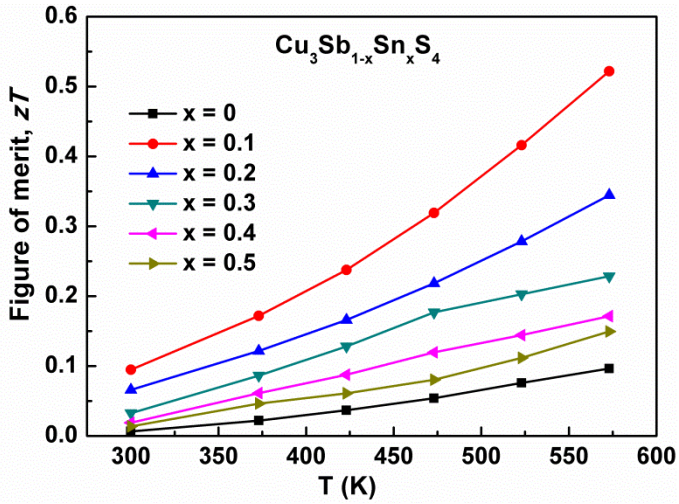

Figure 6.9 *The temperature dependence of the zT value for $Cu_3Sb_{1-x}Sn_xS_4$ (x = 0 ~ 0.5). Note there is a 20 % uncertainty in all data points.*

As discussed above, Sn is an effective p-type dopant for Cu_3SbS_4 and has a very high solubility on the Sb site. The results indicated that the optimal carrier concentration will be achieved with a Sn-doping concentration around or below 10 mol. %. Therefore, the Sn-doping concentration was fine-tuned and a new series samples of $Cu_3Sb_{1-x}Sn_xS_4$ (x = 0, 0.01, 0.03, 0.05, 0.10 and 0.15) were prepared. All of the samples have a relative density above 98 %. Figure 6.10 shows the XRD results, and all of the samples are phase pure. No obvious peak shift was observed as the doping concentration was low. SEM images of the fracture surface of the x = 0, 0.01, 0.05 and 0.15 samples are shown in Figure 6.11. All of the samples have similar microstructures and no second phase was observed. To show the distribution of each element in the Sn-doped samples, the samples were polished and analysed using EDX mapping in SEM. Figure 6.12 shows the results for the x = 0.15 sample, and the other samples produced similar results. It can be seen

that all the elements have homogenous distribution within the resolution of the technique.

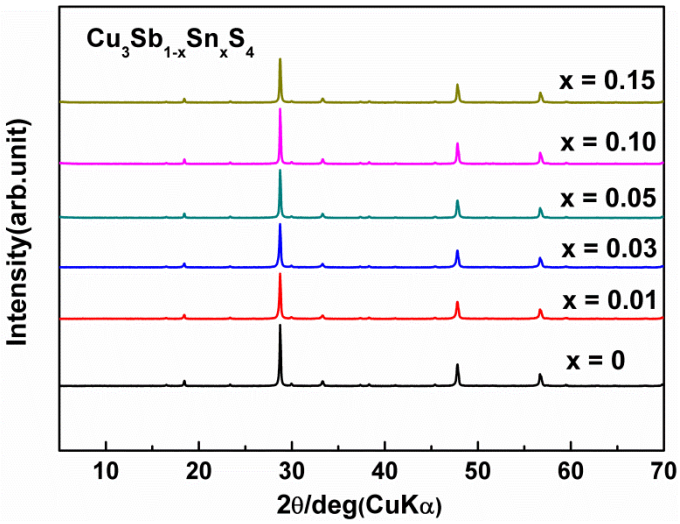

Figure 6.10: *XRD patterns of $Cu_3Sb_{1-x}Sn_xS_4$ (x = 0 ~ 0.15) samples.*

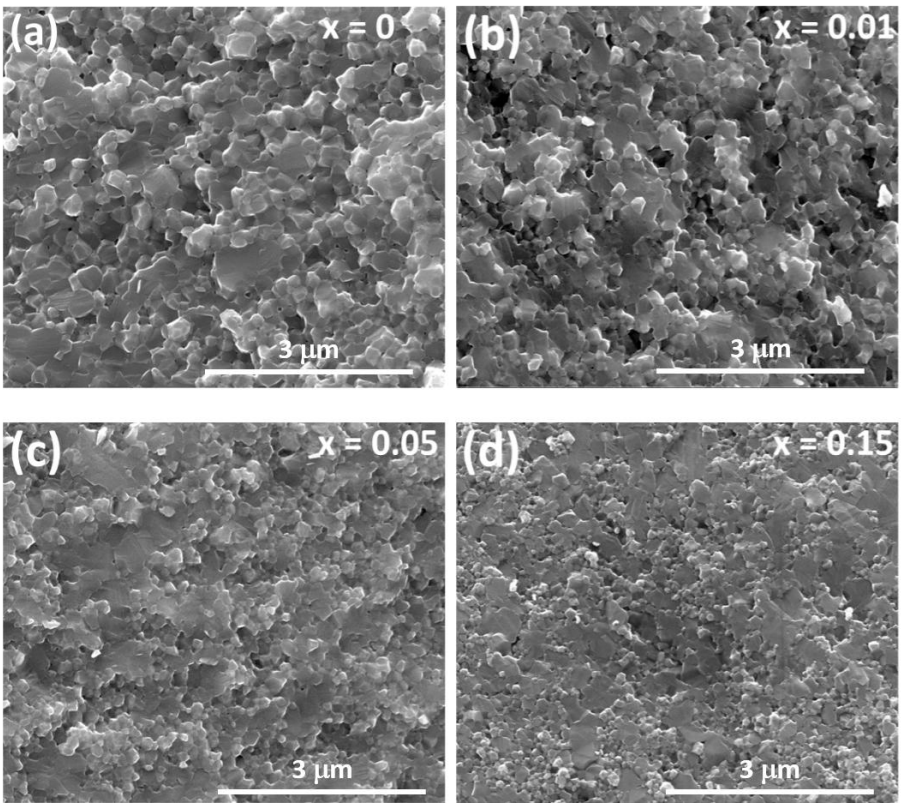

Figure 6.11: *SEM images for $Cu_3Sb_{1-x}Sn_xS_4$ (x = 0, 0.01, 0.05 and 0.15) samples.*

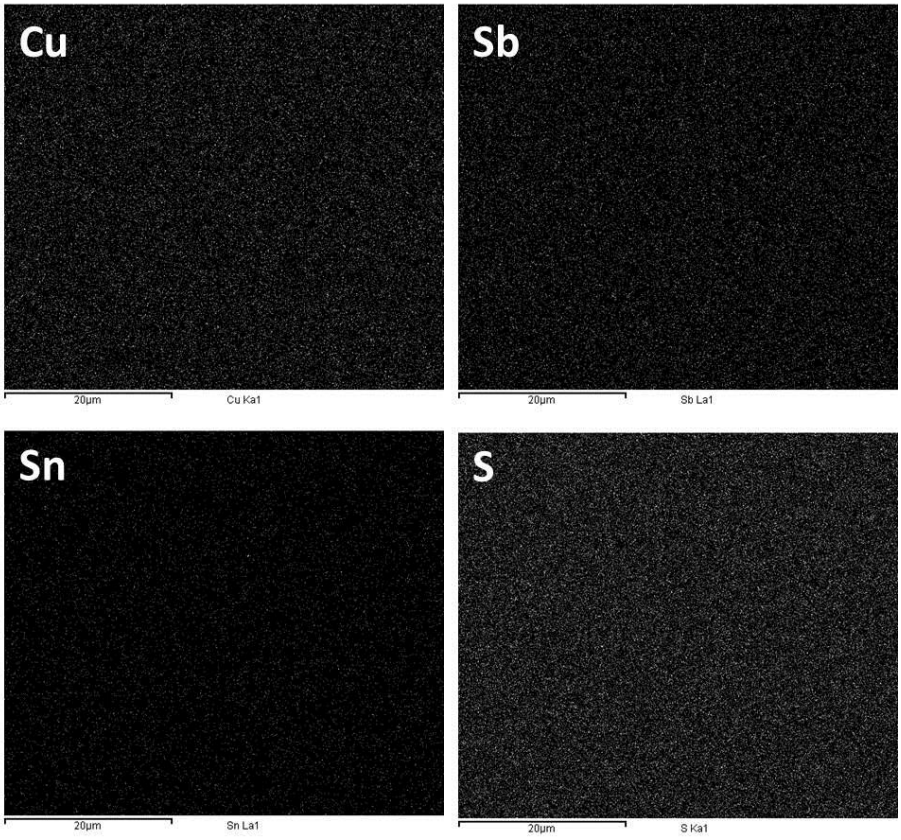

Figure 6.12: *EDX mapping for $Cu_3Sb_{1-x}Sn_xS_4$ (x = 0.15) sample.*

Table 6.1 shows the room temperature physical properties of the $Cu_3Sb_{1-x}Sn_xS_4$ (x = 0 ~ 0.15) samples. All of the samples have a positive Hall coefficients suggesting they are p-type semiconductors, which is consistent with their positive Seebeck coefficients. The undoped Cu_3SbS_4 is an intrinsic semiconductor with a carrier concentration of around 10^{17} cm^{-3}. With 15 mol. % Sn doping, the carrier concentration was increased up to 1.03 $\times 10^{21}$ cm^{-3}, which indicates Sn is an effective p-type dopant. Due to the increased carrier concentration, the electrical resistivity was largely reduced, while the Seebeck coefficient dropped. However, with increasing carrier concentration the uncertainty of Hall measurement increased up to 20%, which made the change of carrier mobility mainly

caused by error. The carrier concentration as a function of nominal doping content can be seen in Figure 6.13. The experimental results for Sn-doped samples show great agreement with the theoretical predictions (dashed line), assuming each Sn atom provides one hole in $Cu_3Sb_{1-x}Sn_xS_4$. It can be clearly seen that Sn is more effective than Ge as a p-type dopant.

Table 6.1 *Room temperature Hall coefficient, carrier concentration, carrier mobility, Seebeck coefficient and electrical resistivity of $Cu_3Sb_{1-x}Sn_xS_4$ ($x = 0 \sim 0.2$) samples.*

Nominal doping	Hall coefficient R_H (cm^3C^{-1})	Carrier concentration n (10^{20} cm^{-3})	Carrier mobility μ ($cm^2V^{-1}s^{-1}$)	Electrical resistivity ρ ($\mu\Omega m$)	Seebeck coefficient α (μVK^{-1})
$x = 0$	19	0.0032	16.4	11231.9	670.1
$x = 0.01$	0.080	0.78	5.9	150.3	264.2
$x = 0.03$	0.027	2.28	6.0	45.2	168.6
$x = 0.05$	0.015	4.07	5.7	23.3	125.8
$x = 0.10$	0.0093	6.70	7.6	10.5	90.6
$x = 0.15$	0.0061	10.25	6.8	7.6	71.8

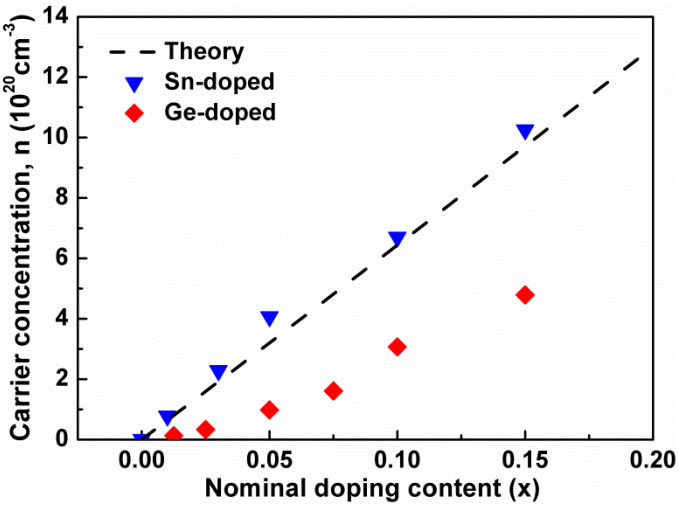

Figure 6.13: *The theoretical and experimental carrier concentration as a function of nominal Sn content.*

The electrical properties of the $Cu_3Sb_{1-x}Sn_xS_4$ (x = 0 ~ 0.15) samples were investigated from 300 K to 623 K. Figure 6.14 shows the temperature dependence of their electrical resistivity, Seebeck coefficient and power factor. The resistivity of Cu_3SbS_4 was reduced by 100 times with only 1 mol. % of Sn-doping. With increasing Sn-doping amount, the electrical resistivity decreased and the Seebeck coefficient dropped. A wide range of carrier concentration (10^{17} to 10^{21} cm^{-3}) was achieved in the Sn-doped samples, and a maximum power factor was obtained with carrier concentration of 6.7 × 10^{20} cm^{-3}. The transport properties were analysed using the SPB model as discussed in last chapter. The carrier concentration dependence of the Seebeck coefficient at 300 K is shown in Figure 6.15. The data for the Ge-doped samples is included for comparison. The solid line represents the Pisarenko line with m^* = 3.0 m_e. There is good agreement between the theoretical and experimental results. It indicates that the dopants have no obvious impact on the electronic structure as m^* is unchanged.

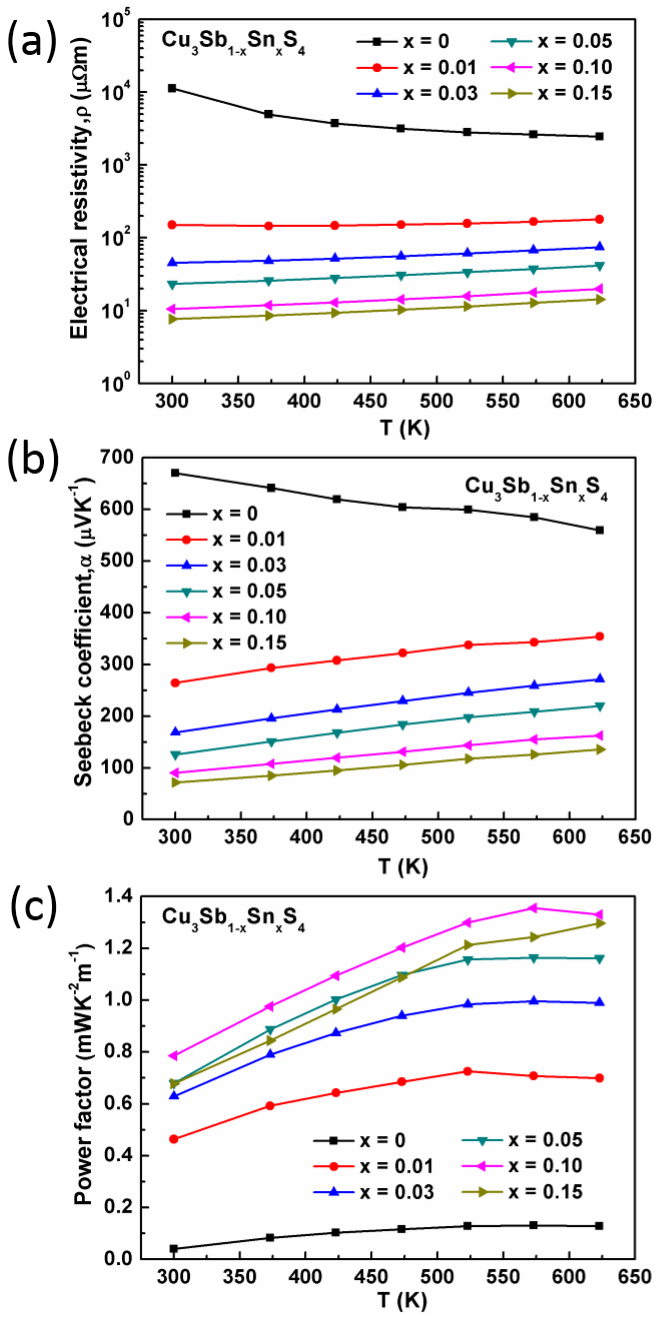

Figure 6.14 *The temperature dependence of (a) electrical resistivity, (b) Seebeck coefficient and (c) power factor for $Cu_3Sb_{1-x}Sn_xS_4$ (x = 0 ~ 0.15) samples. Note there is a 5 % uncertainty in all data points.*

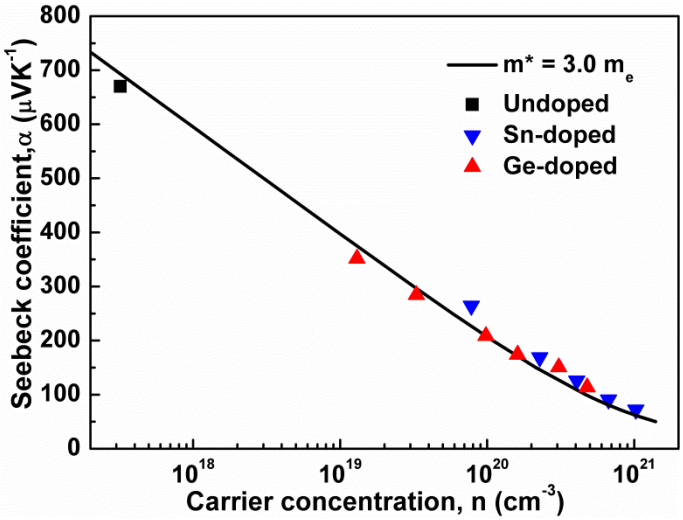

Figure 6.15 *The carrier concentration (n) dependence of Seebeck coefficient (α) at 300 K and the Pisarenko line with m* = 3.0 m_e.*

The thermal transport properties of the $Cu_3Sb_{1-x}Sn_xS_4$ (x = 0 ~ 0.15) samples were investigated from 300 K to 623 K. Figure 6.16 (a) shows the temperature dependence of thermal conductivities of all of the samples. The total thermal conductivity decreased with increasing temperature and there was no sign of bipolar effects. With increasing Sn doping, the thermal conductivity increased over the investigated temperature range due to the increased electronic contribution. Figure 6.16 (b) shows the temperature dependence of lattice thermal conductivity, which was calculated using the Lorenz numbers shown in Figure 6.16 (c). It can be seen that the lattice thermal conductivity slightly increased with increasing Sn-doping concentration and the increase for the x = 0.15 sample was more obvious. This is caused by the high lattice thermal conductivity of Cu_3SnS_4 as discussed in the previous section.

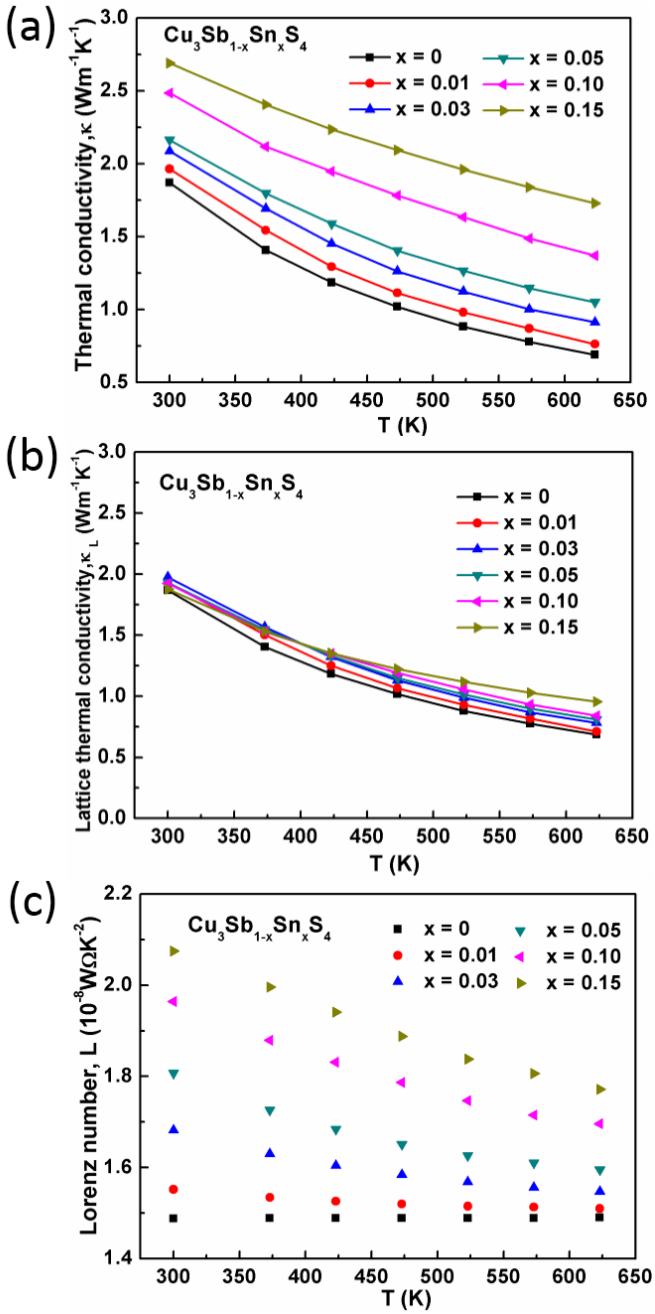

Figure 6.16 *The temperature dependence of (a) thermal conductivity, (b) lattice thermal conductivity and (c) calculated Lorenz number for $Cu_3Sb_{1-x}Sn_xS_4$ (x = 0 ~ 0.15) samples. Note there is a 10 % uncertainty in all data points.*

The temperature dependence of the *zT* value is shown in Figure 6.17. The *zT* value increased linearly with increasing temperature for all samples. All of the Sn-doped samples showed a higher *zT* value than the undoped sample, due to the improvement in electrical properties. A maximum *zT* value of 0.69 was obtained at 623 K for the x = 0.05 sample with a carrier concentration of 4.07×10^{20} cm^{-3}. This value is similar to the maximum *zT* value of 0.63 achieved in the Ge-doped sample (x = 0.1) with a carrier concentration of 4.79×10^{20} cm^{-3}. These results indicate the optimal carrier concentration for Cu_3SbS_4 is around 4×10^{20} cm^{-3}.

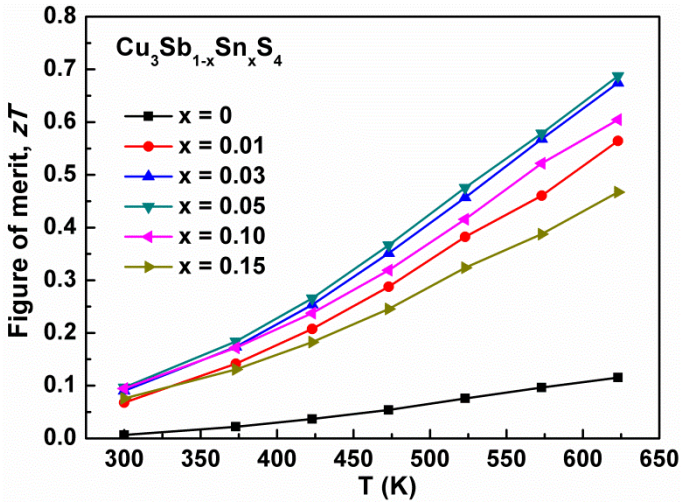

Figure 6.17 *The temperature dependence of the zT value for $Cu_3Sb_{1-x}Sn_xS_4$ (x = 0 ~ 0.15) samples. Note there is a 20 % uncertainty in all data points.*

An enhancement of the thermoelectric properties of Cu_3SbS_4 was achieved by tuning its carrier concentration. However, it could only improve the properties to some extent, due

to the strong interconnection between different parameters. A wide carrier concentration range was achieved in Cu_3SbS_4 through Sn-doping. Assuming the carrier concentration does not change with temperature, the power factor (PF), *zT* value, thermal conductivity (κ) and lattice thermal conductivity (κ_L) at 623 K was plotted as a function of carrier concentration as seen in Figure 6.18. With increasing carrier concentration, both the power factor and *zT* value first increased and then decreased. The power factor reached a maximum value at a carrier concentration of 6.7×10^{20} cm^{-3}. But the maximum *zT* value was obtained at a lower carrier concentration of 4.07×10^{20} cm^{-3}. This is because the linearly increased thermal conductivity starts to overlap with the improvement in the power factor when carrier concentration is higher than 4.07×10^{20} cm^{-3}. The thermal conductivity is comprised of the lattice contribution and electronic contribution. In Figure 6.18 (bottom), the difference between κ and κ_L is the electronic contribution. It can be seen that the increase of thermal conductivity was largely from the electronic contribution, and this was inevitable with increasing carrier concentration. However, a large portion of the thermal conductivity was still lattice contribution for all the samples. For $n = 6.7 \times 10^{20}$ cm^{-3} sample (x = 0.1), the ratio of lattice contribution to electronic contribution is about 1.6:1 and it has a very high power factor. It indicates the thermoelectric properties could be further improved, if the lattice thermal conductivity can be reduced while the high power factor can be maintained.

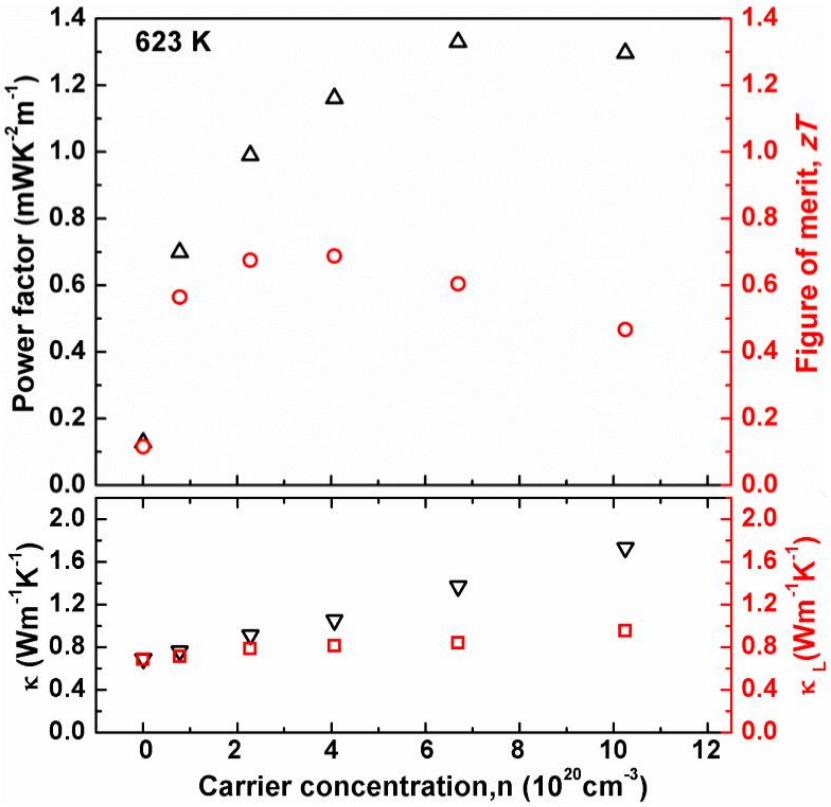

Figure 6.18 *The power factor, zT value and thermal conductivity as a function of carrier concentration for $Cu_3Sb_{1-x}Sn_xS_4$ (x = 0 ~ 0.15) samples.*

6.4 Conclusions

Polycrystalline Sn-doped $Cu_3Sb_{1-x}Sn_xS_4$ (x = 0 ~ 0.5) samples were prepared by mechanical alloying and spark plasma sintering. Sn had very high solubility in Cu_3SbS_4, and no second phase was found in samples with Sn doping up to 50 mol. %. The oxidation states of the elements in $Cu_3Sb_{1-x}Sn_xS_4$ were confirmed by XPS. Cu, Sb, Sn and S have oxidation state of +1, +5, +4 and -2 respectively, and there was no change in oxidation states with increasing Sn-doping. Sn was very effective as a p-type dopant. The carrier concentration increased up to 10^{21} cm^{-3} with 15 mol. % Sn-doping. A high power factor

of 1.33 $mWK^{-2}m^{-1}$ was achieved at 623 K for the x = 0.1 sample with carrier concentration of 6.7 × 10^{20} cm^{-3}. The transport properties were analysed by the single parabolic band (SPB) model, and a large effective mass of 3.0 m_e was estimated for all of the samples. A maximum *zT* value of 0.69 was obtained at 623 K for the x = 0.05 sample with a carrier concentration of 4.07 × 10^{20} cm^{-3}. Compared with Ge-doping, Sn-doping did not cause any formation of second phase and the Sn-doped samples showed a similar *zT* value. Besides, the carrier concentration dependence of the power factor, *zT* value and thermal conductivity indicates there is space for further improvement in thermoelectric properties of Cu_3SbS_4.

Chapter 7 Thermoelectric Properties of $Cu_3SbS_{4(1-y)}Se_{4y}$ Solid Solution

7.1 Introduction

In the last two chapters, the effects of Ge-doping and Sn-doping on the thermoelectric properties of Cu_3SbS_4 have been investigated. The thermoelectric performance of Cu_3SbS_4 was significantly improved by optimizing the electrical properties. The electronic thermal conductivity increased with optimized electrical properties, but the total thermal conductivity was still mainly comprised of the lattice thermal conductivity. This indicates that the thermoelectric performance of Cu_3SbS_4 could be further improved if the lattice thermal conductivity could be reduced without affecting the electrical properties. It is known that the formation of a solid solution between two similar compounds can introduce alloying scattering due to differences in atomic mass and size between the components. The alloying scattering scatters phonons to a larger extent than electrons, which is well suited for thermoelectric materials [127]. As known, Se and S are near each other on the periodic table, and they have similar atomic radius, similar electronegativity and the same valence. Also Cu_3SbS_4 and Cu_3SbSe_4 have the same crystal structure. This suggests that Cu_3SbS_4 and Cu_3SbSe_4 should form a complete solid solution. Therefore, the phase structure, microstructure and thermoelectric properties of $Cu_3SbS_{4(1-y)}Se_{4y}$ solid solution were investigated in this chapter. Sn was used as a p-type dopant to achieve a high power factor.

7.2 Experimental Details

$Cu_3SbS_{4(1-y)}Se_{4y}$ solid-solutions (y = 0, 0.05, 0.1, 0.2, 0.3, 0.4 and 0.5) were prepared by mechanical alloying (MA) combined with spark plasma sintering (SPS) (FCT, Rauenstein, Germany). 15g of starting elements of Cu (99.5 %, AlfaAesar), Sb (99.5 %, AlfaAesar), Se (99.99 %, AlfaAesar), and S (reagent grade, Sigma-Aldrich) were ball milled with a powder to ball weight ratio of 1:20 in argon for 20 h. The obtained powders were loaded into a graphite die, and sintered using SPS at 723 K for 3 min under a pressure of 60 MPa.

7.3 Results and Discussions

$Cu_3SbS_{4(1-y)}Se_{4y}$ bulk samples were examined by XRD and the results can be seen in Figure 7.1. The XRD patterns of all of the samples match the reference data for Cu_3SbS_4 (PDF: 00-035-0581), which suggests the samples are phase pure. From the enlarged figure, it can be seen that the peak shift to low angle with increasing Se amount as Se has a larger ionic radius than that of S. According to Vegard's law [128], the lattice parameter of a solid solution of two constituents is approximately equal to a mixtures of the two constituents' lattice parameters as shown in the following equation,

$$a_{\mathrm{A}_{1-x}\mathrm{B}_x} = (1-x)a_{\mathrm{A}} + xa_{\mathrm{B}}$$

Where, $a_{\mathrm{A}_{1-x}\mathrm{B}_x}$ is the lattice parameter of the solution, a_{A} and a_{B} are the lattice parameters of the pure constituents, and x is the molar fraction of B in the solution. To confirm the formation of solid solution, the lattice parameters of all samples were calculated based on XRD results by using FullProf software. The results are shown in

Figure 7.2. The calculated lattice parameter of Cu_3SbS_4 is $a = b = 5.382$ Å and $c = 10.752$ Å, which is consistent with other reports [90, 129]. The dashed line represents Vegard's relation and the lattice parameter of Cu_3SbSe_4 was taken as the reported value of $a = b = 5.685$ Å and $c = 11.258$ Å [127]. It can be seen the lattice parameters of the solid solutions are in good agreement with Vegard's law, which suggests Cu_3SbS_4 and Cu_3SbSe_4 form a complete solid solution.

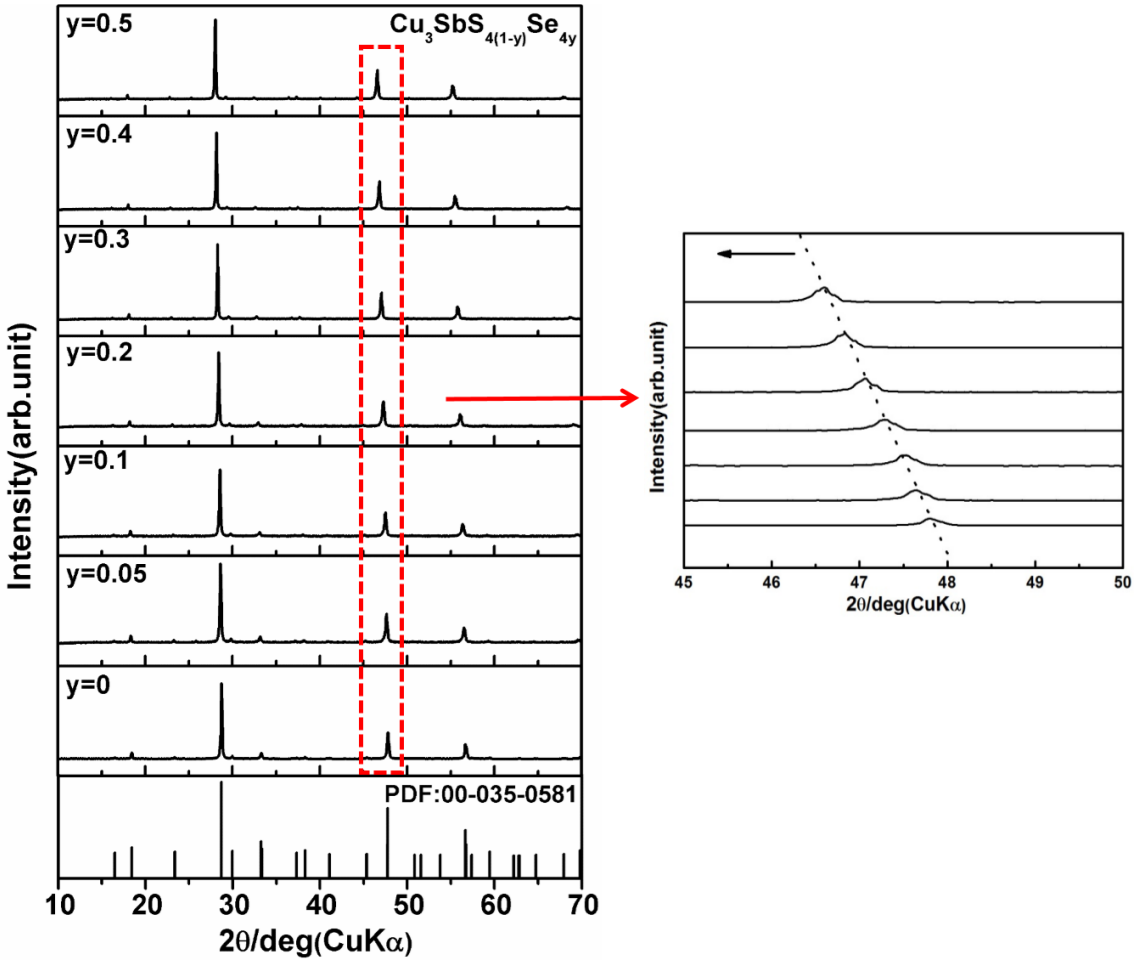

Figure 7.1: *XRD patterns of $Cu_3SbS_{4(1-y)}Se_{4y}$ ($y = 0 \sim 0.5$) samples and the enlarged figure showing peak shift.*

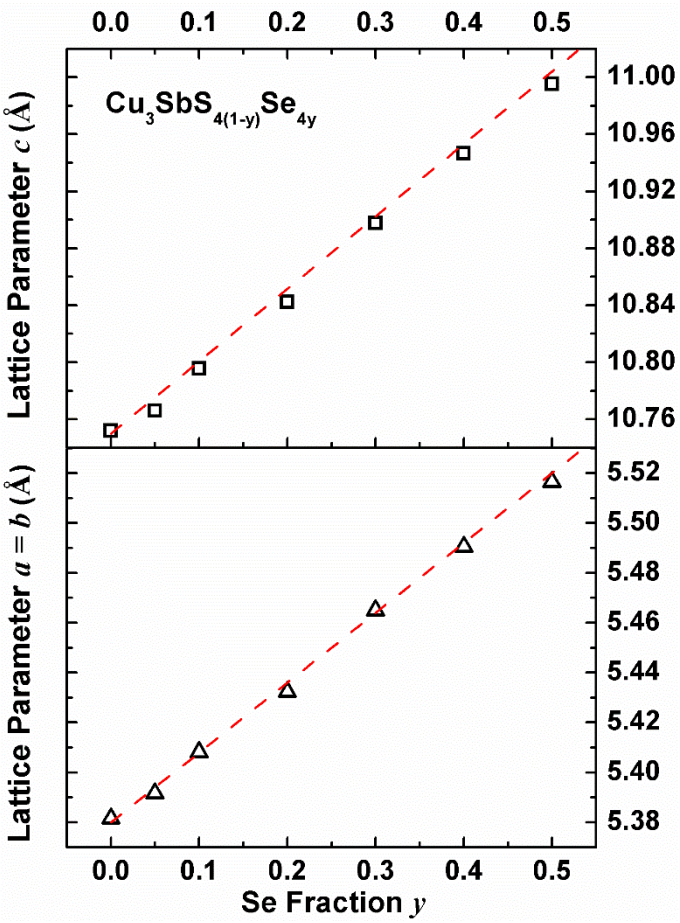

Figure 7.2: *Calculated lattice parameters of $Cu_3SbS_{4(1-y)}Se_{4y}$ (y = 0 ~ 0.5) samples and the red dash line represents the Vegard's law.*

The fracture surfaces of $Cu_3SbS_{4(1-y)}Se_{4y}$ (y = 0, 0.05, 0.1 and 0.2) bulk samples were observed using SEM as shown in Figure 7.3. The pure Cu_3SbS_4 sample has a very uniform microstructure with grain size of 100 ~ 300 nm. The y = 0.05 sample has a similar microstructure as pure Cu_3SbS_4 sample. However, there was grain growth in both the y = 0.1 and y = 0.2 samples, which indicates Cu_3SbSe_4 tends to form larger grains than Cu_3SbS_4.

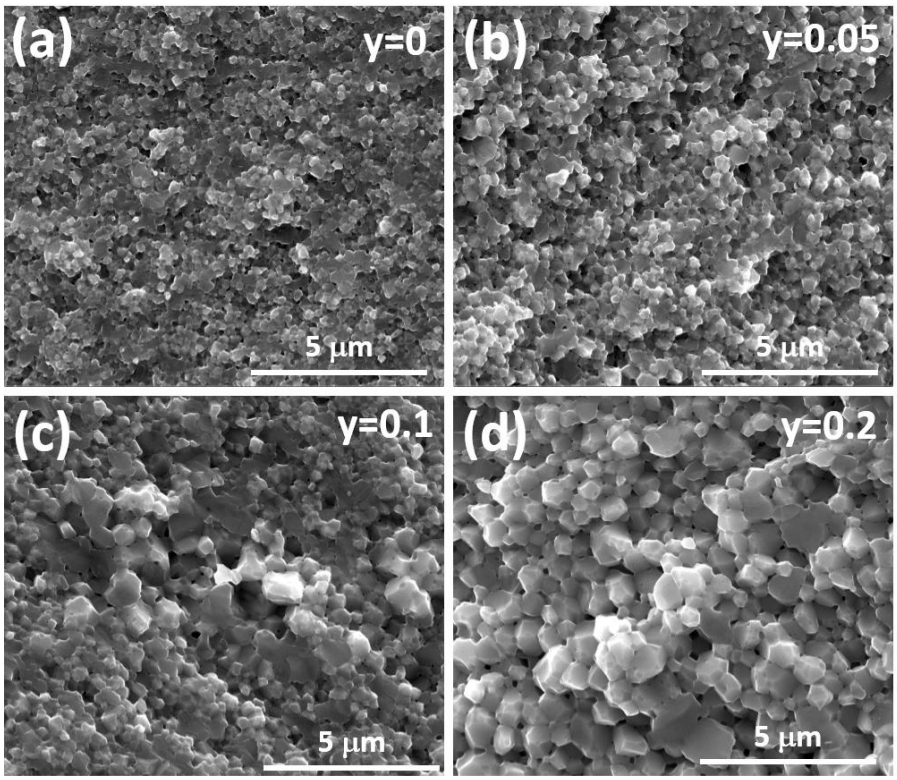

Figure 7.3: *SEM images of $Cu_3SbS_{4(1-y)}Se_{4y}$ (y = 0, 0.05, 0.1 and 0.2) samples.*

Some regions with very large grains were observed in the y = 0.2 sample, which can be seen in Figure 7.4 (a) and (b). The sample does not seem to be very uniform as the small grain regions should be S-rich while the large grain regions should be Se-rich. Figure 7.4 (c), (d) and (e) show higher magnification images of the large grain regions, which have grain size of 1 ~ 3 μm. This is about 10 times larger than the grain size of pure Cu_3SbS_4. Figure 7.4 (f) shows an SEM image of a pure Cu_3SbSe_4 sample reported by Wei et.al [99], which also shows large grains. The sample was prepared using a similar method as in this work. It suggests Cu_3SbSe_4 was forming much larger grains than that of Cu_3SbS_4 and the large grain regions in y = 0.2 sample were Se-rich. The reason of the formation of large

grains in Cu_3SbSe_4 is because Se has lower ionization energy and is more reactive than S, which leads to greater diffusion rates of Se compared to S during SPS sintering.

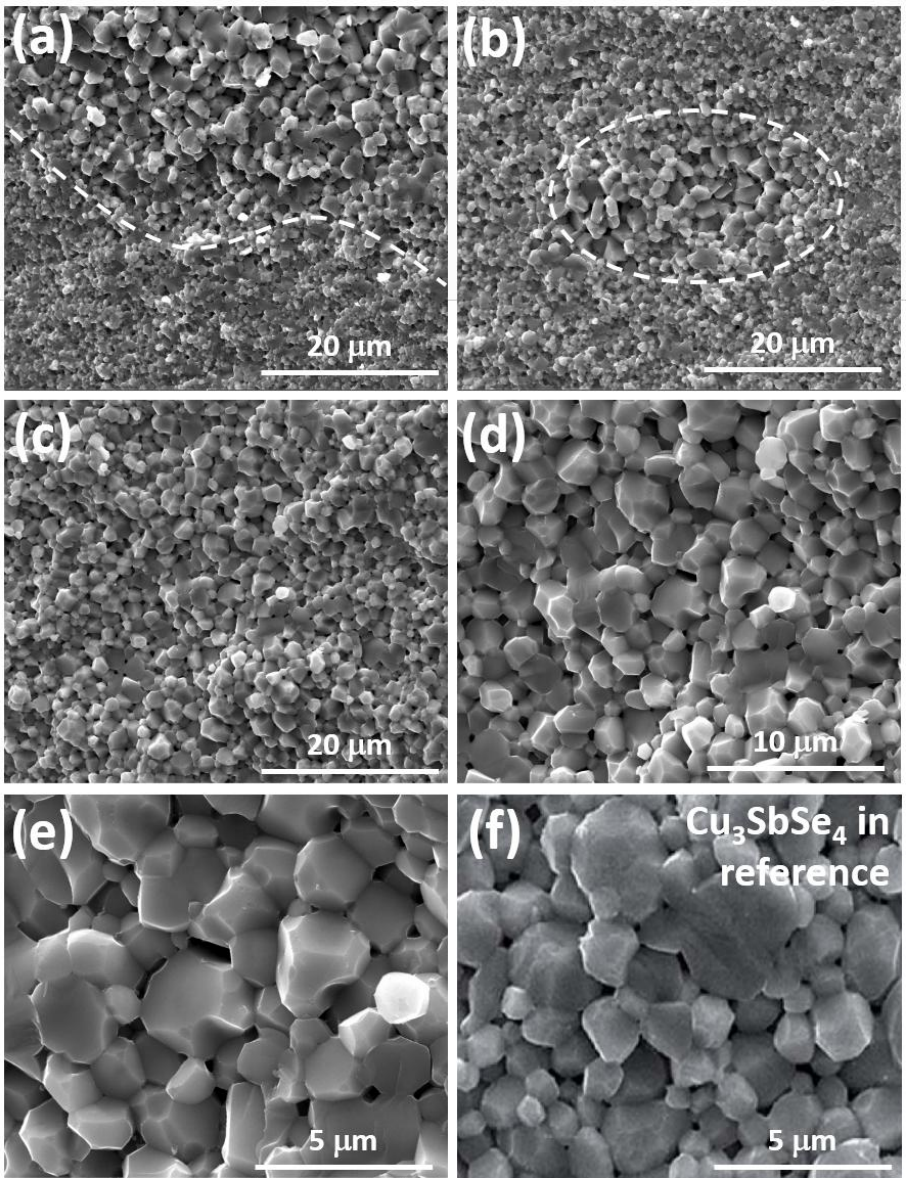

Figure 7.4: *(a) ~ (e) SEM images of $Cu_3SbS_{4(1-y)}Se_{4y}$ (y = 0.2) samples and (f) SEM image of Cu_3SbSe_4 from reference [99].*

The thermal transport properties of $Cu_3SbS_{4(1-y)}Se_{4y}$ (y = 0 ~ 0.5) samples were investigated from 300 K to 623 K. Figure 7.5 shows the temperature dependence of the thermal conductivity for all of the samples. As all of the samples have very high electrical resistivity, the electronic thermal conductivity was negligible and the total thermal conductivity can be regarded as the lattice thermal conductivity. The thermal conductivity decreased with increasing temperature for all of the samples. With increasing Se amount, the thermal conductivity first decreased and then increased. The y = 0.1 sample has the lowest thermal conductivity. Compared with pure Cu_3SbS_4 sample, the thermal conductivity of y = 0.1 sample was reduced. The decrease in thermal conductivity can be attributed to the alloying scattering produced by local mass-contrast and atomic defects in solid solution. However, grain growth can produce an increase in lattice thermal conductivity as there will be less grain boundaries. Therefore, the thermal conductivity was not further reduced with increasing Se content.

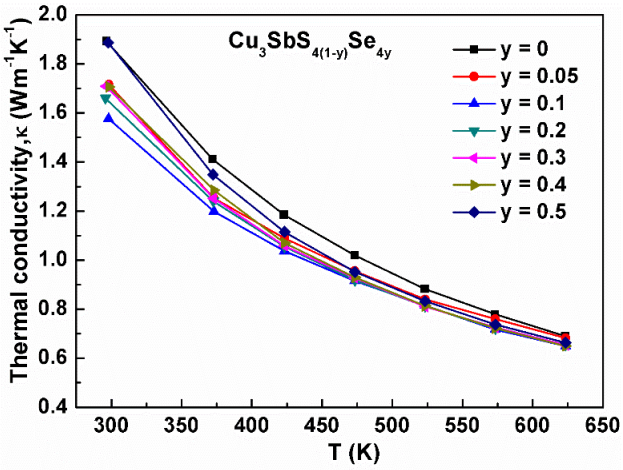

Figure 7.5: *The temperature dependence of thermal conductivity for $Cu_3SbS_{4(1-y)}Se_{4y}$ (y = 0 ~ 0.5) samples. Note there is a 10 % uncertainty in all data points.*

As the $Cu_3SbS_{4(1-y)}Se_{4y}$ (y = 0.1) sample has the lowest thermal conductivity, it was doped with 10 mol. % of Sn to improve the power factor as a highest power factor was achieved with 10 mol.% Sn in Cu_3SbS_4 sample. The effects of solid solution on electrical properties were investigated. Four samples were presented in the following study, which are $Cu_3Sb_{1-x}Sn_xS_{4(1-y)}Se_{4y}$ samples of A (x = 0, y = 0), B (x = 0, y = 0.1), C (x = 0.1, y = 0) and D (x = 0.1, y = 0.1). The temperature dependence of the electrical resistivity, Seebeck coefficient and power factor is shown in Figure 7.6. The Sn-doped samples (x = 0.1) have much lower electrical resistivity than the undoped samples (x = 0), as expected from the results in the last chapter. Also it can be seen that the introduction of Se has no obvious effect on the electrical resistivity for both doped and undoped samples. However, the Seebeck coefficient dropped in samples with Se substitution (B and D), which can be seen in Figure 7.6 (b). It is probably caused by the effect of Se on the band structure of Cu_3SbS_4, as the S3p orbitals contribute to the valence band maximum (VBM). The substitution of S by Se will affect the effective mass of the valence bands. The reported effective mass of Cu_3SbSe_4 was 1.5 m_e [99], which is smaller than the effective mass of Cu_3SbS_4 (3.0 m_e) found in this work. The change of effective mass will affect the Seebeck coefficient. Due to the decrease in Seebeck coefficient, the power factor also dropped in samples with Se substitution as shown in Figure 7.6 (c). It was unexpected that Se would have such a significant impact on the electrical properties of Cu_3SbS_4. The *zT* value was not further improved in $Cu_3SbS_{4(1-y)}Se_{4y}$ solid solution, which can be seen in Figure 7.6 (d). The results suggest the lattice thermal conductivity of Cu_3SbS_4 can be reduced with alloying

scattering, but its electronic structure is sensitive to substitution on the S site.

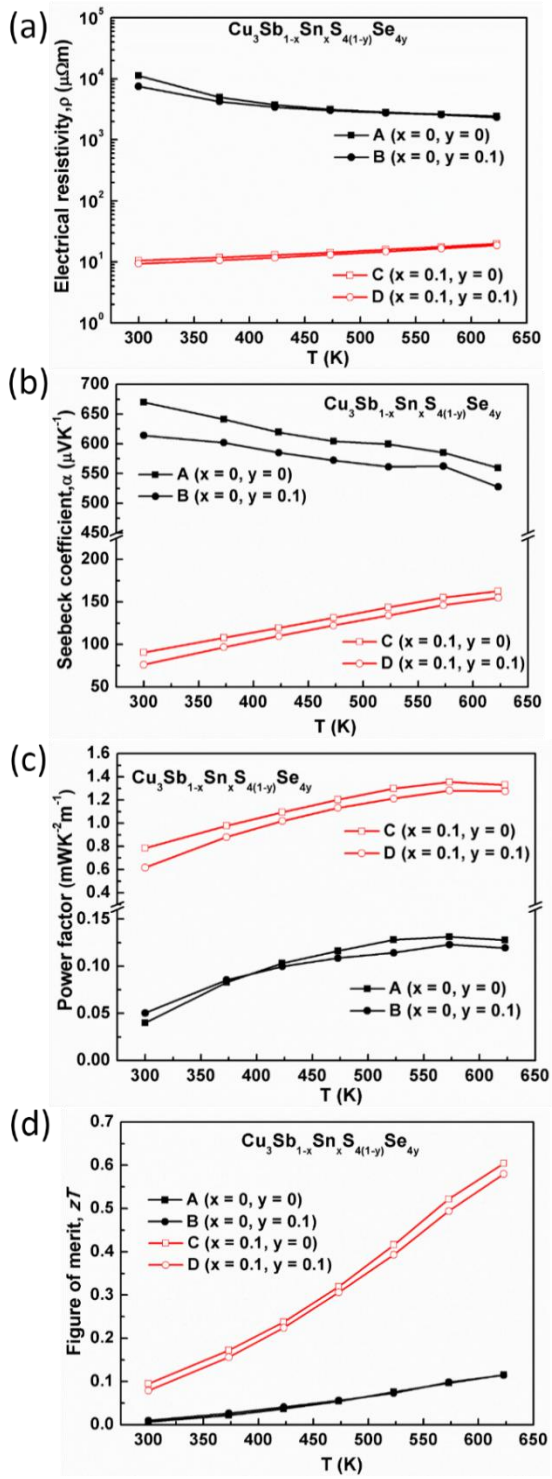

Figure 7.6: *The temperature dependence of (a) electrical resistivity, (b) Seebeck coefficient, (c) power factor and (d) zT value for sample A, B, C and D. Note there is a 20 % uncertainty in zT values and a 5 % uncertainty in all other data points.*

Considering all of the results for substituted Cu_3SbS_4, substituting Sb might avoid disturbing the electronic structure of Cu_3SbS_4 as the VBM is composed of a hybridization between the Cu3d orbitals and the S3p orbitals. According to the rules of solid solution, Bi and As could form a solid solution in Cu_3SbS_4. Therefore, $Cu_3Sb_{1-x}Bi_xS_4$ (x = 0, 0.05, 0.1, 0.2 and 0.3) samples were prepared and the XRD results are shown in Figure 7.7. Unfortunately, Bi was found to have very low solubility in Cu_3SbS_4, which was lower than 5 mol. %, and a second phase of $Cu_4Bi_4S_9$ was formed. This was probably because the ionic radius of Bi (76 pm) is much larger than that of Sb (60 pm), and it was not able to fit easily into the crystal structure of Cu_3SbS_4. Besides, it is interesting that the second phase was $Cu_4Bi_4S_9$ instead of Cu_3BiS_4. It indicates Cu_3BiS_4 might have different crystal structure from Cu_3SbS_4 and need strict conditions to form. In terms of As, it was reported forming a solid solution with Cu_3SbS_4 [130], but it was not studied in this work due to its high toxicity.

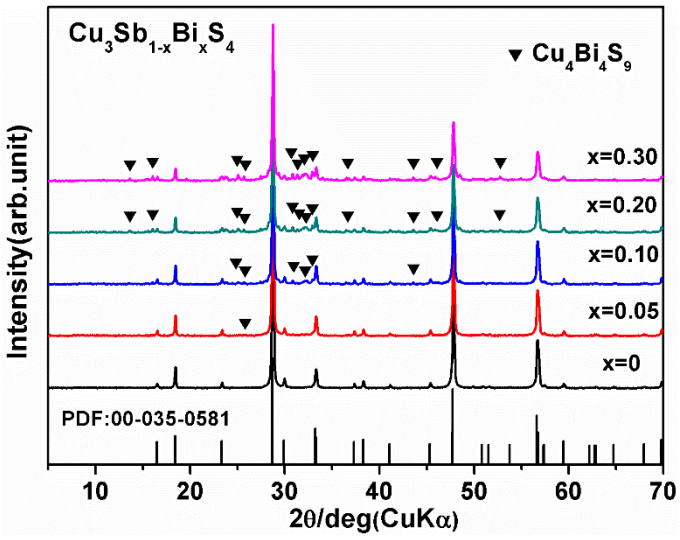

Figure 7.7: *XRD patterns of $Cu_3Sb_{1-x}Bi_xS_4$ (x = 0 ~ 0.3) samples.*

7.4 Conclusions

Polycrystalline $Cu_3SbS_{4(1-y)}Se_{4y}$ (y = 0 ~ 0.5) solid solutions were prepared by mechanical alloying and spark plasma sintering. All of the samples were phase pure and the XRD peaks shifted to low angle as Se has larger ionic radius than S. The calculated lattice parameters of all of the samples showed good agreement with Vergard's law indicating a solid solution was formed. Se caused grain growth in solid solutions. Due to alloying scattering, the lattice thermal conductivity was reduced. The y = 0.1 sample showed the lowest thermal conductivity, and the thermal conductivity was not further reduced with higher Se content due to the grain growth. The electrical properties of the y = 0.1 sample was investigated. The results indicated Se had no obvious impact on electrical resistivity but it affects the Seebeck coefficient. It was believed that the band structure of Cu_3SbS_4 was disturbed by substituting S with Se, as S contributes to the VBM. The decrease of Seebeck produced a decrease in the power factor and there was no further improvement in the *zT* value of the $Cu_3SbS_{3.6}Se_{0.4}$ solid solution. The attempt to substitute Sb with Bi to form a solid solution failed, because of the large difference of ionic radius between Sb and Bi.

Chapter 8 Conclusions and Future Work

8.1 Conclusions

In this work, the synthesis and thermoelectric properties of Cu-Sb-S compounds were investigated. The effects of synthesis methods on microstructure and thermal transport properties were studied based on Cu_3SbS_4 compound. Two different synthesis processing routes of melt processing combined with spark plasma sintering (SPS) and mechanical alloying (MA) combined with SPS were compared. It was found that the MA + SPS processing route was more suitable for S-containing compounds and it can produce very fine microstructures. The small grains of 100 ~ 300 nm introduced more phonon scattering (more grain boundaries) and led to a much lower thermal conductivity in Cu_3SbS_4.

The all four Cu-Sb-S compounds of $Cu_{12}Sb_4S_{13}$, $CuSbS_2$, Cu_3SbS_3 and Cu_3SbS_4 were prepared by MA + SPS and all samples had high purity and high density. The lone-pair electrons of Sb and the [CuS3] plane play important roles in realizing very low lattice thermal conductivity. The lattice thermal conductivities of $Cu_{12}Sb_4S_{13}$, $CuSbS_2$ and Cu_3SbS_4 were governed by Umklapp phonon scattering and a T^{-1} dependence was observed for these samples. A phase transition at 398 K was found in Cu_3SbS_3, which is similar to that in Cu_3SbSe_3. The phase transition will cause mechanical problems, which

makes it unsuitable for application, in spite of its extremely low thermal conductivity (lower than 0.35 $Wm^{-1}K^{-1}$). Except for $Cu_{12}Sb_4S_{13}$, which is known to be a good thermoelectric material, the other three compounds showed very poor thermoelectric performance due to their high electrical resistivities. Attempts to optimize electrical properties of $CuSbS_2$ were failed, which made this research more focused on Cu_3SbS_4 compound.

The effects of Ge-doping and Sn-doping on microstructure, electronic structure and thermoelectric properties of Cu_3SbS_4 were investigated. Ge was found to partially form a second phase of Cu_2GeS_3, but it still worked as an effective p-type dopant, which increased the carrier concentration up to 4.79×10^{20} cm^{-3}. The transport properties were analysed by the single parabolic band (SPB) model, and a large effective mass of 3.0 m_e was estimated for Cu_3SbS_4. This large m^* was derived from the three degenerate bands at VBM in the calculated band structure. Ge doping slightly shifted the Fermi level, without altering the electronic structure of Cu_3SbS_4. The thermal conductivity was dominated by Umklapp phonon scattering for all of the samples. The second phase of Cu_2GeS_3 had no obvious effect on the transport properties. A maximum zT value of 0.63 was obtained at 673 K in Cu_3SbS_4 samples with 10 mol. % and 15 mol. % Ge doping. In comparison, Sn had very high solubility in Cu_3SbS_4, and no second phase was found in samples with Sn doping up to 50 mol. %. Also the oxidation states of the elements in $Cu_3Sb_{1-x}Sn_xS_4$ were confirmed by XPS. Cu, Sb, Sn and S have oxidation states of +1, +5,

+4 and -2 respectively and there was no change in oxidation states with increasing Sn-doping. Sn was more effective as a p-type dopant than Ge. The carrier concentration increased up to 10^{21} cm^{-3} with 15 mol. % Sn-doping. A high power factor of 1.33 $mWK^{-2}m^{-1}$ was achieved at 623 K for the x = 0.1 sample with a carrier concentration of 6.7 × 10^{20} cm^{-3}. The transport properties were analysed using the single parabolic band (SPB) model, and an effective mass of 3.0 m_e was estimated for all of the samples, which is consistent with Ge-doped samples. A maximum zT value of 0.69 was obtained at 623 K for the x = 0.05 sample, which is similar with that of Ge-doped sample. For both Ge-doped and Sn-dpoed samples, the best thermoelectric performance was achieved with similar carrier concentration of 4 ~ 5 × 10^{20} cm^{-3}. This suggests that the optimal carrier concentration of high zT value for Cu_3SbS_4 is in this range. It was also found that the thermal conductivity was largely comprised of lattice contribution, even with a high carrier concentration. This indicates that the thermoelectric performance of Cu_3SbS_4 could be further improved by reducing lattice thermal conductivity.

Aiming to reduce the lattice thermal conductivity, the solid solutions of $Cu_3SbS_{4(1-y)}Se_{4y}$ (y = 0 ~ 0.5) were prepared by MA + SPS. The phase structure, microstructure and thermoelectric properties were investigated. All of the samples were phase pure and the XRD peaks shifted to low angle as Se has a larger ionic radius than S. The calculated lattice parameters of all of the samples showed good agreement with Vergard's law, indicating a solid solution was formed. Se caused grain growth in solid solutions, as it

was more reactive than S. Due to alloying scattering, the lattice thermal conductivity was reduced. The y = 0.1 sample showed the lowest thermal conductivity, and the thermal conductivity was not further reduced with increasing Se content due to the grain growth. The electrical properties of the y = 0.1 sample was investigated. The results indicated that Se has no obvious impact on electrical resistivity, but it reduced the Seebeck coefficient. It was believed that the band structure of Cu_3SbS_4 was disturbed by substituting S with Se, as S contributes to the VBM. The decrease of Seebeck produced a decrease in the power factor and there was no further improvement in the *zT* value of the $Cu_3SbS_{4(1-y)}Se_{4y}$ solid solution. The attempt to substitute Sb with Bi to form a solid solution failed, because of the large difference of ionic radius between Sb and Bi.

8.2 Future Work

8.2.1 $CuSbS_2$

$CuSbS_2$ has a very low thermal conductivity and very high Seebeck coefficient, but its high electrical resistivity leads to very poor thermoelectric performance. Although the attempts to optimize its electrical properties failed in this work, there might be other dopants that will work in $CuSbS_2$. A comprehensive study of its crystal structure and band structure could help to identify better dopants. The solubility of the dopants might be increased by optimizing the synthesis route or using other synthesis routes.

8.2.2 Cu_3SbS_4

The thermoelectric properties of Cu_3SbS_4 were significantly improved through optimization of carrier concentration and a maximum *zT* value of 0.69 was obtained at 623 K. This value is high in terms of sulfides, but it has not reached the benchmark *zT* of 1.0 for thermoelectric materials. As Cu_3SbS_4 has the advantage of low-toxicity, earth abundance and low-cost, it is promising in thermoelectric application if the *zT* could be further improved. Therefore, it is useful to found a suitable technique for Cu_3SbS_4 to reduce its lattice thermal conductivity without sacrificing its electrical properties. Except for alloying scattering, other techniques such as nano-participants, nano-composites and all-scale hierarchical scattering could be used in Cu_3SbS_4.

8.2.3 Other Sulfides

Thermoelectric sulfides are attracting more and more attention due to its low-cost and low-toxicity. The main challenge in sulfides is to improve their thermoelectric performance. Except for further improvement of the well-known sulfides, it is worth to search more sulfides as potential thermoelectric materials. Related to this work, the families of Cu-Sn-S and Cu-Bi-S compounds might contain some new potential thermoelectric sulfides. Moreover, Sn and Bi are more environmental-friendly than Sb.

List of Publications

1. Khaliq, J., C. Li, **K. Chen**, B. Shi, H. Ye, A.M. Grande, H. Yan, and M.J. Reece, *Reduced thermal conductivity by nanoscale intergrowths in perovskite like layered structure La2Ti2O7.* Journal of Applied Physics, 2015. **117**(7): p. 075101.
2. Williams, H.R., R.M. Ambrosi, **K. Chen**, U. Friedman, H. Ning, M.J. Reece, M.C. Robbins, K. Simpson, and K. Stephenson, *Spark plasma sintered bismuth telluride-based thermoelectric materials incorporating dispersed boron carbide.* Journal of Alloys and Compounds, 2015. **626**: p. 368-374.
3. Du, B., **K. Chen**, H. Yan, and M.J. Reece, *Efficacy of lone-pair electrons to engender ultralow thermal conductivity*. Scripta Materialia, 2016. 111: p. 49-53.
4. Cui, S., C. Boussard-plédel, L. Calvez, F. Rojas, **K. Chen**, H. Ning, M.J. Reece, T. Guizouarn, and B. Bureau, *Comprehensive study of tellurium based glass ceramics for thermoelectric application.* Advances in Applied Ceramics, 2015. **114**(sup1): p. S42-S47.
5. **Chen, K.**, B. Du, N. Bonini, C. Weber, H. Yan, and M.J. Reece, *Theory-guided synthesis of an eco-friendly and low-cost copper-based sulfide thermoelectric material*. Journal of Physic Chemistry C, 2016.

References

1. *Renewables 2015 Global Status Report.* 2015. http://www.ren21.net/status-of-renewables/global-status-report/

2. Heremans, J.P., *The Ugly Duckling.* Nature, 2014. **508**(7496): p. 327-328.

3. Xie, W.J., J. He, H.J. Kang, X.F. Tang, S. Zhu, M. Laver, S.Y. Wang, J.R.D. Copley, C.M. Brown, Q.J. Zhang, and T.M. Tritt, *Identifying the Specific Nanostructures Responsible for the High Thermoelectric Performance of $(Bi,Sb)_2Te_3$ Nanocomposites.* Nano Letters, 2010. **10**(9): p. 3283-3289.

4. Xiong, Z., X.H. Chen, X.Y. Huang, S.Q. Bai, and L.D. Chen, *High Thermoelectric Performance of $Yb_{0.26}Co_4Sb_{12}$/yGaSb Nanocomposites Originating from Scattering Electrons of Low Energy.* Acta Materialia, 2010. **58**(11): p. 3995-4002.

5. Biswas, K., J. He, I.D. Blum, C.I. Wu, T.P. Hogan, D.N. Seidman, V.P. Dravid, and M.G. Kanatzidis, *High-Performance Bulk Thermoelectrics with All-Scale Hierarchical Architectures.* Nature, 2012. **489**(7416): p. 414-8.

6. Wang, H., J.-F. Li, M. Zou, and T. Sui, *Synthesis and Transport Property of $AgSbTe_2$ as a Promising Thermoelectric Compound.* Applied Physics Letters, 2008. **93**(20): p. 202106.

7. Hsu, K.F., S. Loo, F. Guo, W. Chen, J.S. Dyck, C. Uher, T. Hogan, E.K. Polychroniadis, and M.G. Kanatzidis, *Cubic $AgPb_mSbTe_{2+m}$: Bulk Thermoelectric Materials with High Figure of Merit.* Science, 2004. **303**(5659): p. 818-21.

8. Wang, X.W., H. Lee, Y.C. Lan, G.H. Zhu, G. Joshi, D.Z. Wang, J. Yang, A.J. Muto, M.Y. Tang, J. Klatsky, S. Song, M.S. Dresselhaus, G. Chen, and Z.F. Ren, *Enhanced Thermoelectric Figure of Merit in Nanostructured n-type Silicon Germanium Bulk Alloy.* Applied Physics Letters, 2008. **93**(19): p. 193121.

9. Yang, S.H., T.J. Zhu, T. Sun, J. He, S.N. Zhang, and X.B. Zhao, *Nanostructures in high-performance $(GeTe)_x(AgSbTe_2)_{100-x}$ Thermoelectric Materials.* Nanotechnology, 2008. **19**(24): p. 245707.

10. Zhao, L.D., S.H. Lo, Y.S. Zhang, H. Sun, G.J. Tan, C. Uher, C. Wolverton, V.P. Dravid, and M.G. Kanatzidis, *Ultralow Thermal Conductivity and High Thermoelectric Figure of Merit in SnSe Crystals.* Nature, 2014. **508**(7496): p. 373.

11. Amatya, R. and R.J. Ram, *Trend for Thermoelectric Materials and Their Earth Abundance.* Journal of Electronic Materials, 2011. **41**(6): p. 1011-1019.

12. He, Y., T. Day, T. Zhang, H. Liu, X. Shi, L. Chen, and G.J. Snyder, *High Thermoelectric Performance in Non-toxic Earth-abundant Copper Sulfide.* Adv Mater, 2014. **26**(23): p. 3974-8.

13. Allgaier, R.S. and W.W. Scanlon, *Mobility of Electrons and Holes in PbS, PbSe, and PbTe between Room Temperature and 4.2K.* Physical Review, 1958. **111**(4): p. 1029-1037.

14. Haynes, W.M., *CRC Handbook of Chemistry and Physics, 93rd Edition*. 2012: Taylor & Francis.

15. Lu, X., D.T. Morelli, Y. Xia, F. Zhou, V. Ozolins, H. Chi, X. Zhou, and C. Uher, *High Performance Thermoelectricity in Earth-Abundant Compounds Based on Natural*

Mineral Tetrahedrites. Advanced Energy Materials, 2013. **3**(3): p. 342-348.

16. Skoug, E.J. and D.T. Morelli, *Role of Lone-Pair Electrons in Producing Minimum Thermal Conductivity in Nitrogen-Group Chalcogenide Compounds.* Physical Review Letters, 2011. **107**(23).

17. Heo, J., G. Laurita, S. Muir, M.A. Subramanian, and D.A. Keszler, *Enhanced Thermoelectric Performance of Synthetic Tetrahedrites.* Chemistry of Materials, 2014. **26**(6): p. 2047-2051.

18. Rowe, D.M., *CRC Handbook of Thermoelectrics*. 1995: CRC Press.

19. Paul, D., *Thermoelectric Energy Harvesting. ICT - Energy - Concepts Towards Zero - Power Information and Communication Technology.* 2014: InTech

20. Sootsman, J.R., D.Y. Chung, and M.G. Kanatzidis, *New and Old Concepts in Thermoelectric Materials.* Angew Chem Int Ed Engl, 2009. **48**(46): p. 8616-39.

21. Shakouri, A., *Recent Developments in Semiconductor Thermoelectric Physics and Materials.* Annual Review of Materials Research, 2011. **41**(1): p. 399-431.

22. Tritt, T.M. and M.A. Subramanian, *Thermoelectric Materials, Phenomena, and Applications: A Bird's Eye View.* Mrs Bulletin, 2006. **31**(3): p. 188-194.

23. Heremans, J.P., B. Wiendlocha, and A.M. Chamoire, *Resonant Levels in Bulk Thermoelectric Semiconductors.* Energy & Environmental Science, 2012. **5**(2): p. 5510.

24. Jaworski, C.M., B. Wiendlocha, V. Jovovic, and J.P. Heremans, *Combining Alloy Scattering of Phonons and Resonant Electronic Levels to Reach a High Thermoelectric Figure of Merit in PbTeSe and PbTeS alloys.* Energy & Environmental Science, 2011.

4(10): p. 4155-4162.

25. Ohtaki, M., D. Ogura, K. Eguchi, and H. Arai, *High-Temperature Thermoelectric Properties of In_2O_3-Based Mixed Oxides and Their Applicability to Thermoelectric-Power Generation.* Journal of Materials Chemistry, 1994. **4**(5): p. 653-656.

26. Ko, D.K., Y. Kang, and C.B. Murray, *Enhanced Thermopower via Carrier Energy Filtering in Solution-processable Pt-Sb_2Te_3 Nanocomposites.* Nano Lett, 2011. **11**(7): p. 2841-4.

27. Pei, Y., X. Shi, A. LaLonde, H. Wang, L. Chen, and G.J. Snyder, *Convergence of Electronic Bands for High Performance Bulk Thermoelectrics.* Nature, 2011. **473**(7345): p. 66-9.

28. Toberer, E.S., A. Zevalkink, and G.J. Snyder, *Phonon Engineering Through Crystal Chemistry.* Journal of Materials Chemistry, 2011. **21**(40): p. 15843.

29. Vineis, C.J., A. Shakouri, A. Majumdar, and M.G. Kanatzidis, *Nanostructured Thermoelectrics: Big Efficiency Gains from Small Features.* Adv Mater, 2010. **22**(36): p. 3970-80.

30. Wu, F., H.Z. Song, F. Gao, W.Y. Shi, J.F. Jia, and X. Hu, *Effects of Different Morphologies of Bi_2Te_3 Nanopowders on Thermoelectric Properties.* Journal of Electronic Materials, 2013. **42**(6): p. 1140-1145.

31. Xie, W.J., X.F. Tang, Y.G. Yan, Q.J. Zhang, and T.M. Tritt, *Unique Nanostructures and Enhanced Thermoelectric Performance of Melt-Spun BiSbTe Alloys.* Applied Physics Letters, 2009. **94**(10).

32. Cook, B.A., M.J. Kramer, J.L. Harringa, M.K. Han, D.Y. Chung, and M.G. Kanatzidis, *Analysis of Nanostructuring in High Figure-of-Merit $Ag_{1-x}Pb_mSbTe_{2+m}$ Thermoelectric Materials.* Advanced Functional Materials, 2009. **19**(8): p. 1254-1259.

33. Heremans, J.P., V. Jovovic, E.S. Toberer, A. Saramat, K. Kurosaki, A. Charoenphakdee, S. Yamanaka, and G.J. Snyder, *Enhancement of Thermoelectric Efficiency in PbTe by Distortion of the Electronic Density of States.* Science, 2008. **321**(5888): p. 554-7.

34. Joshi, G., H. Lee, Y. Lan, X. Wang, G. Zhu, D. Wang, R.W. Gould, D.C. Cuff, M.Y. Tang, M.S. Dresselhaus, G. Chen, and Z. Ren, *Enhanced Thermoelectric Figure-of-Merit in Nanostructured p-type Silicon Germanium Bulk Alloys.* Nano Lett, 2008. **8**(12): p. 4670-4674.

35. Basu, R., S. Bhattacharya, R. Bhatt, M. Roy, S. Ahmad, A. Singh, M. Navaneethan, Y. Hayakawa, D.K. Aswal, and S.K. Gupta, *Improved Thermoelectric Performance of Hot Pressed Nanostructured n-type SiGe Bulk Alloys.* Journal of Materials Chemistry A, 2014. **2**(19): p. 6922-6930.

36. Liu, H.L., X. Shi, F.F. Xu, L.L. Zhang, W.Q. Zhang, L.D. Chen, Q. Li, C. Uher, T. Day, and G.J. Snyder, *Copper Ion Liquid-like Thermoelectrics.* Nature Materials, 2012. **11**(5): p. 422-425.

37. D. J. Chakrabarti , D.E.L., *The Cu-S (Copper-Sulfur) System.* Bulletin of Alloy Phase Diagrams, 1983. **4**(3).

38. Dennler, G., R. Chmielowski, S. Jacob, F. Capet, P. Roussel, S. Zastrow, K. Nielsch,

I. Opahle, and G.K.H. Madsen, *Are Binary Copper Sulfides/Selenides Really New and Promising Thermoelectric Materials?* Advanced Energy Materials, 2014. **4**(9).

39. Allgaier, R.S., *History of Narrow-Gap Semiconductors and Semimetals, 1945-65.* Semiconductor Science and Technology, 1990. **5**: p. S326-S333.

40. Wang, H., E. Schechtel, Y. Pei, and G.J. Snyder, *High Thermoelectric Efficiency of n-type PbS.* Advanced Energy Materials, 2013. **3**(4): p. 488-495.

41. Zhao, L.D., S.H. Lo, J. He, H. Li, K. Biswas, J. Androulakis, C.I. Wu, T.P. Hogan, D.Y. Chung, V.P. Dravid, and M.G. Kanatzidis, *High Performance Thermoelectrics from Earth-Abundant Materials: Enhanced Figure of Merit in PbS by Second Phase Nanostructures.* J Am Chem Soc, 2011. **133**(50): p. 20476-87.

42. Chen, B.X., C. Uher, L. Iordanidis, and M.G. Kanatzidis, *Transport Properties of Bi_2S_3 and the Ternary Bismuth Sulfides $KBi_{6.33}S_{10}$ and $K_2Bi_8S_{13}$.* Chemistry of Materials, 1997. **9**(7): p. 1655-1658.

43. Yu, Y.Q., B.P. Zhang, Z.H. Ge, P.P. Shang, and Y.X. Chen, *Thermoelectric Properties of Ag-doped Bismuth Sulfide Polycrystals Prepared by Mechanical Alloying and Spark Plasma Sintering.* Materials Chemistry and Physics, 2011. **131**(1-2): p. 216-222.

44. Chmielowski, R., D. Pere, C. Bera, I. Opahle, W.J. Xie, S. Jacob, F. Capet, P. Roussel, A. Weidenkaff, G.K.H. Madsen, and G. Dennler, *Theoretical and Experimental Investigations of the Thermoelectric Properties of Bi_2S_3.* Journal of Applied Physics, 2015. **117**(12).

45. Liu, Z.H., Y.L. Pei, H.Y. Geng, J.C. Zhou, X.F. Meng, W. Cai, W.S. Liu, and J.H. Sui,

Enhanced Thermoelectric Performance of Bi_2S_3 by Synergistical Action of Bromine Substitution and Copper Nanoparticles. Nano Energy, 2015. **13**: p. 554-562.

46. Nassary, M.M., *Temperature Dependence of the Electrical Conductivity, Hall Effect and Thermoelectric Power of SnS Single Crystals.* Journal of Alloys and Compounds, 2005. **398**(1-2): p. 21-25.

47. Tan, Q., L.-D. Zhao, J.-F. Li, C.-F. Wu, T.-R. Wei, Z.-B. Xing, and M.G. Kanatzidis, *Thermoelectrics with Earth Abundant Elements: Low Thermal Conductivity and High Thermopower in Doped SnS.* J. Mater. Chem. A, 2014. **2**(41): p. 17302-17306.

48. Tan, Q. and J.F. Li, *Thermoelectric Properties of Sn-S Bulk Materials Prepared by Mechanical Alloying and Spark Plasma Sintering.* Journal of Electronic Materials, 2014. **43**(6): p. 2435-2439.

49. Guilmeau, E., A. Maignan, C. Wan, and K. Koumoto, *On the Effects of Substitution, Intercalation, Non-stoichiometry and Block Layer Concept in TiS_2 Based Thermoelectrics.* Physical Chemistry Chemical Physics, 2015. **17**(38): p. 24541-24555.

50. Jood, P. and M. Ohta, *Hierarchical Architecturing for Layered Thermoelectric Sulfides and Chalcogenides.* Materials, 2015. **8**(3): p. 1124-1149.

51. Beaumale, M., T. Barbier, Y. Bréard, G. Guelou, A.V. Powell, P. Vaqueiro, and E. Guilmeau, *Electron Doping and Phonon Scattering in $Ti_{1+x}S_2$ Thermoelectric Compounds.* Acta Materialia, 2014. **78**: p. 86-92.

52. Guilmeau, E., Y. Bréard, and A. Maignan, *Transport and Thermoelectric Properties in Copper Intercalated TiS_2 Chalcogenide.* Applied Physics Letters, 2011. **99**(5): p.

052107.

53. Wuensch, B.J., *Confirmation of the Crystal Structure of Tetrahedrite, $Cu_{12}Sb_4S_{13}$.* Science (New York, N.Y.), 1963. **141**(3583): p. 804-5.

54. Lu, X., D.T. Morelli, Y. Xia, and V. Ozolins, *Increasing the Thermoelectric Figure of Merit of Tetrahedrites by Co-Doping with Nickel and Zinc.* Chemistry of Materials, 2015. **27**(2): p. 408-413.

55. Lai, W., Y. Wang, D.T. Morelli, and X. Lu, *From Bonding Asymmetry to Anharmonic Rattling in $Cu_{12}Sb_4S_{13}$ Tetrahedrites: When Lone-Pair Electrons Are Not So Lonely.* Advanced Functional Materials, 2015. **25**(24): p. 3648-3657.

56. Suekuni, K., K. Tsuruta, T. Ariga, and M. Koyano, *Thermoelectric Properties of Mineral Tetrahedrites $Cu_{10}Tr_2Sb_4S_{13}$ with Low Thermal Conductivity.* Applied Physics Express, 2012. **5**(5): p. 051201.

57. Lu, X. and D.T. Morelli, *Natural Mineral Tetrahedrite as a Direct Source of Thermoelectric Materials.* Physical Chemistry Chemical Physics, 2013. **15**(16): p. 5762-6.

58. Suekuni, K., K. Tsuruta, M. Kunii, H. Nishiate, E. Nishibori, S. Maki, M. Ohta, A. Yamamoto, and M. Koyano, *High-Performance Thermoelectric Mineral $Cu_{12-x}Ni_xSb_4S_{13}$ Tetrahedrite.* Journal of Applied Physics, 2013. **113**(4): p. 043712.

59. Barbier, T., P. Lemoine, S. Gascoin, O.I. Lebedev, A. Kaltzoglou, P. Vaqueiro, A.V. Powell, R.I. Smith, and E. Guilmeau, *Structural Stability of the Synthetic Thermoelectric Ternary and Nickel-Substituted Tetrahedrite Phases.* Journal of Alloys and Compounds,

2015. **634**: p. 253-262.

60. Bouyrie, Y., C. Candolfi, A. Dauscher, B. Malaman, and B. Lenoir, *Exsolution Process as a Route toward Extremely Low Thermal Conductivity in $Cu_{12}Sb_{4-x}Te_xS_{13}$ Tetrahedrites.* Chemistry of Materials, 2015. **27**(24): p. 8354-8361.

61. Chetty, R., A. Bali, M.H. Naik, G. Rogl, P. Rogl, M. Jain, S. Suwas, and R.C. Mallik, *Thermoelectric Properties of Co Substituted Synthetic Tetrahedrite.* Acta Materialia, 2015. **100**: p. 266-274.

62. Chetty, R., S.P. D, G. Rogl, P. Rogl, E. Bauer, H. Michor, S. Suwas, S. Puchegger, G. Giester, and R.C. Mallik, *Thermoelectric Properties of a Mn Substituted Synthetic Tetrahedrite.* Phys Chem Chem Phys, 2015. **17**(3): p. 1716-27.

63. Lu, X. and D. Morelli, *The Effect of Te Substitution for Sb on Thermoelectric Properties of Tetrahedrite.* Journal of Electronic Materials, 2013. **43**(6): p. 1983-1987.

64. Chetty, R., A. Bali, and R.C. Mallik, *Tetrahedrites as Thermoelectric Materials: an Overview.* Journal of Materials Chemistry C, 2015. **3**(48): p. 12364-12378.

65. Lu, X. and D.T. Morelli, *Rapid Synthesis of High-performance Thermoelectric Materials Directly from Natural Mineral Tetrahedrite.* MRS Communications, 2013. **3**(03): p. 129-133.

66. Skinner, B.J., F.D. Luce, and E. Makovicky, *Studies of the Sulfosalts of Copper III; Phases and Phase Relations in the System Cu-Sb-S.* Economic Geology, 1972. **67**(7): p. 924-938.

67. Dufton, J.T., A. Walsh, P.M. Panchmatia, L.M. Peter, D. Colombara, and M.S. Islam,

Structural and Electronic Properties of $CuSbS_2$ and $CuBiS_2$: Potential Absorber Materials for Thin-Film Solar Cells. Physical Chemistry Chemical Physics, 2012. **14**(20): p. 7229-33.

68. Kyono, A., *Crystal Structures of Chalcostibite ($CuSbS_2$) and Emplectite ($CuBiS_2$): Structural Relationship of Stereochemical Activity between Chalcostibite and Emplectite.* American Mineralogist, 2005. **90**(1): p. 162-165.

69. Smith, J.D., *The Chemistry of Arsenic, Antimony and Bismuth: Pergamon Texts in Inorganic Chemistry*. Vol. 2. 2013: Elsevier.

70. Baker, J., R.S. Kumar, D. Sneed, A. Connolly, Y. Zhang, N. Velisavljevic, J. Paladugu, M. Pravica, C. Chen, A. Cornelius, and Y. Zhao, *Pressure Induced Structural Transitions in $CuSbS_2$ and $CuSbSe_2$ Thermoelectric Compounds.* Journal of Alloys and Compounds, 2015. **643**: p. 186-194.

71. Kumar, M. and C. Persson, *$Cu(Sb,Bi)(S,Se)_2$ as Indium-free Absorber Material with High Optical Efficiency.* Energy Procedia, 2014. **44**: p. 176-183.

72. Ramasamy, K., H. Sims, W.H. Butler, and A. Gupta, *Selective Nanocrystal Synthesis and Calculated Electronic Structure of All Four Phases of Copper–Antimony–Sulfide.* Chemistry of Materials, 2014. **26**(9): p. 2891-2899.

73. Kittel, C., *Introduction to Solid State Physics*. 2005: Wiley.

74. Welch, A.W., L.L. Baranowski, P. Zawadzki, C. DeHart, S. Johnston, S. Lany, C.A. Wolden, and A. Zakutayev, *Accelerated Development of $CuSbS_2$ Thin Film Photovoltaic Device Prototypes.* Progress in Photovoltaics: Research and Applications, 2016: p. 929-

939.

75. Wachtel, A. and A. Noreika, *Growth and Characterization of $CuSbS_2$ Crystals.* Journal of Electronic Materials. **9**(2): p. 281-297.

76. Kumar Gudelli, V., V. Kanchana, G. Vaitheeswaran, A. Svane, and N.E. Christensen, *Thermoelectric Properties of Chalcopyrite Type $CuGaTe_2$ and Chalcostibite $CuSbS_2$.* Journal of Applied Physics, 2013. **114**(22): p. 223707.

77. Kehoe, A.B., D.J. Temple, G.W. Watson, and D.O. Scanlon, *Cu_3MCh_3 (M = Sb, Bi; Ch = S, Se) as Candidate Solar Cell Absorbers: Insights from Theory.* Phys Chem Chem Phys, 2013. **15**(37): p. 15477-84.

78. Qiu, X., S. Ji, C. Chen, G. Liu, and C. Ye, *Synthesis, Characterization, and Surface-Enhanced Raman Scattering of Near Infrared Absorbing Cu_3SbS_3 Nanocrystals.* CrystEngComm, 2013. **15**(48): p. 10431.

79. Tablero, C., *Electronic Property Analysis of O-doped Cu_3SbS_3.* Solar Energy Materials and Solar Cells, 2012. **104**: p. 180-184.

80. Skoug, E.J., J.D. Cain, and D.T. Morelli, *Structural Effects on the Lattice Thermal Conductivity of Ternary Antimony- and Bismuth-Containing Chalcogenide Semiconductors.* Applied Physics Letters, 2010. **96**(18): p. 181905.

81. Sevik, C. and T. Çağın, *Investigation of Thermoelectric Properties of Chalcogenide Semiconductors from First Principles.* Journal of Applied Physics, 2011. **109**(12): p. 123712.

82. Tyagi, K., B. Gahtori, S. Bathula, V. Toutam, S. Sharma, N.K. Singh, and A. Dhar,

Thermoelectric and Mechanical Properties of Spark Plasma Sintered Cu_3SbSe_3 and Cu_3SbSe_4: Promising Thermoelectric Materials. Applied Physics Letters, 2014. **105**(26): p. 261902.

83. Tyagi, K., B. Gahtori, S. Bathula, A.K. Srivastava, A.K. Shukla, S. Auluck, and A. Dhar, *Thermoelectric Properties of Cu_3SbSe_3 with Intrinsically Ultralow Lattice Thermal Conductivity.* Journal of Materials Chemistry A, 2014. **2**(38): p. 15829-15835.

84. Wei, T.-R., C.-F. Wu, W. Sun, Y. Pan, and J.-F. Li, *Is Cu_3SbSe_3 a Promising Thermoelectric Material?* RSC Adv., 2015. **5**(53): p. 42848-42854.

85. Zhang, Y., E. Skoug, J. Cain, V. Ozoliņš, D. Morelli, and C. Wolverton, *First-Principles Description of Anomalously Low Lattice Thermal Conductivity in Thermoelectric Cu-Sb-Se Ternary Semiconductors.* Physical Review B, 2012. **85**(5).

86. Kirkham, M., P. Majsztrik, E. Skoug, D. Morelli, H. Wang, W.D. Porter, E.A. Payzant, and E. Lara-Curzio, *High-Temperature Order/Disorder Transition in the Thermoelectric Cu_3SbSe_3.* Journal of Materials Research, 2011. **26**(15): p. 2001-2005.

87. Whitfield, H.J., *Polymorphism in Skinnerite, Cu_3SbS_3.* Solid State Communications, 1980. **33**(7): p. 747-748.

88. Pfitzner, A., *Disorder of Cu in Cu_3SbS_3: Structural Investigations of the High- and Low-Temperature Modification Abstract.* Zeitschrift für Kristallographie. Crystalline materials. **213**(4): p. 228-236.

89. Pfitzner, A., *Cu_3SbS_3: Zur Kristallstruktur und Polymorphie.* Zeitschrift für anorganische und allgemeine Chemie (1950). **620**(11): p. 1992-1997.

90. Pfitzner, A.R., S., *Refinement of the Crystal Structures of Cu_3PS_4 and Cu_3SbS_4 and a Comment on Normal Tetrahedral Structures.* Zeitschrift für Kristallographie, 2002. **217**(2-2002): p. 4.

91. Zhang, J.W., R.H. Liu, N.A. Cheng, Y.B. Zhang, J.H. Yang, C. Uher, X. Shi, L.D. Chen, and W.Q. Zhang, *High-Performance Pseudocubic Thermoelectric Materials from Non-cubic Chalcopyrite Compounds.* Advanced Materials, 2014. **26**(23): p. 3848-3853.

92. Liu, W., X. Tan, K. Yin, H. Liu, X. Tang, J. Shi, Q. Zhang, and C. Uher, *Convergence of Conduction Bands as a Means of Enhancing Thermoelectric Performance of n-type $Mg_2Si_{1-x}Sn_x$ solid solutions.* Phys Rev Lett, 2012. **108**(16): p. 166601.

93. Do, D.T. and S.D. Mahanti, *Bonds, Bands, and Band Gaps in Tetrahedrally Bonded Ternary Compounds: The Role of Group V Lone Pairs.* Journal of Physics and Chemistry of Solids, 2014. **75**(4): p. 477-485.

94. Yang, C., F. Huang, L. Wu, and K. Xu, *New Stannite-like p-type Thermoelectric Material Cu_3SbSe_4.* Journal of Physics D: Applied Physics, 2011. **44**(29): p. 295404.

95. Skoug, E.J., J.D. Cain, and D.T. Morelli, *High Thermoelectric Figure of Merit in the Cu_3SbSe_4-Cu_3SbS_4 Solid Solution.* Applied Physics Letters, 2011. **98**(26): p. 261911.

96. Li, X.Y., D. Li, H.X. Xin, J. Zhang, C.J. Song, and X.Y. Qin, *Effects of Bismuth Doping on the Thermoelectric Properties of Cu_3SbSe_4 at Moderate Temperatures.* Journal of Alloys and Compounds, 2013. **561**: p. 105-108.

97. Li, D., R. Li, X.Y. Qin, C.J. Song, H.X. Xin, L. Wang, J. Zhang, G.L. Guo, T.H. Zou, Y.F. Liu, and X.G. Zhu, *Co-precipitation Synthesis of Nanostructured Cu_3SbSe_4 and its*

Sn-doped Sample with High Thermoelectric Performance. Dalton Trans, 2014. **43**(4): p. 1888-96.

98. Wei, T.-R., F. Li, and J.-F. Li, *Enhanced Thermoelectric Performance of Nonstoichiometric Compounds $Cu_{3-x}SbSe_4$ by Cu Deficiencies.* Journal of Electronic Materials, 2014. **43**(6): p. 2229-2238.

99. Wei, T.R., H. Wang, Z.M. Gibbs, C.F. Wu, G.J. Snyder, and J.F. Li, *Thermoelectric Properties of Sn-doped p-type Cu_3SbSe_4: a Compound with Large Effective Mass and Small Band Gap.* Journal of Materials Chemistry A, 2014. **2**(33): p. 13527-13533.

100. Li, Y., X. Qin, D. Li, X. Li, Y. Liu, J. Zhang, C. Song, and H. Xin, *Transport Properties and Enhanced Thermoelectric Performance of Aluminum Doped Cu_3SbSe_4.* RSC Adv., 2015. **5**(40): p. 31399-31403.

101. Kumar, A., P. Dhama, D.S. Saini, and P. Banerji, *Effect of Zn Substitution at a Cu Site on the Transport Behavior and Thermoelectric Properties in Cu_3SbSe_4.* RSC Adv., 2016. **6**(7): p. 5528-5534.

102. Katsumi, H., K. Masaru, and I. Taizo, *On the Electrical and Thermal Properties of the Ternary Chalcogenides $A_2^IB^{IV}X_3$, $A^IB^VX_2$ and $A_3^IB^VX_4$ (AI=Cu; BIV=Ge, Sn; BV=Sb; X=S, Se, Te). I. Thermoelectric Properties at Room Temperature.* Jpn. J. Appl. Phys. , 1968. **7** p. 6.

103. Suzumura, A., M. Watanabe, N. Nagasako, and R. Asahi, *Improvement in Thermoelectric Properties of Se-Free Cu_3SbS_4 Compound.* Journal of Electronic Materials, 2014. **43**(6): p. 2356-2361.

104. Guillon, O., J. Gonzalez-Julian, B. Dargatz, T. Kessel, G. Schierning, J. Räthel, and M. Herrmann, *Field-Assisted Sintering Technology/Spark Plasma Sintering: Mechanisms, Materials, and Technology Developments.* Advanced Engineering Materials, 2014. **16**(7): p. 830-849.

105. Berger, L.I., *Semiconductor Materials*. 1996: CRC Press.

106. Suryanarayana, C., E. Ivanov, and V.V. Boldyrev, *The Science and Technology of Mechanical Alloying.* Materials Science and Engineering: A, 2001. **304–306**: p. 151-158.

107. Heo, J., R. Ravichandran, C.F. Reidy, J. Tate, J.F. Wager, and D.A. Keszler, *Design Meets Nature: Tetrahedrite Solar Absorbers.* Advanced Energy Materials, 2015. **5**(7): p. 1401506.

108. Yan, C., Z. Su, E. Gu, T. Cao, J. Yang, J. Liu, F. Liu, Y. Lai, J. Li, and Y. Liu, *Solution-Based Synthesis of Chalcostibite ($CuSbS_2$) Nanobricks for Solar Energy Conversion.* RSC Advances, 2012. **2**(28): p. 10481.

109. *Mott,N.F, E.A. Davis. Electronic Processes in Non-Crystalline Materials. 2012: Oxford University Press.*

110. Yosuke Goto, Y.S., Yoichi Kamihara, Masanori Matoba, *Effect of Sn-substitution On Thermoelectric Properties of Copper-based Sulfide, Famatinite Cu_3SbS_4.* Journal of the Physical Society of Japan, 2015. **84**(4).

111. Nielsen, M.D., V. Ozolins, and J.P. Heremans, *Lone Pair Electrons Minimize Lattice Thermal Conductivity.* Energy Environ. Sci., 2013. **6**(2): p. 570-578.

112. Pfitzner, A., M. Evain, and V. Petricek, *$Cu_{12}Sb_4S_{13}$: A Temperature-dependent*

Structure Investigation. Acta Crystallographica Section B-Structural Science, 1997. **53**: p. 337-345.

113. Zhou, J., G.-Q. Bian, Q.-Y. Zhu, Y. Zhang, C.-Y. Li, and J. Dai, *Solvothermal Crystal Growth of $CuSbQ_2$ (Q=S, Se) and the Correlation between Macroscopic Morphology and Microscopic Structure.* Journal of Solid State Chemistry, 2009. **182**(2): p. 259-264.

114. Makovicky, E. and T. Balic-Zunic, *The Crystal Structure of Skinnerite, P21/c-Cu_3SbS_3, from Powder Data.* The Canadian Mineralogist, 1995. **33**: p. 9.

115. Nolas, G.S., Sharp, J., Goldsmid, J., *Thermoelectrics Basic Principles and New Materials Developments*. 2001: Springer-Verlag Berlin Heidelberg.

116. Amirkhanov, K.I., G.G. Gadzhiev, and Y.B. Magomedov, *Cu_3SbS_4 Band Gap.* Teplofiz. Vys.Temp., 1978. **16**.

117. Sommerfeld, A., *Zur Elektronentheorie der Metalle.* Naturwissenschaften, 1927. **15**(41): p. 825-832.

118. Lukas, K.C., W.S. Liu, G. Joshi, M. Zebarjadi, M.S. Dresselhaus, Z.F. Ren, G. Chen, and C.P. Opeil, *Experimental Determination of the Lorenz Number in $Cu_{0.01}Bi_2Te_{2.7}Se_{0.3}$ and $Bi_{0.88}Sb_{0.12}$.* Physical Review B, 2012. **85**(20).

119. Yosuke, G., S. Yuki, K. Yoichi, and M. Masanori, *Electronic Structure and Transport Properties of Cu-deficient Kuramite $Cu_{3-x}SnS_4$.* Japanese Journal of Applied Physics, 2015. **54**(2): p. 021801.

120. Van Embden, J. and Y. Tachibana, *Synthesis and Characterisation of Famatinite*

Copper Antimony Sulfide Nanocrystals. Journal of Materials Chemistry, 2012. **22**(23): p. 11466.

121. Yang, B., L. Wang, J. Han, Y. Zhou, H. Song, S. Chen, J. Zhong, L. Lv, D. Niu, and J. Tang, *$CuSbS_2$ as a Promising Earth-Abundant Photovoltaic Absorber Material: A Combined Theoretical and Experimental Study.* Chemistry of Materials, 2014. **26**(10): p. 3135-3143.

122. Hu, H., Z. Liu, B. Yang, X. Chen, and Y. Qian, *Template-mediated Growth of Cu_3SnS_4 Nanoshell Tubes.* Journal of Crystal Growth, 2005. **284**(1–2): p. 226-234.

123. Chusuei, C.C. and D.W. Goodman, *X-Ray Photoelectron Spectroscopy A2 - Meyers, Robert A*, in *Encyclopedia of Physical Science and Technology (Third Edition)*. 2003, Academic Press: New York. p. 921-938.

124. *NIST X-ray Photoelectron Spectroscopy Database* 2012.

125. Sarswat, P.K. and M.L. Free, *Enhanced Photoelectrochemical Response from Copper Antimony Zinc Sulfide Thin Films on Transparent Conducting Electrode.* International Journal of Photoenergy, 2013. **2013**: p. 1-7.

126. Lin, X., A. Steigert, M.C. Lux-Steiner, and A. Ennaoui, *One-step Solution-based Synthesis and Characterization of Kuramite Cu_3SnS_4 nanocrystals.* RSC Advances, 2012. **2**(26): p. 9798-9800.

127. Skoug, E.J., J.D. Cain, D.T. Morelli, M. Kirkham, P. Majsztrik, and E. Lara-Curzio, *Lattice Thermal Conductivity of the Cu_3SbSe_4-Cu_3SbS_4 Solid Solution.* Journal of Applied Physics, 2011. **110**(2): p. 023501.

128. Denton, A.R. and N.W. Ashcroft, *Vegard's law.* Physical Review A, 1991. **43**(6): p. 3161-3164.

129. Goto, Y., Y. Sakai, Y. Kamihara, and M. Matoba, *Effect of Sn-Substitution on Thermoelectric Properties of Copper-Based Sulfide, Famatinite Cu_3SbS_4.* Journal of the Physical Society of Japan, 2015. **84**(4): p. 044706.

130. Pfitzner, A. and T. Bernert, *The System Cu_3AsS_4–Cu_3SbS_4 and Investigations on Normal Tetrahedral Structures, Zeitschrift für Kristallographie - Crystalline Materials*. 2004. **219**(1): p. 20-26.

Appendix

Density and calculated heat capacity of all samples for thermal conductivity calculation.

Sample Name	**Density (gcm^{-3})**	**Heat Capacity ($Jg^{-1}K^{-1}$)**
Cu_3SbS_4 (Melt+SPS)	4.55	0.46
Cu_3SbS_4 (MA+SPS)	4.60	0.46
$Cu_{12}Sb_4S_{13}$	4.99	0.44
Cu_3SbS_3	5.01	0.43
$CuSbS_2$	4.93	0.40
$Cu_3Sb_{1-x}Ge_xS_4$ (x=0.0125)	4.59	0.46
$Cu_3Sb_{1-x}Ge_xS_4$ (x=0.025)	4.60	0.46
$Cu_3Sb_{1-x}Ge_xS_4$ (x=0.05)	4.59	0.46
$Cu_3Sb_{1-x}Ge_xS_4$ (x=0.075)	4.57	0.46
$Cu_3Sb_{1-x}Ge_xS_4$ (x=0.1)	4.58	0.46
$Cu_3Sb_{1-x}Ge_xS_4$ (x=0.15)	4.60	0.46
$Cu_3Sb_{1-x}Sn_xS_4$ (x=0.1)	4.62	0.46
$Cu_3Sb_{1-x}Sn_xS_4$ (x=0.2)	4.64	0.46
$Cu_3Sb_{1-x}Sn_xS_4$ (x=0.3)	4.65	0.46
$Cu_3Sb_{1-x}Sn_xS_4$ (x=0.4)	4.65	0.46
$Cu_3Sb_{1-x}Sn_xS_4$ (x=0.5)	4.67	0.46
$Cu_3Sb_{1-x}Sn_xS_4$ (x=0.01)	4.60	0.46
$Cu_3Sb_{1-x}Sn_xS_4$ (x=0.03)	4.61	0.46
$Cu_3Sb_{1-x}Sn_xS_4$ (x=0.05)	4.57	0.46
$Cu_3Sb_{1-x}Sn_xS_4$ (x=0.15)	4.60	0.46
$Cu_3SbS_{4(1-y)}Se_{4y}$ (y=0.05)	4.68	0.45
$Cu_3SbS_{4(1-y)}Se_{4y}$ (y=0.1)	4.72	0.44
$Cu_3SbS_{4(1-y)}Se_{4y}$ (y=0.2)	4.83	0.42
$Cu_3SbS_{4(1-y)}Se_{4y}$ (y=0.3)	4.90	0.40
$Cu_3SbS_{4(1-y)}Se_{4y}$ (y=0.4)	5.02	0.39
$Cu_3SbS_{4(1-y)}Se_{4y}$ (y=0.5)	5.14	0.38
$Cu_3Sb_{1-x}Sn_xS_{4(1-y)}Se_{4y}$ (x=0.1, y=0.1)	4.75	0.44